

SILICON-BASED PHOTONIC, PLASMONIC, AND
OPTOMECHANIC DEVICES

A DISSERTATION
SUBMITTED TO THE DEPARTMENT OF ELECTRICAL
ENGINEERING
AND THE COMMITTEE ON GRADUATE STUDIES
OF STANFORD UNIVERSITY
IN PARTIAL FULFILLMENT OF THE REQUIREMENTS
FOR THE DEGREE OF
DOCTOR OF PHILOSOPHY

Yiyang Gong

December 2010

Abstract

The integration of optical devices and electronic devices on the same platform is currently a gateway into many research and practical applications. Because silicon and silicon compatible materials have dominated electronic development, optical devices must also conform to the silicon platform. One of the greatest challenges in building such an integrated opto-electronic system is the development of an efficient Si-compatible light emitter.

In this thesis, we develop several Si-based nano-photonic devices for the control of light at the nano-scales. However, several Si-compatible materials and light emitters have low index of refraction (n), and high degrees of confinement using only index contrast and total internal reflection is difficult. We design high quality (Q -) factor photonic crystal nanobeam cavities for a variety of materials with low index, such as SiO_2 ($n = 1.46$), silicon rich oxide ($n = 1.7$), and silicon nitride ($n = 2.0$), all with $Q > 5,000$ and mode volumes $V_m < 2.0(\lambda/n)^3$. We employ these cavity designs to a variety of active materials, including Si-nanocrystal doped silicon oxide, Er-doped amorphous silicon nitride (Er:SiN_x), and InAs quantum quantum dots (QDs) in GaAs. By placing emitters in these ultrasmall, high- Q cavities, we demonstrate that the cavity enhances emission processes. We show that the free carrier absorption processes are greatly enhanced in the Si-nanocrystal nanobeam cavities at both room and cryogenic temperatures, up to an order of magnitude compared to bulk. In addition, we demonstrate that nanobeam cavities made of Er:SiN_x have enhanced absorption and gain characteristics compared to earlier designs that included silicon in the cavity. Because of the reduced losses stemming from absorption, we observe

linewidth narrowing and material transparency at both room temperature and cryogenic temperatures. Finally, we demonstrate low threshold continuous-wave lasing from InAs QDs embedded in 1D nanobeam PC cavities, with pump power thresholds below $1 \mu\text{W}$. We investigate the behavior of the threshold for different pump conditions and manipulate the cavity with a fiber taper in close proximity to the cavity.

We also design plasmonic cavity and grating structures, which have lower Q compared to photonic crystal cavities due to metal ohmic losses, but have low mode volumes that break the diffraction limit. We propose and study a planar distributed Bragg reflector plasmonic cavity analogous to the nanobeam photonic cavity. We show that a plasmonic bandgap arising from a metallic grating can confine a plasmonic mode to a defect region, and enables ultrasmall volume that can enhance luminescence from emitters embedded in the cavity. We also demonstrate the enhancement of emission from silicon nanocrystals coupled to wide area plasmonic grating modes and Er:SiN_x coupled to metal-insulator-metal modes confined between two metal layers. We demonstrate the control of emission wavelength by changing the device dimensions in both cases, and in the case of the Er material, observe an order of magnitude increase in collected emission compared to a sample with only one side contacting the metal. In addition, we identify both local and coupled plasmonic modes supported by metallic gratings and nano-particle arrays.

Finally, we demonstrate resonant actuation of a mechanical mode with optical gradient forces in a Si nanobeam cavity. The optical cavity enhances the optomechanical coupling between the optical mode and the mechanical vibration, and enables detectable mechanical motions with hundreds of nanowatts driving an optical cavity mode.

Acknowledgements

Working toward a Ph. D. for over five years is a great challenge, and certainly not a solo effort. I have met a variety of people in academic and non-academic settings that have contributed to this thesis and the overall graduate student experience. I value all of the help that I've received, and I would like to acknowledge the various sources of support below.

First, I thank Prof. Jelena Vučković for all of her patience and guidance. She has given me an unparalleled amount academic freedom and allowed me to pursue a variety of ideas. Her help through the ups and downs of my graduate student career has been invaluable, and I appreciate everything that she has done. It does not surprise me that I continue to learn from her as time goes on, and I hope to count on her as a mentor in the future.

I also thank the members of my reading and oral committee Prof. David Miller, Prof. Shanhui Fan and Prof. Mark Brongersma, for their comments and thoughts on this thesis. They have all demonstrated an outstanding passion for their work, which translates into great understanding of their respective fields that easily comes across during my conversations with them.

I thank the various members of the Vučković group that I had the pleasure to interact with over the years. The graduated members: Hatice Altug, Dirk Englund, Andrei Faraon, Ilya Fushman, Maria Makarova, Vanessa Sih, and Edo Waks have set the bar very high for the future graduates of the group. The visiting scholars: Hideo Iwase, Takuya Konno, and Mitsuru Toishi, have provided fresh perspectives on many subjects. The present members: Michal Bajcsy, Sonia Buckley, Bryan Ellis, Erik Kim, Carter Lin, Jesse Lu, Arka Majumdar, Alexander Papageorge, Jan Petykiewitz,

Kelley Rivoire, Armand Rundquist, and Gary Shambat all have bright futures ahead, and I am eager to see their work in the future. I especially thank Maria (with whom I worked closely on the Er project), Jesse, Bryan, Gary, Armand, and Arka, with whom I have worked on various projects.

I thank our various collaborators on the different projects. The growers of the silicon nanocrystal material, Szu-Lin Cheng and Satoshi Ishikawa of the Yoshio Nishi group, provided material with very little turnaround. It was a pleasure to collaborate with them and discuss the future applications of silicon photonics. Selçuk Yerci, and Rui Li in Prof. Luca Dal Negro's group has provided an immense amount of support for the Er-doped nitride material, and their material expertise was instrumental in characterizing the observed linewidth-narrowing effect. Similarly, our collaborators at NIST, Sae Woo Nam, Martin Stevens, and Burn Baek deserve our gratitude, as their experimental expertise on time-resolved measurements for low-power sources allowed the characterization of Purcell enhancement. Finally, I thank Tomas Sarmiento of the Jim Harris group for growing the quantum dots used in the laser work. His help on the materials side of things was greatly appreciated.

I thank the various SNF staff who I have received training from: James Conway, Nancy Latta, Jim McVitte, Ed Myers, Jeannie Perez, Paul Rissman, Mary tang, and Uli Thumser. I also thank the staff for maintaining equipment, especially James Conway (e-beam), Elmer Enriquez and Cesar Baxter (etchers), Jim Haydon (metal evaporator), and Mahnaz Mansourpour, Gary Sosa, and Mario Vilanova (lithography). I greatly appreciate the vast effort that keeps the SNF equipment functional, and how it has enabled the research of this thesis.

I thank the various people that I have had the time to talk about science and non-science while at Stanford: Krishna Balram, Linyou Cao, Kristiaan DeGreve, Dany Ly-Gagnon, J. R. Heberle, Peter McMahon, Min-Kyo Seo, and Justin White. It was always fun having conversations about our individual and collective futures, which as the occasion necessitated, served as inspirations or diversions.

Finally, I thank my parents. Their support has been unwavering over the years, and I cherish all of their kind thoughts. I dedicate this thesis to them.

Contents

Abstract	iv
Acknowledgements	vi
1 Introduction	2
1.1 Optical Sources for Photonic Networks	2
1.2 Photonic Crystal Cavities	5
1.3 Plasmonic structures	7
1.3.1 Silicon Nanocrystals	10
1.3.2 Erbium doped Silicon Nitride	11
1.3.3 InAs Quantum Dots	12
1.4 Thesis Outline	12
2 Design of Photonic Crystal Cavity and Plasmonic Cavity Structures	15
2.1 One dimensional Nanobeam Photonic Crystal Cavity	15
2.1.1 Nanobeam Cavity in Silicon Dioxide	16
2.1.2 Nanobeam Cavity in Silicon Rich Oxide	20
2.1.3 Nanobeam Cavity in Silicon Nitride	22
2.1.4 High-index Nanobeam Cavities	24
2.2 Plasmonic Cavity	26
2.2.1 Metallic Distributed Bragg Reflection Cavity	26
2.2.2 Metallic Grating Modes with Silicon Oxide	33
2.2.3 Metallic Grating Modes in Metal-Insulator-Metal Configuration with Silicon Nitride	35

3 Enhancement of Photoluminescence and Lasing in One-dimensional Photonic Crystal Cavities	39
3.1 Silicon Nanocrystals in Oxide	39
3.2 Erbium-doped Amorphous Silicon Nitride	53
3.3 InAs Quantum Dots in GaAs nanobeam laser	62
4 Plasmonic Enhancement of Emission from Si-compatible Materials	72
4.1 Plasmonic Enhancement of Silicon Nanocrystals	72
4.2 Enhancement of Er Photoluminescence via Metal-Insulator-Metal modes	77
5 Passive Nanobeam Cavities	85
5.1 Silicon dioxide nanobeam cavities	85
5.2 Silicon nanobeam cavities	87
6 Optomechanics in One-dimensional Photonic Crystal Cavities	89
7 Conclusion and Future Directions	99
A Fabrication	103
A.1 Silicon Dioxide beam cavities	103
A.2 Silicon dioxide beam cavities with embedded Si nanocrystals	104
A.3 Er-doped Silicon Nitride Beam Cavities	104
A.4 GaAs Beam Cavities	105
A.5 Si Beam Cavities	105
A.6 Metallic Gratings on Si-NC layer	105
A.7 Metallic Gratings in MIM Configuration	106
B Finite Difference Time Domain Simulations	107
C Optical Setup	113
D Theory of Resonant Excitation of a Mechanical Mode through an Optical Cavity Mode	115

D.1 Example 1: Cosine input	117
Bibliography	120

List of Tables

C.1 List of optical components.	114
---	-----

List of Figures

- | | |
|---|---|
| 1.1 (a) The 2D PC cavity system in a suspended membrane, with the cavity defect and the periodic air holes that form the triangular lattice photonic crystal. TIR confines the light in the out-of-plane directions of the membrane, while DBR confines the light in the directions in the plane of the membrane. The inset shows the irreducible Brillouin zone in the reciprocal space for the triangular lattice, along with the labeled high symmetry points. (b) A representative band diagram for the TE-like polarization along the high-symmetry directions, for a slab with index of refraction $n = 3.5$. The solid line is the light-line, which separates the states confined by the total internal reflection (below the line) from those that leak in the direction perpendicular to the membrane. The optical bandgap is seen below the light line and between normalized frequencies $a/\lambda = 0.25$ and 0.33 | 7 |
| 1.2 (a) Depiction of the SPP mode. (b) The dispersion relationship for the SPP modes on a gold-air interface. The light-line ($\omega = ck_{sp}$) and ω_{sp} (where ω_p is the bulk plasma frequency) asymptote are also shown. . | 9 |

2.1	(a) The fabricated 1D nanobeam cavity in silica (SiO_2 , $n = 1.46$) imaged in an SEM. (b) The electric field intensity ($ E ^2$) of the fundamental mode supported by the cavity. (c) Band diagram for a beam with lattice constant a , $w = 3a$, $d = 0.9a$, $h_x = 0.5a$, and $h_y = 0.7w$, and another beam with the same parameters except for lattice constant $a' = 0.9a$. The dashed line indicates the light line in free space. (d) Design of the cavity. The plot shows the period (a) along the length of the beam as a function of N , the layer number counted from the center of the cavity.	17
2.2	(a) The direction specific Q -factors of the silica nanobeam cavity as a function of the number of photonic crystal mirror layers surrounding the cavity. With respect to Fig. 2.1(b), Q_{\perp} corresponds to radiation leaked in the z direction, Q_{\parallel} corresponds to radiation leaked in the y direction, and Q_{PC} corresponds to radiation leaked in the x direction. Q_{tot} is the parallel sum of Q_{\perp} , Q_{\parallel} , and Q_{PC} . (b) The Q -factors and (c) the mode volumes of cavities with the same air hole design, but different beam widths and thicknesses. The reference dot sizes are for $Q = 2.0 \times 10^4$ and $V_m = 2.0(\lambda/n)^3$ in (b) and (c), respectively.	19
2.3	(a) SEM image of the fabricated beam structure. The E_y component of the (b) first- (c) second- and (d) third-order TE-like modes supported by the nanobeam with parameters $w = 3.2a$, $h_x = 0.5a$, $h_y = 0.7w$, and thickness $d = 0.7a$ are also shown. The beam material has index $n = 1.7$	21
2.4	(a) Q and (b) V_m for the TE_0 mode for different beam widths (w) and thicknesses (d) for nanobeam cavities in $n = 1.7$ material. We keep the same air hole design for the simulated cavities.	22

2.5	(a) SEM image of the fabricated Er:SiN _x nanobeam cavity. (b) The E ² profile of the fundamental cavity mode from FDTD simulations. (c)-(d) The color of each marker illustrates the Q and V _m of nanobeam cavities in n = 2.1 material as the width and height of the beam is changed, while h _x = 0.5a, h _y = 0.7w, and the design of the holes are fixed. The reference markers represent Q = 30,000 and V _m = 0.95(λ/n) ³ .	23
2.6	(a) The fabricated 1D nanobeam cavity in GaAs, with index n = 3.5. (b) The electric field intensity (E ²) of the fundamental mode supported by the cavity.	25
2.7	(a) The E _y profile for the (a) first and (b) second order modes using the taperout design.	25
2.8	(a) The proposed structure. (b)-(d) Mode profiles (E ²) with total cavity lengths 216 nm, 328 nm, and 440 nm, respectively. These correspond to 2, 3, and 4 peaks of the electric field intensity inside the cavity.	27
2.9	Dependence of (a) frequency and (b) quality factor (Q) of the localized plasmon mode on the cavity length. In (a), the dots sizes are proportional to the mode Q-factor.	29
2.10	(a) Dependence of Purcell enhancement (normalized by width of the cavity in the y direction of Fig. 2.8) on cavity length for various emitter positions relative to the metal-dielectric interface (z direction). (b) Exponential decay of the electric field in the dielectric (E ²) away from the metal-dielectric interface, plotted for 3 different cavity lengths corresponding to maximum Purcell enhancements. The decay constant of 36 nm is consistent with the plasmon modes in the band gap at the k _{sp} = π/a point. (c) Normalized Purcell enhancement as a function of emitter position (in the x-direction) inside the 440 nm cavity for four different emitter distances from the metal-dielectric interface.	30

2.11 (a) Dependence of Purcell enhancement on the loss factor, ξ , in the Drude model (ξ is inversely proportional to the damping frequency). The Purcell enhancements are calculated for emitters 20 nm from the metal-dielectric interface for three different cavity lengths. (b) Dependence of the Purcell enhancement on the temperature, which is obtained by translating the ξ factor into temperatures for a residual resistivity of 1600 for silver.	32
2.12 (a) The FDTD calculated band edge frequencies for first, second, and third order modes of the SPP band diagram. The first and third order modes correspond to modes at the X ($k = \pi/a$) point of the dispersion relation, while the second order mode corresponds to modes at the Γ ($k = 0$) point. The $ E ^2$ and $ B ^2$ fields for the first (b), second (c), and third (d) order modes are plotted.	34
2.13 (a) The wavelengths of the first and second order field-symmetric MIM SPP modes for different grating periods, with a 52 nm thick layer of SiN_x between the metal layers. The analytical solution for a MIM structure with semi-infinite metal thickness and the same SiN_x thickness is also shown. (b) The magnetic field (B) and (c) the electric field intensity ($ E ^2$) of the first (top) and second (bottom) order modes near free space $\lambda_0 \approx 1500$ nm. The MIM SPP modes in a 2D simulation have B fields perpendicular to plane of the figures, while the E field is restricted to the plane of the figures. The inset of (b) shows the magnetic field through a vertical slice of the structure, as well as the analytical solution of a MIM system with semi-infinite metal thicknesses and a 52 nm SiN_x spacer layer.	37

3.1	(a) PL spectra from unpatterned oxide film with Si-NCs at 10 K and 290 K, as well as a cavity spectrum at 290 K with the first two TE modes visible. (b) TEM image of representative Si-NCs. (c) The PL spectrum of a representative fundamental cavity mode at 290 K, and the fit to a Lorentzian with $Q = 9,000$. (d) The polarization angle dependence of the cavity mode at 290 K, along with the angle dependence of PL from an unpatterned region. 0° corresponds to the y -direction of Fig. 2.3(d).	40
3.2	The Q s of nanobeam oxide cavities with Si-NCs at different wavelengths as a function of temperature.	41
3.3	(a) The Q s of the one set of cavities vs. the cavity wavelengths, at 10 K and 290 K. The PL from an unpatterned region of the sample is shown for reference. (b) The change in the cavity linewidth as the temperature is increased from 10 K to 290 K. Lower Q s at low temperature are attributed to the increase in Si-NC absorption, resulting from narrowing of the Si-NC linewidth.	43
3.4	The pump power dependence of the integrated intensity for different cavities at (a) 290 K and (b) 10 K. The amplitude traces of each cavity are offset by factors of 10 to allow clear viewing. The pump power dependence of the change in cavity wavelength (with respect to the low pump power wavelength, λ_0) for different cavities at (c) 290 K and (d) 10 K. Power dependences were taken with both the CW diode laser and the pulsed frequency-doubled Ti:Sapph. The pump power is measured in front of the objective.	45
3.5	The linewidths of representative cavities as the pump power is changed at (a) 290 K and (b) 10 K. Both a CW diode laser and a frequency doubled mode-locked Ti:Sapph laser are used as the pump source. The pump power is measured in front of the objective.	47

3.6	(a) The Si-NC density distribution of this sample as a function of Si-NC radius. (b) Time resolved measurements of the Si-NC rise and fall time. Fits to extended exponential distributions yield a rise time of 17 μ s and a fall time of 20 μ s for the sample at 290 K, and a rise time of 78 μ s and a fall time of 79 μ s for the sample at 10 K. (c) The excitation cross section and the lifetimes (τ_f) of the Si-NCs as a function of emission wavelength, for both 290 K and 10 K. (d) The calculated free carrier concentration as a function of pump intensity for 290 K and 10 K.	49
3.7	(a) The change in cavity linewidth as a function free carrier density for a representative cavity around 720 nm at 290 K and 10 K. Linear fits to the data are also shown. (b) The free carrier absorption cross-section (σ_{FCA}) obtained from linear fits such as those in part (a), as a function of wavelength, for different cavities throughout the PL spectrum of the Si-NCs. The inset shows the same data renormalized in a small V_m setting. The dashed lines represent fits to a λ^b model, where $b = 1.3$ and 1.8 for the 290 K and 10 K data, respectively.	51
3.8	(a) Photoluminescence from the cavity at room temperature and the unpatterned film at room temperature and 5.5 K. The whole membrane is composed of Er:SiN _x in this case (type I, shown in inset). (b) Spectrum of a cavity fabricated in SiN _x with only the middle third doped with Er (type II, shown in inset). Dots correspond to the spectrum obtained by a laser scan in cross-polarization reflectivity, and circles to PL measured by the spectrometer. Fits to a Lorentzian lineshape gives a $Q = 52,000$ from the reflectivity scan and a spectrometer resolution limited $Q = 25,000$	54
3.9	The pump power dependence of the (a) integrated PC cavity intensity and PL spectrally decoupled from the cavity, (b) the cavity resonance wavelength, and (c) the cavity Q , all at 5.5K and 290K. The pump power is measured in front of the objective lens.	56

3.10 (a) The Q s of the cavities at 5.5K and 290K, both with low pump power (less than $10 \mu\text{W}$). The dashed lines connect the data for the same cavity at the two different temperatures. The shift in wavelength between the two temperatures is most likely due to a shift of the sample position in the cryostat as temperature is varied. (b) The change in the linewidth (full-width at half-max, FWHM) for individual cavities as pump power is switched from less than $10 \mu\text{W}$ to 40 mW, at 5.5 K and room temperature. The scaled and shifted Er spectrum is shown in gray as a reference.	57
3.11 (a) Time-resolved PL measurements of the cavity resonance for various pump powers at ~ 3 K, as well as unpatterned film (integrated for all wavelengths). Solid lines for the cavity time traces are fits to a bi-exponential model. (b) The fast and slow components from the fits in part (a), as well as for an unpatterned film lifetimes for various pump powers.	59
3.12 (a) The difference in between the cavity linewidth at 5.5 K and 290 K, under high pump power (greater than 40 mW). The scaled and shifted Er spectrum is shown as a reference. (b) The absorption rate achieved at room temperature under high pump power (circles) and low pump power (squares) calculated by use of the cavity Q s measured in experiment, with error bounds assuming that the Er homogeneous linewidth at room temperature is between $\eta = 4$ and $\eta = 8$ times that at 5.5 K. (c) The absorption rate achieved at 5.5 K at high pump power (circles) and low pump power (squares), with the same error bounds as part (b). Regions with positive γ_a correspond to gain achieved with the system.	60
3.13 (a) The change in linewidth between 5.5 K and room temperature, both measured at low pump powers (below $10 \mu\text{W}$). The color of the points represents the intrinsic cavity Q -factor (Q_{cav}). The scaled and shifted Er spectrum is shown as a reference.	62

3.14 Normalized PL spectra from representative GaAs nanobeam cavities with embedded InAs QDs above lasing threshold (colored points). The PL spectrum from QDs in bulk (unpatterned film) is also shown (gray circles). The inset shows a zoomed-in cavity spectrum (pumped at 14 μ W, below the lasing threshold) and its fit to a Lorentzian lineshape, corresponding to $Q = 9,700$	64
3.15 The light-in light-out curves of a representative cavity, using CW pumping at (a) 980 nm and (b) 780 nm. Fits from the rate equations, and linear fits to the above threshold behavior are also shown. (c) The power dependence of the cavity wavelength with 780 nm and 980 nm pump. The red-shift at high pump powers indicates structure heating, and it kicks off sooner if the above-GaAs bandgap laser (780nm) is employed, as expected. The inset shows the cavity intensity for larger pump powers, where the beginning of saturation is observed toward the end of both traces. (d) The power dependence of the cavity linewidth with 780 nm and 980 nm pump. The pump power (horizontal axis) is measured before the objective in all cases.	66
3.16 The thresholds of various nanobeam lasers obtained by linear fit to the above threshold behavior, using both the 780 nm and the 980 nm pump. Threshold pump powers are measured before the objective lens in all cases. The Q s of various cavities (all below threshold) are also shown.	67
3.17 The light-in light-out curve for the same cavity as in Fig 3.15(a)-(b), pumped with a pulsed 830 nm laser, and by a CW 830 nm laser. The emission from a portion of the PL spectrum not coupled to the cavity is also shown. Pump powers are measured in front of the objective.	68

3.18 (a) Spectra from a nanobeam cavity as it is tuned by the movement of a fiber taper in close proximity to the cavity. The free space spectrum without the fiber taper is shown as a reference, and taper movement in the y - and z -directions (shown in Fig. 2.6) tunes the cavity mode by over 7 nm. The spectra for the tuned cavity are scaled for clarity. (b) The lasing thresholds of one cavity pumped from free space (normal incidence) and through the fiber taper, with collection through the fiber taper in both cases. The fiber taper position is varied to tune the lasing wavelengths. A reference case without any fiber tapers is also shown as the data point with the shortest wavelength. The inset shows the geometry simulated by FDTD, as well as the $ E ^2$ field of the cavity mode in the presence of the fiber taper.	70
4.1 (a) PL from the bulk Si-NC wafer (unprocessed, i.e., without metallic grating). (b) Experimental setup. (c) Fabricated gold grating, with p_1 and p_2 denoting the two polarizations selected in the experiments. . .	73
4.2 PL from Si-NCs near the grating for the (a) p_1 and (b) p_2 polarizations, from Fig. 4.1(a). (c) The ratio of PL spectra for the p_1 and p_2 polarizations. The second (diamond) and third (square) order mode wavelengths from FDTD are plotted again from Fig. 2.12(a). (d) PL_{p1}/PL_{p2} from Si-NCs coupled to the first order SPP grating mode. The FDTD calculated first order mode wavelengths are plotted again from Fig. 2.12(a).	75
4.3 (a) Biharmonic grating design, where a is the grating period that couples Si-NC to the SPP mode at π/a , and d is the duty cycle that can vary between 0 and 1. (b) The enhancement of the p_1 polarization by the biharmonic gratings. The first order mode wavelengths from FDTD are plotted again from Fig. 2.12(a). (c) Enhancement for one particular grating periodicity, with the red line being a Lorentzian fit of to data, representing quality factor $Q = 16$	76

4.4	(a) Top gold grating fabricated on the Er:SiN _x /Au substrate imaged by SEM. The double arrows indicate the approximate alignment of the polarizer (0°) (b) PL from on and off the grating structure, as well as from a reference sample with the same Er:SiN _x thickness grown on quartz. The same excitation power was used in all three cases. The region off the grating is a region with Er:SiN _x on top of Au without the top metal layer.	78
4.5	(a) The enhancement of integrated emission from grating structures relative to off grating areas, as a function of grating period. The three curves correspond to two different duty cycles (d), and to a biharmonic grating. (b) The enhancement of emission as a function of polarization angle for the resonant first and second order grating modes, as well as for the resonant biharmonic grating. The emission polarization angle dependence of the Er:SiN _x on Au off grating is also shown.	79
4.6	(a) The design of the square array of square metal particles. (b) The enhancement of emission from the shown nano-particle array structures relative to off-array areas, as a function of array period (a). (c) The angle dependence of the emission from a near-resonant nano-particle array with lattice constant of $a = 290$ nm.	81
4.7	(a) The enhancement of emission from a square array of square metallic particles (Fig. 4.6(a)), as the duty cycle (d) and lattice constant (a) are varied. (b) The same set of data is replotted against the particle width, $w = d \times a$	82

4.8 (a) Asymmetric particle arrays used to examine the role of inter-particle distance in the directions parallel and perpendicular to the plasmonic mode polarization. The vertical period v and horizontal period a are changed independently of each other. The polarization of the plasmonic resonances observed is shown by the double arrows. (b) The enhancement of emission from asymmetric particle arrays as a function of horizontal period a , while v is changed. Vertical period v is increased in increments of 200 nm. The particle has a width of $w = 0.8 a$, and height of $h = 0.4 v$ for all measurements. The horizontal period a that produces maximum enhancement remains the same for all v . (c) The enhancement of emission from arrays where v is fixed at 600 nm, h is fixed at 360 nm, and the horizontal width and period are varied independently.	83
5.1 (a) The cavities spectra measured in reflectivity from structures with different lattice constants are normalized and shown together, with fits to Lorentzian lineshapes plotted on top of the data points. The cavity spectra are shown from left to right with increasing a . (b) The Q s of the cavities shown in part (a) plotted against the wavelengths of the cavities. (c) The angle dependence of the reflectivity amplitude. The horizontal axis corresponds to the half-waveplate angle, which is placed in front of the objective lens that is in front of the chip (and thus placed in both the incident and collection paths). The fit to the reflectivity amplitude shows a period very close to $\pi/4$, indicating a linearly polarized cavity mode.	86
5.2 (a) SEM image of the fabricated structure with the alternative hole taper-out design. (b) The transmission spectrum of this cavity found with a broadband LED bank. The inset shows a laser scan of the fundamental cavity peak in transmission, along with a fit to a Lorentzian lineshape with $Q = 1.3 \times 10^5$	88

6.1	(a) Scanning electron microscope image of the fabricated cavity. The E_y field of the (b) $TE_{1,+}$ and (c) $TE_{2,+}$ optical modes. (d) The first order common in-plane mechanical mode, and (e) the first order differential in-plane mechanical modes are plotted with the color map assigned to the in-plane (y) motion.	91
6.2	(a) The optical setup used to probe the optomechanical cavity. (b) Spectrum of the cavity observed in transmission using a broadband LED. The first and second order bonded (+) and anti-bonded (−) modes are labeled. The inset shows a laser scan of the $TE_{1,+}$ cavity mode for excitation, with a fit to a Lorentzian lineshape having $Q \approx 15,000$	95
6.3	The RF spectrum of the mechanical modes under study in (a) ambient atmosphere, and in (b) vacuum. (c) The time averaged spectrum of the differential mechanical mode from part (b) is shown (green points), observed as RF sidebands of the laser tuned to $TE_{2,+}$. The non-averaged RF spectrum showing the sharp RF response when a modulated laser is pumped on $TE_{1,+}$ is also plotted (blue line). The inset shows the same data zoomed in, to observe the thermal driven mechanical mode in the background. (d) The integrated power within the sharp RF response of the laser on $TE_{2,+}$ [from (c)] with different RF modulation frequencies of the laser on $TE_{1,+}$. The two dotted curves correspond to two different average input powers on the first order mode and fixed input power on the second order mode. A closer zoom of the mode shown in part (b) of the figure is shown as a reference at the bottom (blue).	96

6.4 (a) The integrated intensity in the RF response collected from $\text{TE}_{2,+}$ as a function of average input power on $\text{TE}_{1,+}$ for different detunings of the RF modulation frequency from the mechanical resonance at a fixed probe power ($2 \mu\text{W}$) on $\text{TE}_{2,+}$. (b) The integrated intensity in the RF response as a function of different probe powers on $\text{TE}_{2,+}$, at two different fixed average pump powers on $\text{TE}_{1,+}$. (c) The RF response as a function of input power on $\text{TE}_{1,+}$ with different probe pump powers on $\text{TE}_{2,+}$. (d) The integrated RF response as a function of average pump power on $\text{TE}_{1,+}$. The two curves correspond to the response at ambient atmosphere and in vacuum, both with the same probe intensity on the $\text{TE}_{2,+}$ ($2 \mu\text{W}$).	98
B.1 The FDTD grid from Yee's algorithm. The (i, j, k) label the spatial coordinates of the grid, while the components of the E and H fields are labeled in color arrows.	108
B.2 (a) The time dependent H_z amplitude response of the cavity structure to different excitations. Broadband excitation, along with narrow band excitation for high Q cavity modes are shown. (b) The frequency response to the three excitations shown in part (a), obtained from a Fourier transform relation.	110
B.3 The nanobeam cavity structure is shown, along with the integrating surfaces for Q_{PC} , $Q_{ }$, and Q_{\perp} . For clarity, the bottom half of surfaces for Q_{\perp} are omitted.	111
C.1 The optical setup.	113
D.1 The theoretical average force on the mechanical mode for a fixed average input power of the modulated input, as a function of β	119

Chapter 1

Introduction

1.1 Optical Sources for Photonic Networks

In the information age, the need for bandwidth to pass data between computation centers has greatly increased. In addition to the growth of the fiber-optic communication bandwidth for long distance data transfer, the growth of the local data centers, computer clusters, and multi-core processors has motivated the development of optical communications for the short distances. Here, and especially for chip to chip communications, the optical interconnect has distinct advantages over conventional electrical interconnects as device sizes are decreased to increase the information density [1]. In particular, the resistance and time constant of wires transporting the electrical data increase as device dimensions are scaled down, leading to high energy costs for transporting information. On the other hand, the energy cost for optical interconnects is determined by the size of the transmitter and receiver, and could be decreased with the device design.

In addition to energy considerations, the establishment of electronic computation devices on a silicon complementary metal-oxide-semiconductor (Si-CMOS) platform requires that optical interconnects be silicon-compatible as well. Because silicon is an indirect bandgap material and not an efficient light emitter, there have been significant efforts to incorporate direct gap III/V materials with CMOS processing [2, 3]. An alternative to such fabrication is to develop devices that enhance the emission of novel

silicon-compatible materials. It would be feasible to combine such optical systems with electronics in a cost effective way, as drastic changes in existing electronics fabrication processes could be avoided. In addition to optical communications, silicon-compatible optical emitters can have a large impact in sensor, light, and display technologies.

The emission and control of light on such nanoscales could then be done by a variety of optical cavities [4]. The two key figures of merit for an optical cavity at frequency ω (and wavelength $\lambda = 2\pi c/\omega$, where c is the speed of light) are the quality (Q -) factor and the mode volume (V_m). The Q -factor of the cavity is defined in terms of the energy decay of the cavity, which goes as $\exp(-\omega t/Q)$. Using a Fourier transform of the decaying electric field at frequency ω , the Q -factor can also be defined in the optical spectrum of the cavity as $Q = \omega/\Delta\omega \approx \lambda/\Delta\lambda$, where $\Delta\omega$ and $\Delta\lambda$ are the full-width at half-max (FWHM) of the cavity spectrum in the frequency and wavelength domains, respectively. The high- Q cavity could also be used to spectrally filter signals and define operating wavelengths from a broad emission source. In total, the Q factor is a measure of the temporal confinement of the photons. On the other hand, the mode volume of the cavity is a measure of the volume that the photonic field occupies when confined to the cavity. It is defined as:

$$V_m = \frac{\int \epsilon(\vec{r}) |E(\vec{r})|^2 dV}{\max[\epsilon(\vec{r}) |E(\vec{r})|^2]}, \quad (1.1)$$

where $E(\vec{r})$ is the spatial distribution of the electrical field of the cavity mode, $\epsilon(\vec{r})$ is the dielectric structure of the cavity. In short, it measures the spatial confinement of photons in the cavity.

In particular, increasing Q and decreasing V_m increases the light-matter interaction inside of a photonic cavity. In the weak-coupling, or Purcell, regime of cavity quantum electrodynamics (cQED), the spontaneous emission (SE) rate of an emitter coupled to a cavity is enhanced by the Purcell factor, defined as [5]:

$$F = \frac{3}{4\pi^2} \left(\frac{\lambda}{n} \right)^3 \frac{Q}{V_m} \overline{\psi(\theta, \vec{r}, \nu)}, \quad (1.2)$$

where $\overline{\psi(\theta, \vec{r}, \nu)}$ includes the decrease of enhancement for spatially and spectrally detuned emitters from the cavity mode. Defined for a dipole emitter with frequency ν (spectrally detuned from the cavity frequency, ω) at a position \vec{r} that forms an angle θ with the cavity \vec{E} -field at the same position, $\psi(\theta, \vec{r}, \nu)$ takes the form:

$$\psi(\theta, \vec{r}, \nu) = \left| \frac{E(\vec{r})}{E_{max}} \right|^2 \frac{(\nu/(2Q))^2}{(\nu - \omega)^2 + (\nu/(2Q))^2} \cos^2(\theta), \quad (1.3)$$

where E_{max} is the E -field amplitude at the location of the maximum E -field energy density, $\epsilon|E|^2$. Intuitively, enhancing Q increases the photon storage time, while decreasing V_m increases the local photon energy density, both increasing the interaction (emission and absorption) between the emitter and photons in the optical cavity mode. Finally, in a different interpretation, the cavity modifies the local density of states. From the energy decay of the cavity, the density of states for the cavity can be found as:

$$S(\nu) = \frac{1}{\pi} \frac{\nu/(2Q)}{(\nu - \omega)^2 + (\nu/(2Q))^2}. \quad (1.4)$$

At the cavity resonance ($\nu = \omega$), the density of states is proportional to the cavity Q and is increased above the free space value. Thus, using derivations such as Fermi's Golden Rule, the spontaneous emission of emitters into the cavity mode can be increased [6].

In experiments, under a continuous-wave (CW) pump source, the increased spontaneous emission rate allows more photons to be emitted per unit of time, and thus increases the emission efficiency of the emitters inside of a cavity. In addition, the increased Q and reduced V_m reduce the lasing threshold for active materials, as the increased photon storage time enhances stimulated emission processes, while the reduced mode volume allows inversion with reduced pump power. Finally, cavities of small V_m enable fast direct modulation speeds exceeding 100 GHz [7, 8], which have the potential to be used in opto-electronic communications.

1.2 Photonic Crystal Cavities

The photonic crystal (PC) cavity system, with high Q -factor and low V_m , could be employed to enhance the spontaneous emission rate via Purcell enhancement and reduce the threshold to lasing. First proposed by Yablonovitch [9] and John [10], the photonic crystal is a structure with a periodic variation in dielectric constant. Much like how periodic arrangements of atoms and electron wavefunctions in solids lead to a bandgap in allowed energies for electronics, period arrangements of the dielectric constant lead to a photonic bandgap in the allowed energies for photons. This photonic bandgap can be used to direct light, as photons with energies inside of the bandgap will be reflected by the photonic crystal structure.

In particular, the energy eigenstates of the electromagnetic field inside of a photonic crystal can be found by solving the Maxwell eigenvalue equation [11]:

$$\nabla \times \left(\frac{1}{\epsilon(\vec{r})} \nabla \times H(\vec{r}) \right) = \left(\frac{\omega}{c} \right)^2 H(\vec{r}), \quad (1.5)$$

where $H(\vec{r})$ is the spatial distribution of the magnetic field for a mode supported by a dielectric structure $\epsilon(\vec{r})$. For photonic crystals, $\epsilon(\vec{r})$ is periodically varying in one (1D), two (2D), or three dimensions (3D). The periodicity of the material system creates coupling between forward and backward propagating waves with certain wavevectors k and frequencies ω , and for certain ranges of the ω - k relationship, can enable fully coherent reflection in a process known as distributed Bragg reflection (DBR). Although 3D PCs can confine light in all directions and their fabrication has been recently improved (including high Q cavities) [12, 13, 14, 15, 16], the fabrication process for these multi-layered structures is extremely difficult. Similarly, 1D PCs have been used in vertical cavity surface-emitting lasers (VCSEL) design [17], but require very well controlled growth of multilayer structures. In this thesis, we focus on 1D or 2D cavities that are fabricated in a one step lithography and etching process to form suspended membranes. Because 1D and 2D PCs only confine light in the direction with periodic dielectric constant, total internal reflection (TIR) arising from the index contrast between the slab material and the surrounding medium is

used to confine light in the remaining directions.

The basic photonic crystal cavity system is shown in Fig. 1.1(a), where a three hole defect is formed in a periodic triangular lattice of air holes in a dielectric slab. By solving Eqn. 1.5 in this system for the possible directions of propagation in the plane of the membrane in the PC region, we obtain the energy band diagram of the photonic system shown in Fig. 1.1(b), for the transverse-electric (TE-) like polarization, which has non-zero components in only (E_x, E_y, H_z) on the midplane of the z -direction, where E_x and E_y are in the plane of the membrane, and H_z field perpendicular to the plane of the membrane. The high symmetry directions of the triangular lattice, which forms the boundary of the irreducible Brillouin zone in the reciprocal lattice space (Fig. 1.1(a), inset) is plotted along the x-axis. The solid lines in this plot correspond to the light line. The gray region of the band diagram (known as “above the light-line”) denotes the region where TIR does not confine photons in the direction normal to the plane of the membrane. Below the light-line, we see a range of energies where no photonic modes exist, and thus a range of energies where the PC would confine light through DBR. Because the photonic bandgap exists for all directions below the light-line, photons confined to the cavity region would not be able to escape through photonic crystal in direction parallel to the plane of the membrane. Thus, the confinement of a PC cavity is limited by the radiation lost in the directions not confined by the DBR, i.e., the cavity field components located above the light-line. However, designs to manipulate the spatial profile of the cavity mode and minimize radiation in above light-line directions have been implemented to improve Q -factors [18, 19].

From the picture in Fig. 1.1(b), we also observe that the lattice constant that creates a band gap is generally on the order of $a \approx \lambda/n$, where n is the refractive index of the PC slab material. Such a relationship should not be surprising, as it arises from the diffraction limit of electromagnetic waves in a dielectric medium. With proper design, the V_m of PC cavities is expected to be below of $(\lambda/n)^3$. Compared to other cavities, such as the micropillar ($Q = 2,000$, $V_m > 5(\lambda/n)^3$), microdisk ($Q > 10^4$, $V_m > 6(\lambda/n)^3$), microtoroid ($Q > 10^8$, $V_m \approx 10^2(\lambda/n)^3$), and microsphere ($Q > 10^9$, $V_m > 10^3(\lambda/n)^3$), the photonic crystal cavity offers a different regime of moderate Q

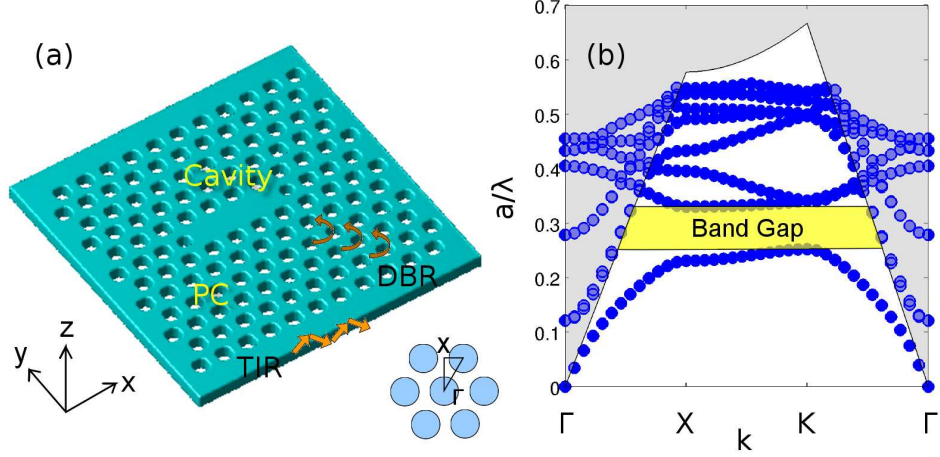


Figure 1.1: (a) The 2D PC cavity system in a suspended membrane, with the cavity defect and the periodic air holes that form the triangular lattice photonic crystal. TIR confines the light in the out-of-plane directions of the membrane, while DBR confines the light in the directions in the plane of the membrane. The inset shows the irreducible Brillouin zone in the reciprocal space for the triangular lattice, along with the labeled high symmetry points. (b) A representative band diagram for the TE-like polarization along the high-symmetry directions, for a slab with index of refraction $n = 3.5$. The solid line is the light-line, which separates the states confined by the total internal reflection (below the line) from those that leak in the direction perpendicular to the membrane. The optical bandgap is seen below the light line and between normalized frequencies $a/\lambda = 0.25$ and 0.33 .

and low V_m , which is useful in quantum optical and Purcell regime work [4].

1.3 Plasmonic structures

An alternative to enhance emitters in the Purcell regime is the use of surface plasmon-polariton (SPP) modes. As stated above, the mode volume of photonic modes confined by DBR and TIR are diffraction limited from below to $\approx (\lambda/2n)^3$. However, evanescent surface modes bound to an interface can break the diffraction limit. The SPP is a mode that stores its energy in electromagnetic fields and electronic charge oscillation [20]. It is an evanescent mode bound to metal-dielectric interface and supported by a surface charge at the interface. It has TM polarization, where a

scalar H -field is parallel to the plane of the interface [Fig. 1.2(a)]. By employing SPP cavities in solid-state, we could attempt to achieve the same or even higher SE rate enhancement compared to photonic designs (as a result of smaller V_m), but with simplified fabrication. However, due to ohmic losses in the metal, SPP modes often have broad spectra and low Q s, which is advantageous for some applications, such as when “bad emitters” with broad homogeneous linewidths are employed. In that case, Purcell enhancement is limited by the quality factor of the emitter (inversely proportional to the emitter linewidth) or the quality factor of the cavity, whichever is lower [21]. The homogeneous linewidth of Er ions at room temperature, for example, is several nanometers [22], and thus limits the effective Purcell enhancement despite coupling to high- Q cavities. In such a case, broadband enhancement (resulting from low modal Q) could produce higher overall enhancements. Furthermore, enhancements from photonic crystal cavities are limited to emitters near the spatial maximum of the cavity mode and spectrally coupled to the narrow cavity bandwidth, where the $(E(\vec{r})/E_{max})^2$ and Lorentzian spectral terms in Eqn. 1.3 are respectively significant. Hence, large area and broadband enhancement are difficult to achieve. On the other hand, SPP modes can be designed for large surfaces, and again due to the broadband enhancement, can produce higher enhancements than photonic modes.

The surface plasmon dispersion relation is given by [20]:

$$k_{sp} = \frac{\omega}{c} \sqrt{\frac{\epsilon_d \epsilon_m(\omega)}{\epsilon_d + \epsilon_m(\omega)}}, \quad (1.6)$$

where k_{sp} is the wave-vector of the plasmon mode, ω is the mode frequency, $\epsilon_d = n^2$ is the dielectric constant of the dielectric material, $\epsilon_m(\omega) = 1 - (\omega_p/\omega)^2$ is the dielectric constant of the metal described by the Drude model, and ω_p is the bulk plasma frequency of the metal. The dispersion relation plotted for SPP modes on a flat gold metal surface facing air ($n = 1.0$) is shown in Fig. 1.2(b), along with the light-line for air. For small k -vectors, the dispersion approaches the light-line, $\omega = k_{sp}c/n$, while at high k -vectors, the dispersion relation asymptotically approaches $\omega = \omega_{sp} = \omega_p/\sqrt{1 + \epsilon_d}$, which is known as the surface plasmon frequency. The inverse decay

length of the SPP mode in the dielectric material is:

$$\kappa = \frac{\omega}{c} \sqrt{\frac{\epsilon_d^2}{|\epsilon_d + \epsilon_m(\omega)|}}, \quad (1.7)$$

which is in general comparable to n/λ at small k -vectors, but drastically increases as frequency approaches ω_{sp} .

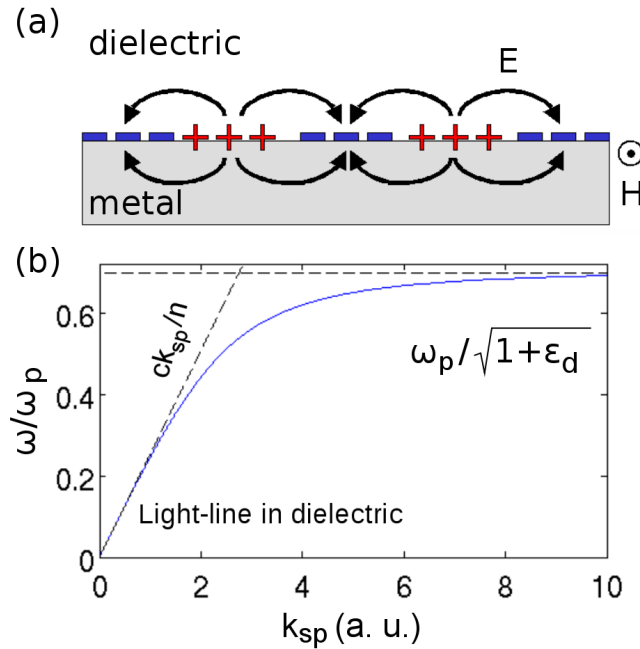


Figure 1.2: (a) Depiction of the SPP mode. (b) The dispersion relationship for the SPP modes on a gold-air interface. The light-line ($\omega = ck_{sp}$) and ω_{sp} (where ω_p is the bulk plasma frequency) asymptote are also shown.

Because the dispersion relationship of the SPP mode on a flat metal-dielectric interface flattens near the frequency ω_{sp} , modes at high k -vector represent modes that travel at slow group velocity. In addition, because these modes are grouped closely in frequency, the density of states at ω_{sp} is high. In recent years, various materials have been coupled to this region of high density of optical states, including InGaN based quantum wells [23, 24] and CdSe colloidal quantum dots [25], with observations of increases in the spontaneous emission rate. These experiments were

done by matching the surface plasmon frequency to the emitters' emission frequency, often by manipulating the index of refraction of the material in contact with the metal surface. In order to efficiently extract emission and to diversify the SPP enhancement over a range of wavelengths, several groups have investigated grating type structures combined with quantum wells or organic materials [26, 27, 28, 29]. Finally, other groups have proposed and demonstrated coupling emitters to metallic nanowires and nanotips, where the tight confinement of the mode (the reduction of V_m) enables high Purcell enhancements [30, 31, 32, 33].

We introduce various types of light emitting materials that have been employed in the experiments of this thesis.

1.3.1 Silicon Nanocrystals

The system of silicon nanocrystals (Si-NCs) embedded in a silicon dioxide (SiO_2 , or silica) host has been proposed as a silicon-compatible light emitter. As such, this material is a viable option for building an inexpensive Si-CMOS compatible light source for optical communications, interconnects, or solid-state lighting purposes. These crystalline particles can be fabricated by a variety of methods, including laser ablation [34], Si implantation [35, 36], or plasma enhanced chemical vapor deposition (PECVD) [37]. Regardless of the method, the general principle is that Si above the stoichiometric ratio is inserted into the oxide matrix, and a high temperature annealing step phase segregates the silicon from the silicon dioxide, leaving silicon nanocrystals in the oxide matrix. Because of the excess silicon, this material is often referred to as silicon-rich oxide (SRO). The excess silicon content of the material can be tuned by varying deposition conditions, and the index of the material can vary between 1.6 to 2.0. Although bulk silicon is an indirect bandgap material and is a poor emitter of light, nanocrystalline particles of silicon relax some constraints for radiative recombination, as the quantum confinement of the electronic wavefunction broadens the electron wavefunction in k -space and enhances radiative transitions at the zone center.

The Si-NCs demonstrate photoluminescence (PL) in a wide range of wavelengths,

depending on the pump wavelength and fabrication procedures. By tuning the size of the nanocrystals, the emission of the Si-NCs can be tuned from the ultraviolet to the near infrared (300 - 1000 nm) [38, 39]. In addition, there have been several reports of amplified spontaneous emission (ASE) and gain in this material [36, 37]. Although the origin of the PL and stimulated emission has been attributed to both quantum confined states and surface states, the demonstrations of ASE makes the material promising for optical devices. However, free carrier absorption has also been closely studied in this material [37], and its effect on the available optical gain has not been fully determined. Finally, electroluminescence has also been demonstrated with this material [40], and making integration with Si-electronics even more promising.

1.3.2 Erbium doped Silicon Nitride

Erbium (Er)-doped materials also have potential as light sources in optoelectronics due to emission at the telecommunication wavelength of $1.54 \mu\text{m}$. The Er-doped materials have similar properties to the erbium-doped fiber amplifier (EDFA), with a wide spectrum of gain from the 4f level around the telecommunication wavelengths (in fact, the C-band from 1530 nm to 1570 nm is also known as the “Erbium window”). In addition, Er doped (sub-stoichiometric) silicon oxide (SiO_x) and nitride (SiN_x) can be integrated with silicon complementary metal-oxide-semiconductor (CMOS) electronics, potentially serving as light sources for on-chip or off-chip communications. Because the 4f transition has a small oscillator strength and correspondingly slow radiative lifetimes, there have been many attempts to improve its emission intensity. Recently, there has been significant work on the material properties of Er-doped materials. The material systems of Er sensitized by silicon nanoclusters in SiO_x [41, 42], Er doped amorphous silicon nitride (Er:SiN_x) [43, 44, 45, 46, 47], and Er doped SiN_x -Si superlattices [48] have all demonstrated an increase in emission and a reduction of non-radiative decay under optical pumping. For example, Er emission from Er doped in an amorphous nitride matrix (Er:SiN_x) can be sensitized by the host through a nanosecond-fast energy transfer mechanism, which provides an absorption cross-section four orders of magnitude larger than that of Er in silica (SiO_2) [43, 44].

Low field electrical injection in this material is also possible, as demonstrated by electroluminescence of silicon nanocrystals in silicon-silicon nitride superlattices [49, 50].

1.3.3 InAs Quantum Dots

The growth of InAs quantum dots (QDs) in a GaAs host has been studied in detail [51]. One growth method for these dots is the self-assembly method, where a thin layer of InAs is grown on GaAs (which has a different lattice constant than InAs) and the QDs are subsequently formed to relieve the strain from the lattice mismatch. Being formed from III-V materials, InAs QDs have a direct bandgap, are efficient emitters of light, and have a high gain coefficient. The dots are on the order of 10 nm in the lateral dimension and a few nanometers in the growth (out-of-plane) direction. By controlling the strain, the QD size, and the Ga content of the QDs, QD emission can be tuned from 900 nm [52, 53] to 1300 nm [54, 55]. The use of quantum dot active material inside PC cavity lasers to further lower the lasing threshold (by minimizing non-radiative surface recombination effects and enhancing the emission rate through Purcell enhancement) has been studied [52, 53, 54, 55, 56]. Due to its low non-radiative decay rates, the InAs QD can also be used for a variety of quantum optics and quantum information applications [57, 58].

1.4 Thesis Outline

The outline of the thesis is as follows: Chapter 2 describes the theoretical design of various photonic crystal and plasmonic structures used to enhance emission from silicon compatible materials. Chapter 3 describes the experimental coupling of 1D PC cavities to various silicon compatible emitters and quantum dots. Chapter 4 describes the experimental coupling of plasmonic grating structures to silicon compatible emitters. Chapter 5 describes the implementation of the nanobeam cavity design for passive structures with various indices of refraction. Chapter 6 describes the measurement and actuation of mechanical modes in photonic crystal cavities by

optical forces. Finally, Chapter 7 offers conclusions and outlooks for the various works in this thesis.

The topics in these chapters can be broken down into design and implementation of photonic crystal cavities or plasmonic structures. The relevant publications for photonic crystal experiments (Sections 2.1.1-2.1.4, Chapter 3, Chapter 5, Chapter 6) are:

- (1-2 equal contribution) Y. Gong, M. Makarova, S. Yerci, Rui Li, M.J. Stevens, B. Baek, S. W. Nam, R.H. Hadfield, S.N. Dorenbos, V. Zwiller, J. Vuckovic, and L. Dal Negro. Linewidth narrowing and Purcell enhancement in photonic crystal cavities on an Er-doped silicon nitride platform. *Optics Express*, 18(3):2601-12, JAN 2010.
- Y. Gong and J. Vuckovic. Photonic crystal cavities in silicon dioxide. *Applied Physics Letters*, 96(3):031107, 18 JAN 2010.
- Y. Gong, B. Ellis, G. Shambat, T. Sarmiento, J. S. Harris, and J. Vuckovic, Nanobeam photonic crystal cavity quantum dot laser. *Optics Express*, 18(9):8781-8789, APR 2010.
- Y. Gong, S. Ishikawa, S.-L. Cheng, M. Gunji, Y. Nishi, and J. Vuckovic. Photoluminescence from silicon dioxide photonic crystal cavities with embedded silicon nanocrystals. *Physical Review B*, 81(23):235317, MAY 2010.
- Y. Gong, M. Makarova, S. Yerci, R. Li, M. J. Stevens, B. Baek, S. Woo Nam, L. Del Negro, and J. Vuckovic. Observation of transparency of ering of plasmonic grating structures to silicon compatible emittebium-doped silicon nitride in photonic crystal nanobeam cavities. *Optics Express*, 18(13):13863-13873, MAY 2010.

The relevant publications for the design of plasmonic structures and experimental coupling of active materials to plasmonic modes (Sections 2.2.1 - 2.2.3, Chapter 4) are:

- Y. Gong and J. Vuckovic. Design of plasmon cavities for solid-state cavity quantum electrodynamics applications. *Applied Physics Letters*, 90(3):33113-1-3, 15 JAN 2007.
- Y. Gong, J. Lu, S.-L. Cheng, Y. Nishi, and J. Vuckovic. Plasmonic enhancement of emission from Si-nanocrystals. *Applied Physics Letters*, 94(1):013106, 5 JAN 2009.
- Y. Gong, S. Yerci, R. Li, L. Dal Negro, and J. Vuckovic. Enhanced light emission from erbium doped silicon nitride in plasmonic metal-insulator-metal structures. *Optics Express*, 17(23):20642-20650, 26 OCT 2009.
- (1-2 equal contribution) M. Makarova, Y. Gong, S.-L. Cheng, Y. Nishi, S. Yerci, R. Li, L. Dal Negro, and J. Vuckovic. Photonic Crystal and Plasmonic Silicon-Based Light Sources. *IEEE Journal of Selected topics in Quantum Electronics*, 16(1):132-140, JAN-FEB 2010.

Chapter 2

Design of Photonic Crystal Cavity and Plasmonic Cavity Structures

2.1 One dimensional Nanobeam Photonic Crystal Cavity

Two dimensional photonic crystal membranes have been well established in photonics research, as they can be fabricated by standard microfabrication techniques, and their 2D photonic bandgap provides strong DBR confinement in all in-plane directions. By proper design of the spatial profile of the photonic modes, extremely high Q -factors have been achieved [18]. These designs modulate the index of refraction in a waveguide system, and $Q_s > 10^6$ have been theoretically and experimentally achieved in a high index material (silicon, $n = 3.5$) [18, 59, 60]. In addition, moderate Q cavities have been proposed in low index materials such as diamond ($n = 2.4$) [61, 62] and silicon nitride (Si_3N_4 , $n = 2.0$) [63, 64], with experimental $Q > 3,000$. Whereas a full photonic band gap in a 2D photonic crystal is difficult to achieve in low index materials, one dimensional (1D) nanobeam cavities can achieve photonic bandgaps in the direction of the periodicity with small index contrast due to the reduced dimensionality, while relying on total internal reflection in directions perpendicular to the beam length [65]. Recent developments in 1D nanobeam cavities with “potential

“well” designs have achieved the same Q -factors in silicon as in 2D photonic crystal cavities with comparable mode volumes [66], while also opening the door for high- Q cavities in Si_3N_4 for applications of optomechanics [67] and coupling to active materials [68]. In particular, the experimentally demonstrated Q s exceed 10^5 for Si [66] and 10^4 for Si_3N_4 ($n = 2.0$) [67], while maintaining $V_m < 2.0(\lambda/n)^3$. We develop designs for low-index materials ($n = 1.46$ to $n = 2.0$) [69], which are hosts to a variety of active materials (e.g. Si nanoparticles in SiO_2), and whose emission can be enhanced in the Purcell regime of high Q , low V_m cavities. Such silicon-compatible cavities also present an interesting platform for applications such as sensors, as due to their poor index contrast with surrounding air, the cavity modes have high overlap with the environment.

2.1.1 Nanobeam Cavity in Silicon Dioxide

First, we design 1D nanobeam cavities in silicon dioxide (SiO_2 , or silica), which has a low index of refraction $n = 1.46$. Unlike silicon, which absorbs heavily in the visible wavelength range, silica is transparent and can be used for applications in visible lighting. Silica is also a heavily used material in electronics, has low cost, and has established fabrication techniques. We follow the cavity design used in Si and Si_3N_4 [67, 70], but consider a silica slab suspended in free space, with lattice constant a , width w , slab thickness d , hole width h_x , and hole height h_y , as shown in Fig. 2.1(b). We first obtain the band diagram of a periodic (or unperturbed) nanobeam waveguide using the three dimensional (3D) finite difference time domain (FDTD) method with Bloch boundary conditions. The FDTD method is described in Appendix B. A sample band diagram is shown in Fig. 2.1(c) for a beam with parameters: lattice constant a , $w = 3a$, $d = 0.9a$, $h_x = 0.5a$, and $h_y = 0.7w$, and also for a beam with the same parameters, except with lattice constant $a' = 0.9a$. The high symmetry points for periodicity in one direction are the Γ point at $k = 0$ and the X point at the edge of the irreducible Brillouin zone, $k = \pi/a$ [Fig. 2.1(c)]. As expected, the structure with the smaller lattice constant has slightly higher band frequencies, as this structure supports modes that have higher overlap with air. Because the lowest

band of the structure with lattice constant a' (mode at the π/a' point) lies in the band gap of the structure with lattice constant a , it can serve as the defect mode in a beam with lattice constant a , which acts as the photonic crystal mirror. We also notice that the bands flatten near the Brillouin zone edge, corresponding to modes of small group velocity, much like the analogous slow electron group velocity at the edge of an electronic band diagram. This slow group velocity effect also helps confine the defected mode in the cavity region.

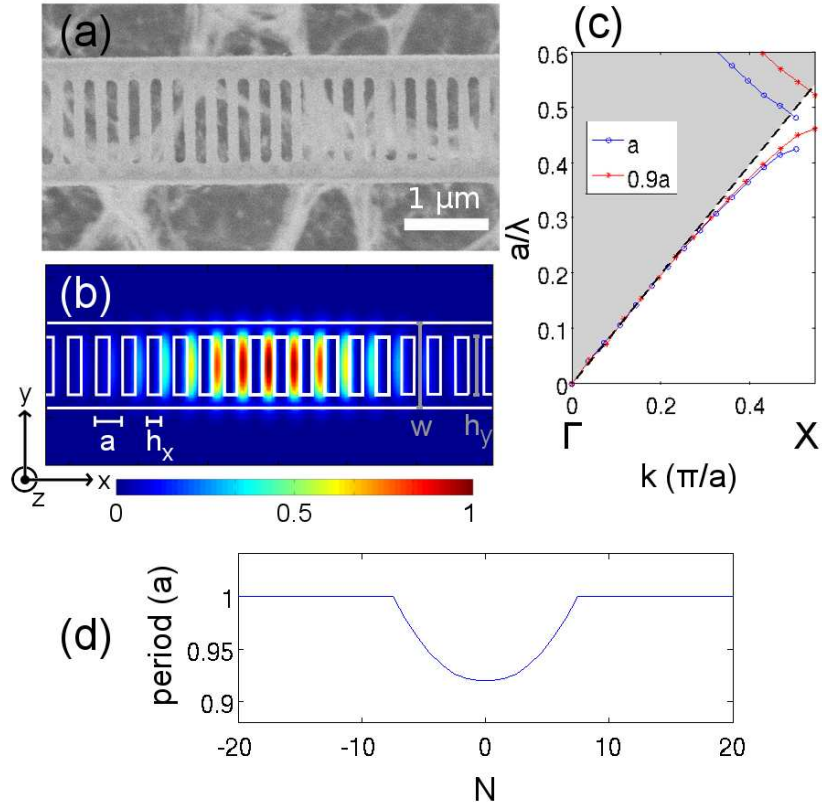


Figure 2.1: (a) The fabricated 1D nanobeam cavity in silica (SiO_2 , $n = 1.46$) imaged in an SEM. (b) The electric field intensity ($|E|^2$) of the fundamental mode supported by the cavity. (c) Band diagram for a beam with lattice constant a , $w = 3a$, $d = 0.9a$, $h_x = 0.5a$, and $h_y = 0.7w$, and another beam with the same parameters except for lattice constant $a' = 0.9a$. The dashed line indicates the light line in free space. (d) Design of the cavity. The plot shows the period (a) along the length of the beam as a function of N , the layer number counted from the center of the cavity.

Next, we use the perturbation design suggested by previous references and introduce a parabolic relationship between the lattice constant and the x -coordinate, thus forming an optical potential well [71]. In particular, we choose a minimum effective lattice constant of $0.90a$ at the center of the potential well, and the remainder of the lattice constants as shown in Fig. 2.1(d). The perturbations of lattice constants span 7 periods away from the center of the cavity. We simulate the full cavity structure again using the FDTD method, with $a = 20$ program units and perfectly matched layer (PML) absorbing boundary conditions, and obtain the fundamental TE-like mode with frequency $a/\lambda = 0.454$, $Q = 1.6 \times 10^4$, $V_m = 2.0(\lambda/n)^3$, and electric field intensity ($|E|^2$) shown in Fig. 2.1(b). This represents a more than one order of magnitude increase in Q -factor and a 7 fold reduction in mode volume compared to a $5\text{ }\mu\text{m}$ diameter silica microdisk (or microdisk made of SRO, with $n = 1.8$ [72]) cavity with the same silica thickness, again obtained in FDTD simulations. While silica micro-disks with $Q = 10^5$ have been achieved [73], such microdisks have dimensions much larger than the nanobeam cavities studied here.

We also simulate the effect of the number of photonic crystal mirror layers on the cavity Q . In particular, we define the quality factor in the direction \hat{i} as $Q_i = \omega U/P_i$, where ω is the frequency of the mode, U is the total energy of the mode, and P_i is the power radiated in the \hat{i} direction, computed by taking the integral of the time averaged Poynting vector across a plane (details in Appendix B). We separate $Q_{tot} = 1/(1/Q_\perp + 1/Q_\parallel + 1/Q_{PC})$, where Q_{PC} corresponds to radiation leaked through the ends of the silica beam [in the x direction of Fig. 2.1(b)], Q_\parallel corresponds to radiation leaked out of the beam transverse to the long axis of the beam within the $z = \pm d/2$ plane (in the y direction), and Q_\perp corresponds to the remaining radiation leaked transverse to the beam long axis (in the z direction) [71]. We plot the dependence of the various Q s as a function of the number of layers of photonic crystal mirrors in Fig. 2.2(a). We see that the gentle confinement method enables high reflectivity mirrors even in silica, as Q_{PC} continuously increases with the addition of more PC mirror layers. In the case of a 1D nanobeam, Q is limited by loss in the directions where the mode is confined by total internal reflection, namely Q_\perp and Q_\parallel . As seen in Fig. 2.2(a), the limiting factor in Q_{tot} is Q_\perp in this case. Thus,

Q_{tot} could be increased by improving the design of the periods that correspond to the photonic crystal cavity, possibly by parameter search, genetic algorithms [74], or inverse designs [19, 75].

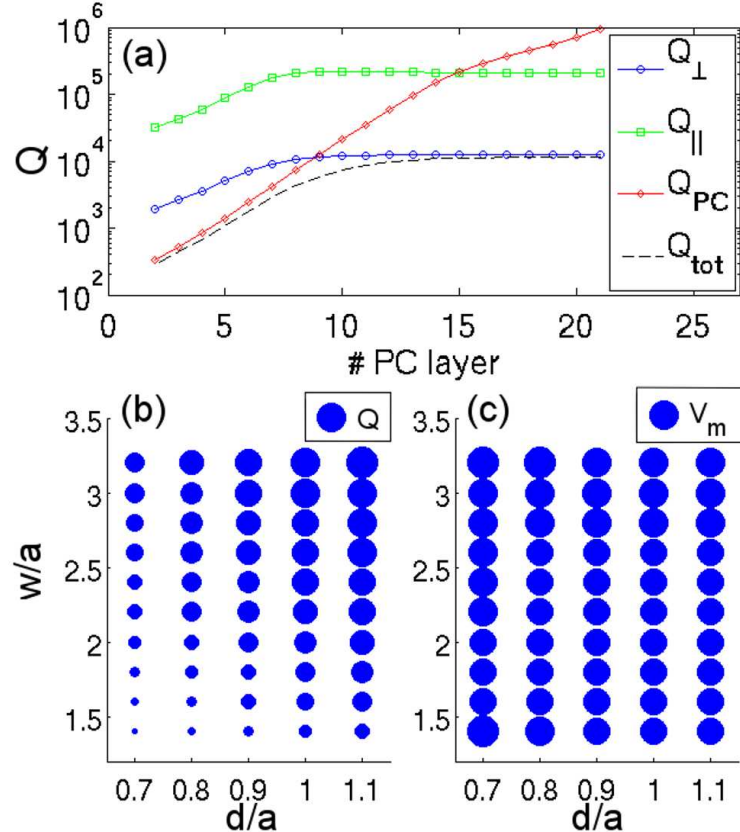


Figure 2.2: (a) The direction specific Q -factors of the silica nanobeam cavity as a function of the number of photonic crystal mirror layers surrounding the cavity. With respect to Fig. 2.1(b), Q_{\perp} corresponds to radiation leaked in the z direction, $Q_{||}$ corresponds to radiation leaked in the y direction, and Q_{PC} corresponds to radiation leaked in the x direction. Q_{tot} is the parallel sum of Q_{\perp} , $Q_{||}$, and Q_{PC} . (b) The Q -factors and (c) the mode volumes of cavities with the same air hole design, but different beam widths and thicknesses. The reference dot sizes are for $Q = 2.0 \times 10^4$ and $V_m = 2.0(\lambda/n)^3$ in (b) and (c), respectively.

Furthermore, we simulate the cavity with the same pattern of holes in the x -direction, while changing the beam width w and thickness d , keeping $h_x = 0.5a$ and $h_y = 0.7w$. The resulting limiting Q (the parallel sum of Q_{\perp} and $Q_{||}$) and V_m are

shown in Fig. 2.2(b) and (c), respectively. We see that both the Q -factor and V_m increase with the slab width and thickness, which is expected as larger cavities have higher confinement but higher mode volumes. In fact, we observe that for small widths and thickness [lower left of Fig. 2.2(b) and (c)], the cavity mode is not as well confined to the center of the beam. Such a trade-off between Q and V_m is also present in other types of cavities, including 2D PC cavities and μ -disk systems. In order to employ this cavity in cQED applications, we need to maximize the Q/V_m ratio. Such a maximum is achieved with $w = 2.6a$ and $d = 1.1a$, with $Q = 2.0 \times 10^4$ and $V_m = 1.8(\lambda/n)^3$.

2.1.2 Nanobeam Cavity in Silicon Rich Oxide

We extend the same design to the silicon rich oxide material, with index of refraction $n = 1.7$. The cavity extends 6 air holes on either side of the center of the cavity, where the distance between air holes is $0.9a$ at the center of the cavity, while holes outside of the cavity in the photonic crystal mirror have lattice constant a . The design maintains air holes with horizontal size $h_x = 0.5a$ and vertical size $h_y = 0.7w$ [Fig. 2.3(a)]. We again simulate the cavity using the 3D-FDTD method, with a discretization of 20 units per lattice constant and apply perfectly matched layer absorbing boundary conditions. For a cavity with $d/a = 0.7$ and $w/a = 3.2$, and assuming the Si-NC doped oxide material to have an index of refraction of $n = 1.7$, we find that the cavity supports at least three TE-like modes, which have dominant E_y field profiles shown in Fig 2.3(b)-(d), and are referred to as the first (TE_0 , or fundamental), second (TE_1), and third order (TE_2) modes, respectively [71]. The TE_0 , TE_1 , and TE_2 modes have normalized mode frequencies of $a/\lambda = 0.417$, 0.398 , and 0.385 , respectively, with the electric field energy of higher order modes occupying regions on the beam with increasing lattice constants (and thus lower frequency waveguide modes). We again compute the Q of the cavity from the radiated power of the cavity, and we find that the TE_0 , TE_1 , and TE_2 modes have radiation limited Q s of 2.0×10^4 , 1.3×10^4 , and 2.9×10^3 , and mode volumes of $1.6(\lambda/n)^3$, $2.5(\lambda/n)^3$, and $4.4(\lambda/n)^3$, respectively, for a reference index of $n = 1.7$.

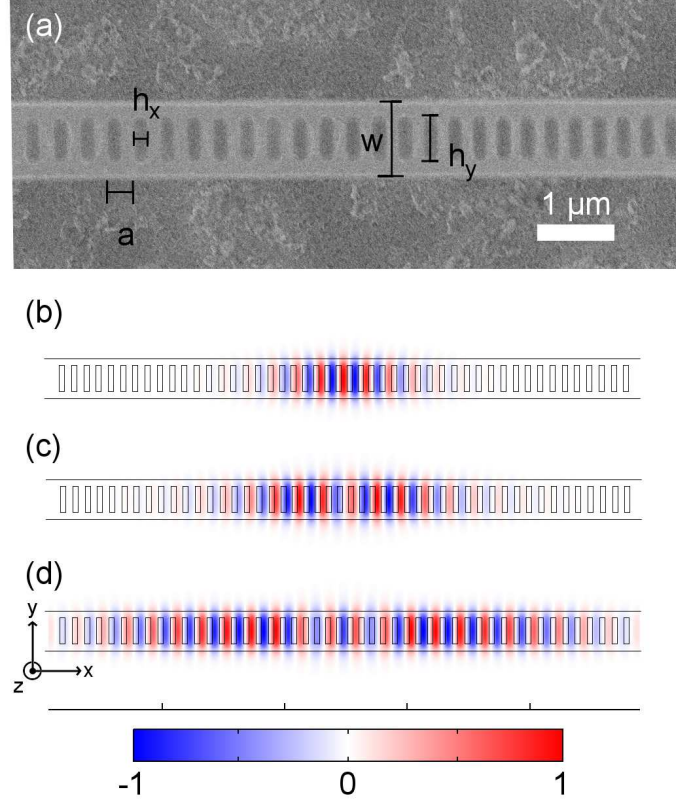


Figure 2.3: (a) SEM image of the fabricated beam structure. The E_y component of the (b) first- (c) second- and (d) third-order TE-like modes supported by the nanobeam with parameters $w = 3.2a$, $h_x = 0.5a$, $h_y = 0.7w$, and thickness $d = 0.7a$ are also shown. The beam material has index $n = 1.7$.

We also vary the width (w) and thickness (d) of the beam with the same fixed air hole design, and find Q and V_m for different beam parameters, shown in Fig 2.4(a) and (b), respectively. Much like the simulations for the lower index silica, for $w < 2.4a$, we find that the confinement of the mode (and thus the Q) increases as the beam increases in either width or thickness, and that the V_m correspondingly increases. In addition, we observe that for all beam widths, such a trade-off is maintained as the thickness of the beam is increased. However, we see that the Q of the cavity mode saturates as the width of the beam is increased beyond $w > 2.4a$, as confinement of the mode in the y -direction is no longer dominant in the overall confinement of the mode. Indeed, the thicknesses (d) of the beams are far smaller than the width at

$w = 2.4a$, and increasing d further increases confinement. Likewise, the k -space profile could remain largely unchanged by the increase of the beam width, thus limiting the Q achieved by this air hole design. In order to maximize the Purcell enhancement for this cavity, we would maximize the Q/V_m ratio, which (in this parameter space), is achieved at $w = 1.6a$ and $d = 1.1a$, corresponding to radiation limited $Q = 25,000$ and $V_m = 1.1(\lambda/n)^3$. This represents an order of magnitude increase in Q and 7 times reduction in mode volume compared to μ -disks with a similar thickness and a diameter of 5 μm [72].

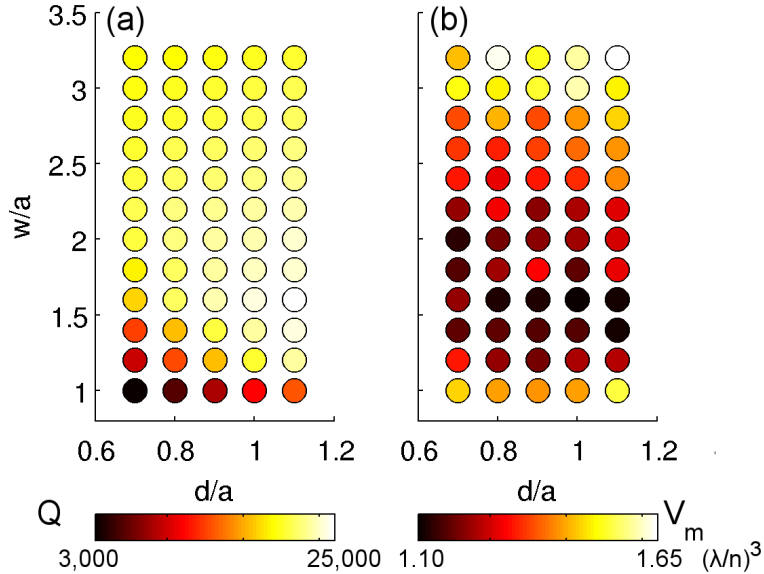


Figure 2.4: (a) Q and (b) V_m for the TE_0 mode for different beam widths (w) and thicknesses (d) for nanobeam cavities in $n = 1.7$ material. We keep the same air hole design for the simulated cavities.

2.1.3 Nanobeam Cavity in Silicon Nitride

We also apply the parabolic design to the Er:SiN_x material, which has an index of refraction approximately the same as that of SiN_x ($n = 2.05$). The hole spacing at the center of the cavity is $0.88a$, and the beam has thickness $d = 0.8a$ and width $w = 1.5a$. The width of the rectangular holes in the direction along the beam is $h_x = 0.5a$, and the width perpendicular to the beam is $h_y = 0.7w$ [Figure 2.5(b)]. We employ the

3D-FDTD method to calculate the field profile of the fundamental TE-like mode, as shown in Fig. 2.5(b). The mode has theoretical normalized frequency $a/\lambda = 0.36$, quality factor $Q = 30,000$, with mode volume $V_m = 0.95(\lambda/n)^3$. In addition, the mode overlap, defined as the fraction of the electric field energy in the beam material, is 52%.

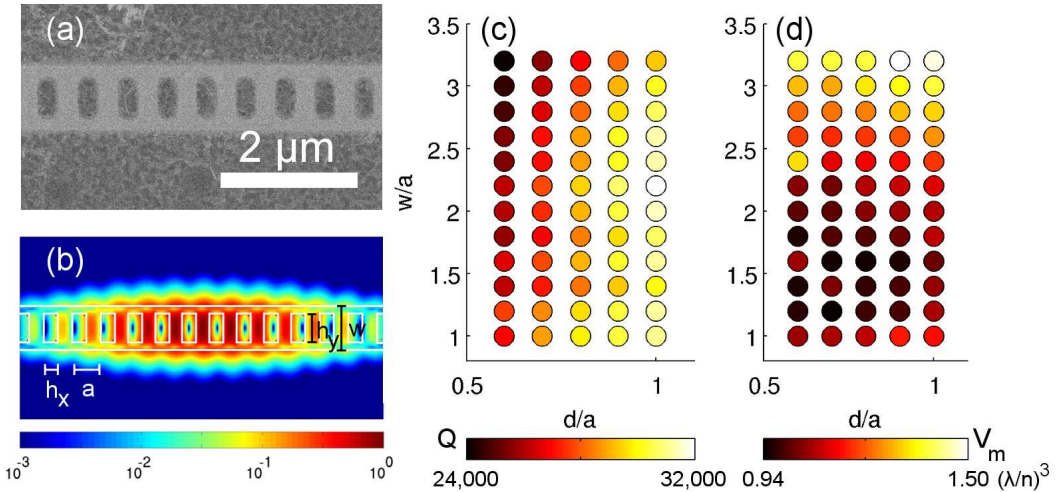


Figure 2.5: (a) SEM image of the fabricated Er:SiN_x nanobeam cavity. (b) The $|E|^2$ profile of the fundamental cavity mode from FDTD simulations. (c)-(d) The color of each marker illustrates the Q and V_m of nanobeam cavities in $n = 2.1$ material as the width and height of the beam is changed, while $h_x = 0.5a$, $h_y = 0.7w$, and the design of the holes are fixed. The reference markers represent $Q = 30,000$ and $V_m = 0.95(\lambda/n)^3$.

We also vary the beam width (w) between $1.0a$ and $3.2a$ and the beam thickness (d) between $0.6a$ and $1.0a$, fixing $h_x = 0.5a$, $h_y = 0.7w$, and the same design of holes for the cavity, and find Q and V_m for the cavities. We observe that the Q of the cavity has little dependence on the width of the beam, but does increase with the beam thickness [Fig. 2.5(c)]. Because SiN_x has a fairly high index of refraction, and beam widths in the studied range can still support waveguide modes, the beam width no longer impacts the Q factor. In addition, we find that V_m is minimized around $w/a = 1.6$ for various beam thicknesses [Fig. 2.5(d)] to about $(\lambda/n)^3$.

2.1.4 High-index Nanobeam Cavities

Although high- Q cavities have already been achieved using 2D PCs for high index materials ($n > 3.0$), the nanobeam design can still be extended to all materials. Here, we consider similar designs for materials like Si and GaAs in the infrared ($n \approx 3.5$). We employ circular holes that are patterned along the beam with period a and radii $r = 0.3a$ (Fig. 2.6(a)). We note that as the index of the beam material is increased, confinement by TIR is enhanced and narrower beam widths can be used in the design without degradation in Q . In addition, for narrow beam widths, circular holes are slightly easier to fabricate, and are used in the design shown in Fig. 2.6(b). This cavity comprises of holes spaced at $a' = 0.84a$ at the center of the cavity, and holes size of $r' = 0.84r$, where a and r are the lattice constant and the hole radius at the outer portion of the cavity. The hole spacing and size increase parabolically from the center of the cavity outwards, extending 6 holes on either side of the cavity. The cavity is designed with $d = 0.7a$ and $w = 1.3a$, and is simulated by the 3D-FDTD method with 20 units per lattice constant and perfectly matched layer (PML) absorbing boundary conditions. We compute the Q of the cavity using time-averaged energy radiated from the cavity. Using the FDTD simulation, we find the $|E|^2$ field profile of the fundamental TE-like cavity mode shown in Fig 2.6(b), which is dominated by the E_y component. We also find that further increase in the number of photonic crystal mirror layers beyond 15 did not increase the overall Q of the cavity. Finally, from the simulations with optimized designs, we obtain $Q = 1.2 \times 10^5$, $V_m = 0.8(\lambda/n)^3$, and normalized frequency of $a/\lambda = 0.25$.

An alternative design for high index nanobeam cavities has been suggested by Quan et. al. [76], where the lattice constant of the air holes is fixed to enhance k -vector matching between segments with different hole sizes. The air holes have maximum radii at the center of the cavity, and the radius is reduced as the distance from the center of the cavity increases. Such a taper-out design follows the same concept of the band diagram in Fig. 2.1(c), where the defect band forming the cavity mode is pushed to higher frequency by the larger air holes at the center of the cavity. Such a design in principle adiabatically joins waveguide mode at the outer edge of the beam to the cavity mode in the center of the beam, enabling high coupling efficiencies

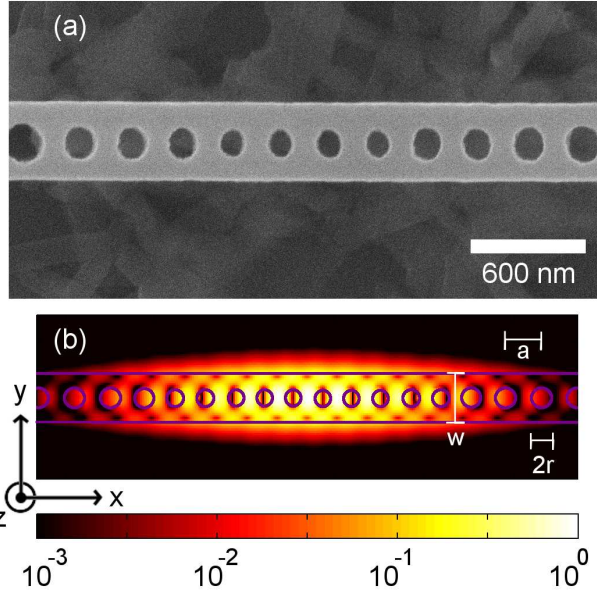


Figure 2.6: (a) The fabricated 1D nanobeam cavity in GaAs, with index $n = 3.5$. (b) The electric field intensity ($|E|^2$) of the fundamental mode supported by the cavity.

when inputting light from the side through the waveguide.

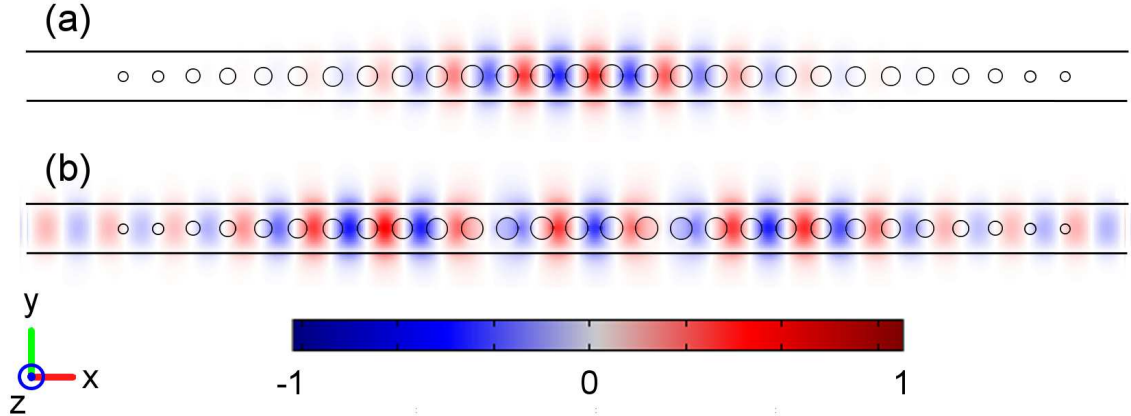


Figure 2.7: (a) The E_y profile for the (a) first and (b) second order modes using the taperout design.

We simulate in 3D-FDTD (with $a = 32$ units) such a cavity design with an index $n = 3.5$ material, with $w = 1.3a$, $h = 0.3a$, the central hole having radius $r = 0.3a$, and the hole area tapering out in a parabolic manner. As with the taper-in type

designs for the low-index material, we observe the first two orders of cavity modes [Fig. 2.7(a)-(b)], although the second order mode is more delocalized in this design. Again, because of the high-index contrast between the beam and the surrounding air, very high Q is achievable in simulation. In this case, $Q_{PC} = 9.0 \times 10^5$ and $Q_\perp = 1.0 \times 10^6$ for the fundamental mode, with $Q_{\parallel} = 5.8 \times 10^6$ [resulting in $Q_{tot} = (Q_{PC}^{-1} + Q_{\parallel}^{-1} + Q_\perp^{-1})^{-1} = 4.4 \times 10^5$]. Thus, we can approximate that the coupling efficiency via the waveguide direction as $Q_{tot}/Q_{PC} \approx 0.48$. The second order mode has $Q = 2,500$, and the mode volumes of the first and second order modes are $0.57(\lambda/n)^3$ and $1.0(\lambda/n)^3$, respectively. This cavity is used as the example to describe the FDTD method in Appendix B.

2.2 Plasmonic Cavity

2.2.1 Metallic Distributed Bragg Reflection Cavity

Similar to the 1D PC cavity, where DBRs confine a mode in the central cavity defect mostly in one direction, we also attempt to design cavities with DBRs for SPP modes by inserting periodic metallic scatters along a flat metal-dielectric interface. The SPP mode offers natural confinement in the direction normal to the metal-dielectric interface, similar to TIR, and DBR could be sufficient to confine SPP modes laterally. Several authors have demonstrated decreased transmission by using periodic structures to manipulate SPPs [77, 78]. These experiments confirm the existence of backscattering and a plasmonic band gap in metallic gratings. In addition, other groups have demonstrated that surface plasmons interfere as normal waves and set up standing waves under certain conditions [79]. Using designs such as the 1D PC cavities for photonic modes, we attempt to design a SPP cavity whose central defect is flanked by DBRs. While some plasmonic DBR cavities have been proposed in previous work [80], the designs are often impractical to fabricate.

The proposed structure is shown in Fig. 2.8 and is composed of gratings with thin slices of metals on either side of an uninterrupted surface, which forms the cavity. Such a grating will open a plasmonic band gap at a frequency to be determined by

the grating period (a). The periodicity of the grating that opens a plasmonic band gap at frequency ω may be determined from the dispersion relationship of SPPs at a metal-dielectric interface:

$$k_{sp} = \frac{\pi}{a} = \frac{\omega}{c} \sqrt{\frac{\epsilon_d \epsilon_m}{\epsilon_d + \epsilon_m}} \quad (2.1)$$

In this section, we assume that the dielectric is GaAs, with permittivity $\epsilon_d = \epsilon_{GaAs} = 12.96$, and the metal is silver, with permittivity estimated from the Drude model as $\epsilon_m = \epsilon_\infty - (\frac{\omega_p}{\omega})^2$, with $\epsilon_\infty = 1$ and the plasmon energy of silver as $\hbar\omega_p = 8.8$ eV ($\lambda_p = 140$ nm) [29]. Setting an operation energy of $\hbar\omega = 1.2$ eV, we determined the grating periodicity to be $a = 116$ nm. Although the metal is only 30 nm thick, coupled modes between the air-metal interface and GaAs-metal interfaces have a negligible impact on the dispersion relation.

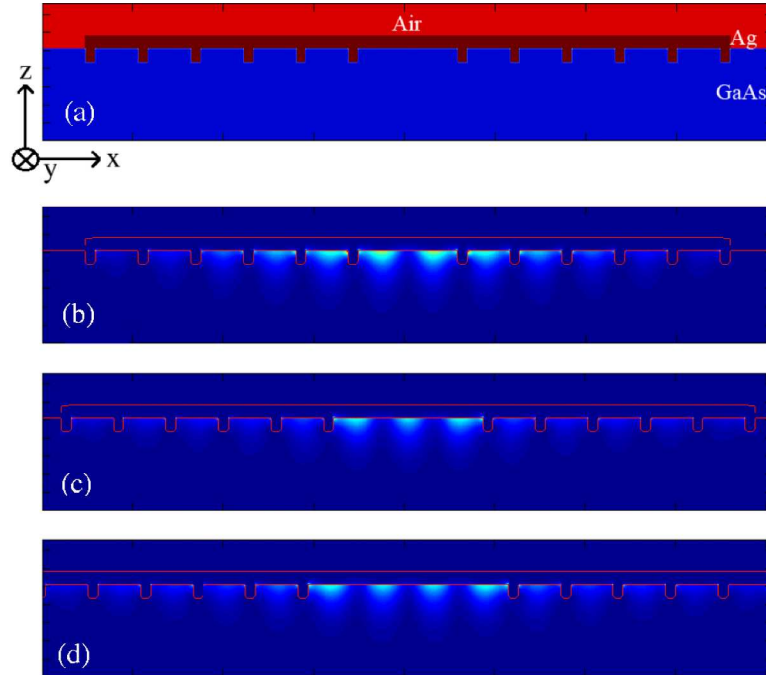


Figure 2.8: (a) The proposed structure. (b)-(d) Mode profiles ($|E|^2$) with total cavity lengths 216 nm, 328 nm, and 440 nm, respectively. These correspond to 2, 3, and 4 peaks of the electric field intensity inside the cavity.

2D FDTD simulations with discretization of 1 unit cell per 2 nm were conducted

with 5 periods of the DBR gratings on either side of a cavity and using the Drude model for the metal [29]. The depth of grooves in GaAs (filled with metal) and the metal slab layer thickness were both set at 30 nm while the groove width was set at 20 nm. Here, losses were also included in the Drude model with the damping energy of $\hbar\eta = 2.5 \times 10^{-5}$ eV to simulate low temperature conditions relevant for solid-state cavity QED experiments [81] (see Appendix B). This damping factor is equivalent to decreasing the non-radiative losses by approximately a factor of 2000 from their room temperature values ($\eta = \eta_{RT}/\xi$), where ξ will be called the loss factor. Such an assumption is for the ideal case of metals, but in experiment are determined by the metal deposition conditions and metal film quality. The cavity length was then varied over multiple grating periods to determine its effect on the modes. Three prospective modes with their electric field intensities are shown in Fig. 2.8 and the influence of cavity length on the Q -factor and frequency is shown in Fig. 2.9. The Q -factors were calculated using the average power radiated from the cavity or lost via absorption in the metal. First, we see that indeed the modes display standing wave patterns inside the cavities. Moreover, the peak quality factors of the modes are separated by grating periods, again supporting the idea that a standing wave is formed by the reflectors on either side of the cavity. The peak quality factor is approximately 1000, and losses are dominated by radiation through the dielectric. The peaks of the quality factor all occur around $\omega = 0.153\omega_p$, suggesting a band gap around that frequency. It is also noteworthy that the radiation parallel to the metal-dielectric interface is not the dominant pathway for losses, suggesting that increasing the number of DBRs would not enhance the overall Q of the modes. Finally, we see that the plasmonic modes of the DBR cavity exhibits a donor tendency, as the modes decrease in frequency as the cavity length increases.

Shown in Fig. 2.10(a) is the calculated Purcell enhancement of a quantum emitter (such as an InAs/GaAs quantum dot - QD) per cavity width Y (in μm) in the y direction normal to the plane of the 2D simulation (see Fig. 2.8). The Purcell enhancement, assuming negligible spectral detuning and non-radiative emitter decay (Γ_{nr}), and alignment of the emitter dipole with the cavity field polarization (mainly

in the z direction) is:

$$\begin{aligned} F &= \frac{\Gamma_0 + \Gamma_{nr} + \Gamma_{pl}}{\Gamma_0 + \Gamma_{nr}} \approx 1 + \frac{\Gamma_{pl}}{\Gamma_0} \\ &= 1 + \frac{3}{4\pi^2} \frac{\lambda^3}{n^3} \frac{Q}{V_m} \left| \frac{E}{E_{max}} \right|^2 \end{aligned} \quad (2.2)$$

where Γ_0 is the emitter spontaneous emission rate in bulk, Γ_{pl} is the emission rate of the QD coupled to the plasmon cavity mode, Q is the quality factor, and V_m is the mode volume defined for 2D simulations as:

$$V_m = \frac{\iint \epsilon_E(x, z) |E(x, z)|^2 dx dz}{\max [\epsilon_E(x, z) |E(x, z)|^2]} Y \quad (2.3)$$

Here, Y is the width of the cavity and the effective dielectric constant is [82]:

$$\epsilon_E(x, z) = \frac{d(\omega \epsilon(x, z))}{d\omega} = \begin{cases} \epsilon_\infty + \left(\frac{\omega_p}{\omega} \right)^2, & \text{metal} \\ \epsilon_{Air} \text{ or } \epsilon_{GaAs}, & \text{non-metal} \end{cases} \quad (2.4)$$

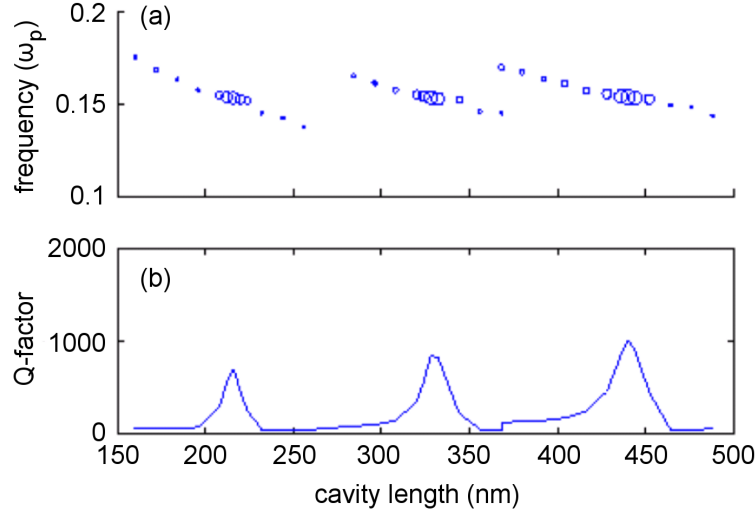


Figure 2.9: Dependence of (a) frequency and (b) quality factor (Q) of the localized plasmon mode on the cavity length. In (a), the dots sizes are proportional to the mode Q -factor.

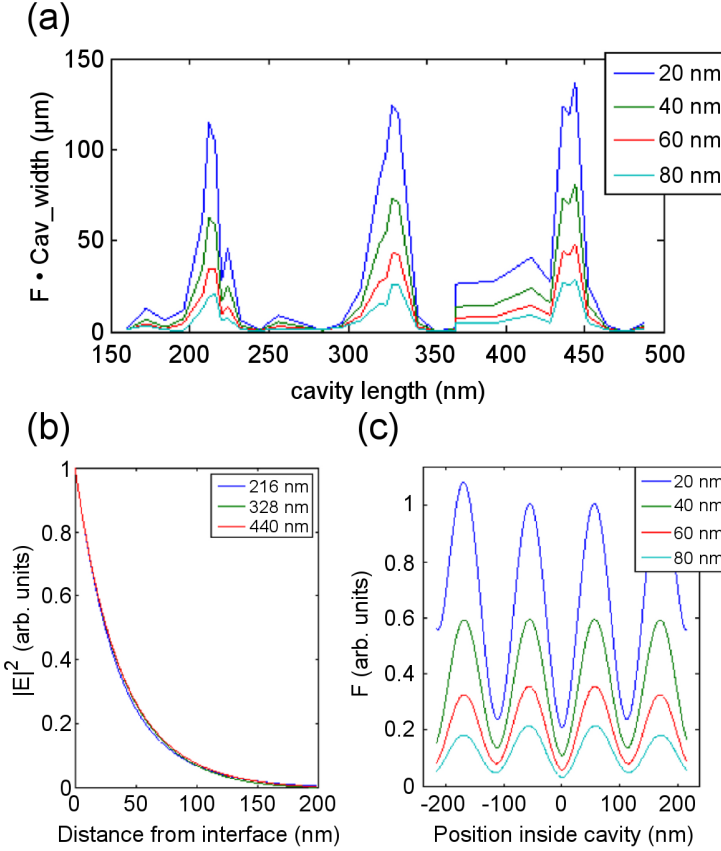


Figure 2.10: (a) Dependence of Purcell enhancement (normalized by width of the cavity in the y direction of Fig. 2.8) on cavity length for various emitter positions relative to the metal-dielectric interface (z direction). (b) Exponential decay of the electric field in the dielectric ($|E|^2$) away from the metal-dielectric interface, plotted for 3 different cavity lengths corresponding to maximum Purcell enhancements. The decay constant of 36 nm is consistent with the plasmon modes in the band gap at the $k_{sp} = \pi/a$ point. (c) Normalized Purcell enhancement as a function of emitter position (in the x -direction) inside the 440 nm cavity for four different emitter distances from the metal-dielectric interface.

The curves pictured in Fig. 2.10(c) show the $|E|^2$ ($\propto F$) for various depths of a quantum emitter relative to the metal-dielectric interface. The larger of the cavities seem to have large tolerances of cavity lengths that could lead to the high Purcell factors. Shown in part (b) of the figure, the electric field amplitude decays exponentially away from the metal-dielectric interface, as expected for SP modes.

Moreover, the decay profile of all three modes is very similar, and the decay constants of $|E|^2$ of 36nm is consistent with the plasmon mode at the $k_{sp} = \pi/a$ point. This again shows that a plasmon frequency is selectively contained by the band gap created from the gratings. Such a decay also creates a mode area of approximately $(50\text{ nm})^2$ for 2D simulations, much smaller than the $(\lambda/n)^2$ area achieved for photonic crystal cavities. If we were able to contain the field in the y direction to 50 nm as well, we could in theory achieve the strong coupling regime. Namely, for an InAs/GaAs quantum dot with a dipole moment of $\mu = 10^{-28}\text{ C}\cdot\text{m}$ [83] positioned 20 nm from the metal-dielectric interface in the tail of E -field anti-node and resonant with the field, the emitter-cavity field coupling is:

$$g = \mu_s \sqrt{\frac{\omega}{2\epsilon\hbar V_m}} \left| \frac{E}{E_{max}} \right| = 2\pi \times 170\text{GHz} \quad (2.5)$$

Note that because E_{max} is not located in the middle of the cavity, but at corners of the cavities, the coupling factor is degraded from maximum values. For comparison, γ (the emitter decay rate without a cavity, dominated by radiative decay, Γ_0) and $\kappa = \omega/(2Q)$ (the cavity field decay rate) are $2\pi \times 1\text{ GHz}$ and $2\pi \times 160\text{ GHz}$, respectively. For such a set of parameters, $g > \gamma, \kappa$, and the onset of the strong coupling regime is reached. While degradation of Q may result from fabrication imperfections, even a ten-fold drop in Q may still result in Purcell enhancements of hundreds, enabling such a device to be used in quantum information applications [84].

Another interesting property of the cavity is the spatial range for high Purcell effect. As shown in Fig. 2.10(c), the electrical field amplitude follows a standing wave profile of an even mode in the x direction and exponentially decays in the z direction. While the E_z field dominates for this mode, the contribution of the E_x field increases as we approach the surface, making the electric field amplitude near the surface significant throughout the cavity. Although the E_z field is the main component of the SPP mode far away from the metal-dielectric interface, quantum dots with polarization in the xy -plane positioned close to the interface could also have high coupling to the SPP mode.

In plasmonics, one great concern is the losses of the metal at optical frequencies.

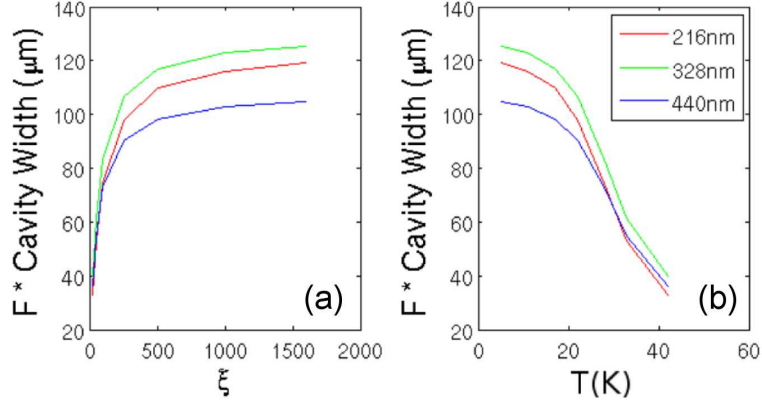


Figure 2.11: (a) Dependence of Purcell enhancement on the loss factor, ξ , in the Drude model (ξ is inversely proportional to the damping frequency). The Purcell enhancements are calculated for emitters 20 nm from the metal-dielectric interface for three different cavity lengths. (b) Dependence of the Purcell enhancement on the temperature, which is obtained by translating the ξ factor into temperatures for a residual resistivity of 1600 for silver.

However, after locating the modes with peak Purcell factors, we can increase losses by a factor of 80 and still preserve enhancement, as shown in Fig. 2.11. Only at those lowest gains in conductivity do the radiative quality factor (Q_{rad}) and mode volume change (by 1% at $\xi = 25$). In the same manner, the Purcell enhancement change is dominated by the linear decrease in the absorptive Q factor (Q_{abs}) with loss, and only drops by a factor of 2 from the low loss ($\xi = 2000$) case at $\xi = 50$. This is seen if the total Q of the system is described as the parallel combination of Q_{rad} and Q_{abs} :

$$\frac{1}{Q} = \frac{1}{Q_{rad}} + \frac{1}{Q_{abs}} \quad (2.6)$$

For loss factors greater than 100, Q_{abs} is far greater than Q_{rad} , and thus is negligible, and the mode is not significantly perturbed. However for loss factors less than 25, the mode is changed, resulting in a diminished Q and negligible Purcell enhancement. This suggests that the sample temperature should be reduced to at least 40 K (where $\xi \approx 25$ [85]) in order for the radiative losses to be dominant. Such operational temperatures are already being used for solid-state cavity QED experiments [57].

2.2.2 Metallic Grating Modes with Silicon Oxide

In this subsection, we study the interaction of plasmonic modes supported by a metallic grating to enhance extraction and emission from silicon-based emitters, such as SRO and SiN_x . Unlike the cavity design of the previous section, we use wide area gratings to enhance emission for a large set of emitters, thereby obtaining large average enhancement of emission instead of enhancing emission from a particular cavity region. Much like the photonic modes at the band edge, we would expect that the SPP dispersion relation flattens at the irreducible zone edge, leading to slow group velocity modes that enhance emission.

We first study the enhancement of Si-NCs using a metallic grating on top of an SRO layer. We analyze the plasmonic modes of a structure with a 70 nm layer of SRO ($n = 1.7$) on top of a quartz substrate, with 30 nm thick gold gratings on top of the SRO layer [Fig 2.12(b)]. We simulate the structure in 2D-FDTD simulations as in the previous section [29, 86], with the plasma frequency of gold as $\omega_p = 2\pi c/(160 \times 10^{-9} \text{ m})$. We calculate the band edge frequencies of the modes at the Γ ($k = 0$) and X ($k = \pi/a$) points of the band diagram, fixing a duty cycle [the ratio between the gold bar width and the grating period, as in Fig. 2.13(b)] of 0.7 and varying the grating period from 200-1000 nm. We plot the free space mode wavelengths (λ_0) for first three relevant modes in the wavelength range of emission from Si-NCs in Fig. 2.12(a), with the first order mode fitting one half SPP wavelength per grating period (corresponding to $k = \pi/a$, i.e. the X point of the band diagram), the second order mode fitting a full SPP wavelength per grating period ($k = 2\pi/a$, which folds to the Γ point), and so forth. We also calculate the field profiles for the first three order modes for a duty cycle of 0.8, fixing the free-space wavelength $\lambda_0 \approx 800 \text{ nm}$, and plotting the results in Fig. 2.12(b)-(d). The grating period (a_p) for the p^{th} order mode with a given mode frequency ω can be roughly determined from the SPP dispersion relationship at the Si-NCs-gold interface without a grating [20]:

$$\frac{p\pi}{a_p} = k_g = \frac{\omega}{c} \sqrt{\frac{\epsilon_d \epsilon_m(\omega)}{\epsilon_d + \epsilon_m(\omega)}} \quad (2.7)$$

where $\epsilon_d = n_{NC}^2$ is the dielectric constant of the Si-NC layer, the dielectric constant of gold is $\epsilon_m(\omega) = 1 - (\omega_p/\omega)^2$.

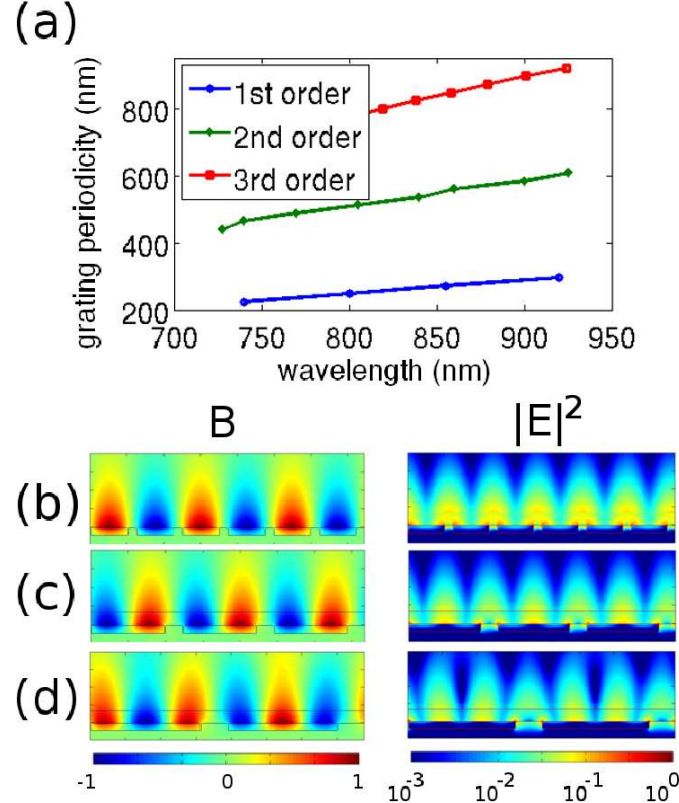


Figure 2.12: (a) The FDTD calculated band edge frequencies for first, second, and third order modes of the SPP band diagram. The first and third order modes correspond to modes at the X ($k = \pi/a$) point of the dispersion relation, while the second order mode corresponds to modes at the Γ ($k = 0$) point. The $|E|^2$ and $|B|^2$ fields for the first (b), second (c), and third (d) order modes are plotted.

We calculate the Purcell enhancement by discretizing the dispersion relation by following the procedure from reference [87]. The Purcell enhancement for each k -vector is given by:

$$F(\nu, k) = \frac{3}{2} \frac{c^3}{n_{NC}^3 \omega^2(k)} \frac{\max[\epsilon_E(z)|E(z)|^2]}{\int \epsilon_E(z)|E(z)|^2 dz} \left(\frac{E}{E_{max}} \right)^2 S(\nu, Q_k), \quad (2.8)$$

where the normalized density of states $S(\nu)$ is from Eqn. 1.4, Q_k is the quality

factor corresponding to the mode at the (ω, k) point of the band diagram, $\omega(k)$ is the dispersion relation for the grating structure, and $\epsilon_E(x, z) = d(\omega\epsilon(x, z))/d\omega$ is the effective dielectric constant. We then sum over all k -vectors to calculate the Purcell enhancement as a function of the frequency ν . This enhancement is averaged over the region occupied by the Si-NCs. By obtaining $\omega(k)$ from the dispersion relation, we calculate the Purcell enhancement for the first, second, and third order modes as 3.8, 3.3, and 3.1, respectively.

Another way to calculate the Purcell enhancement is as follows. We make the intuitive approximation that the standing wave modes in Fig. 2.12(b)-(d) are modes of cavities spaced with the period of the SPP half wavelength, as those modes have the same frequency ω . We then calculate radiative quality factor (Q_{rad}) and the mode volume, defined as:

$$V_{quant} = \frac{\iint \epsilon_E(x, z)|E(x, z)|^2 dx dz}{\max [\epsilon_E(x, z)|E(x, z)|^2]} Y, \quad (2.9)$$

the integral is taken over the unit cell of the SPP wave [88], and Y is the length of the grating bars. Using the above figures, and noting that the quality factor is limited by the absorption factor $Q_{abs} \approx 50$ (since $Q_{rad} \approx 500 \gg Q_{abs}$), we can calculate the average Purcell enhancement by using Eqn. 1.2, where the E -field intensity is again averaged over the region occupied by the Si-NCs. With $Y = 10 \mu\text{m}$ as in the fabricated devices, we estimate the average Purcell enhancements to be 2.7, 2.7, and 2.4 for respectively, the first, second, and third order modes, which approximates the results from the previous method.

2.2.3 Metallic Grating Modes in Metal-Insulator-Metal Configuration with Silicon Nitride

Finally, we analyze metal-insulator-metal (MIM) structures, where the active material is sandwiched between two metallic layers, and grating modes are formed by patterning the metal on one side. In order to increase the emitter-field coupling from the case where the SPP mode is on only one side of the active material, we propose to employ a MIM device. MIM devices with active materials have been considered using III-V materials sandwiched by metal layers, using liftoff processes to preserve

the crystalline material [29]. Passive MIM waveguides with sputtered oxide as a passive insulator have been previously demonstrated, with extreme sub-wavelength dimensions [89], and coupling of emitters to MIM modes have also been theoretically considered [90]. It is possible that silicon compatible materials can be directly deposited on metal while maintaining their luminescence, thus avoiding complicated fabrication processes. In this section, we analyze an active SiN_x layer sandwiched between a metal substrate and a metallic grating, as nitrides are robust and can be directly deposited on metal. In addition, nitrides can be hosts to Er ions with emit at $1.5 \mu\text{m}$, where metallic losses are reduced compared to operation in the visible wavelengths.

The dispersion relation of the MIM mode with semi-infinite metal thicknesses, insulator thickness t , and field symmetric along the direction perpendicular to the insulator layer, is given by the transcendental equation [91]:

$$-\frac{k_m}{k_d} = \frac{\epsilon_m(\omega)}{\epsilon_d} \tanh(k_d t/2), \quad (2.10)$$

where $k_m = \sqrt{k^2 - \epsilon_m(\omega)(\omega/c)^2}$ and $k_d = \sqrt{k^2 - \epsilon_d(\omega/c)^2}$ are defined in terms of the SPP propagation k -vector, and t is the thickness of the insulator layer. Because the two metal surfaces confine the SPP mode from both sides of the active material, the mode volume of the MIM mode is decreased relative to that of the SPP mode supported by metal on only one side of the insulator. In addition, the symmetric field mode of a MIM structure has higher overlap with the active material than the mode of a single sided design.

We analyze the MIM grating structure using the 2D-FDTD method with parameters in our previous work [86, 92]. The structure has a 100 nm gold substrate, with plasma frequency $\omega_p = 2\pi c/(160 \times 10^{-9} \text{ m})$, a 52 nm Er: SiN_x layer with index of refraction $n = 2.1$, and a 30 nm thick top gold grating [Fig. 2.13(b)]. In particular, we fix the grating duty cycle to be $d = 0.8$, and vary the grating period. We find the wavelengths of the band edge SPP modes as a function of grating period, as plotted in Fig. 2.13(a). We focus on the SPP MIM mode that has symmetric field (and anti-symmetric charge) along the growth direction [up-down in Fig. 2.13(b)-(c)], as

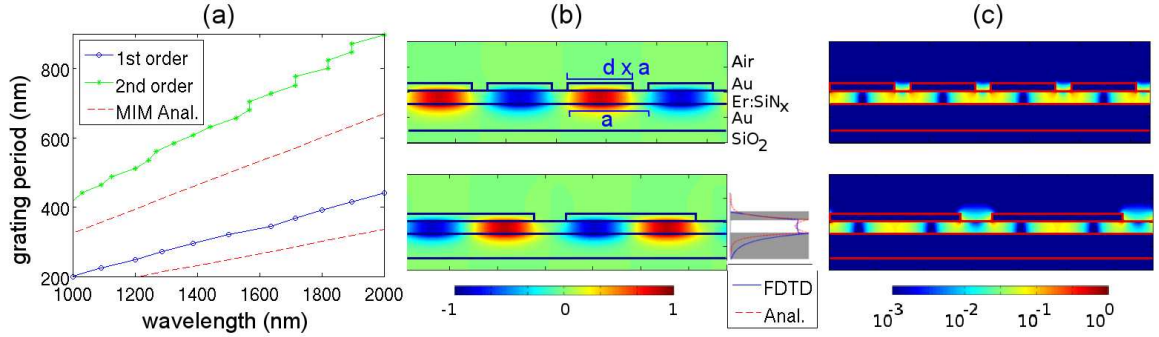


Figure 2.13: (a) The wavelengths of the first and second order field-symmetric MIM SPP modes for different grating periods, with a 52 nm thick layer of SiN_x between the metal layers. The analytical solution for a MIM structure with semi-infinite metal thickness and the same SiN_x thickness is also shown. (b) The magnetic field (B) and (c) the electric field intensity ($|E|^2$) of the first (top) and second (bottom) order modes near free space $\lambda_0 \approx 1500$ nm. The MIM SPP modes in a 2D simulation have B fields perpendicular to plane of the figures, while the E field is restricted to the plane of the figures. The inset of (b) shows the magnetic field through a vertical slice of the structure, as well as the analytical solution of a MIM system with semi-infinite metal thicknesses and a 52 nm SiN_x spacer layer.

it will have high overlap with the active material. In addition, we focus only on the band edge modes in the plasmonic band diagram that support integer multiples of the SPP half-wavelengths within the grating period and exhibit the strongest emission enhancement, as in Eqn. 2.7 [92]. Because the Er emission wavelength is much longer than the plasma wavelength of gold, the structures operate in the “linear” regime of the SPP dispersion relation, where the band edge modes’ wavelengths are approximately linear with respect to the grating period. We examine the magnetic field (B) and electrical field intensity ($|E|^2$) of the first and second order modes, where the first order mode [Fig. 2.13(b)-(c), top] is at the X -point of the dispersion relation, while the second order mode [Fig. 2.13(b)-(c), bottom] is at the Γ point. The solution of Eqn. 2.10 for the MIM mode with semi-infinite metal thicknesses and the same SiN_x parameters is also plotted in Fig. 2.13(a) for the same periodicities, and the analytical magnetic field profile of such a MIM mode is shown in the inset of Fig. 2.13(b). The dispersion relation of the grating is blue shifted from the analytical model of Eqn. 2.10, as the MIM modes for the grating are no longer fully confined and slightly

overlaps with air. By comparing the simulations with a similar one-sided SPP mode with a fully SiN_x substrate to this MIM design, we find that the overlap with the active material (in a 52 nm slice near the metallic grating surface) is increased by approximately 0.5, and the mode volume is approximately halved for the MIM SPP mode.

Chapter 3

Enhancement of Photoluminescence and Lasing in One-dimensional Photonic Crystal Cavities

3.1 Silicon Nanocrystals in Oxide

Photoluminescence (PL) from silicon nanocrystals (Si-NCs) in a nitride host was previously coupled to a photonic crystal (PC) cavity [64], and PL from Si-NCs in an oxide host was coupled to a microdisk cavity [72, 93]. In the microdisk case, the loss mechanisms of the material were analyzed, and it was noted that free carrier absorption may play a significant role in loss processes and may ultimately inhibit gain in this material [93]. In addition, loss mechanisms were also studied in ultra-high quality (Q) factor bottle resonators, which have large V_m [94]. By coupling the Si-NCs to an oxide 1D PC (nanobeam) cavity, we examine the emission properties of the material, along with the lossy mechanism, in a small mode volume (V_m) setting, (instead of the larger whispering gallery mode type resonators).

The Si-NC beams with embedded Si-NCs are made by fully CMOS compatible fabrication techniques, following the fabrication procedures in Appendix A.2. Cavities

are fabricated with the design parameters from Sec. 2.1.2, and the final fabricated structure is shown in Fig. 2.3(a). We vary the lattice constant a from 250 nm to 350 nm with a fixed thickness of $d = 200$ nm in fabrication to create cavities with a variety of wavelengths, where all beams have a width of $w = 3.2a$ (due to fabrication constraints). A transmission electron microscope (TEM) image of representative Si-NCs is shown in Fig. 3.1(b).

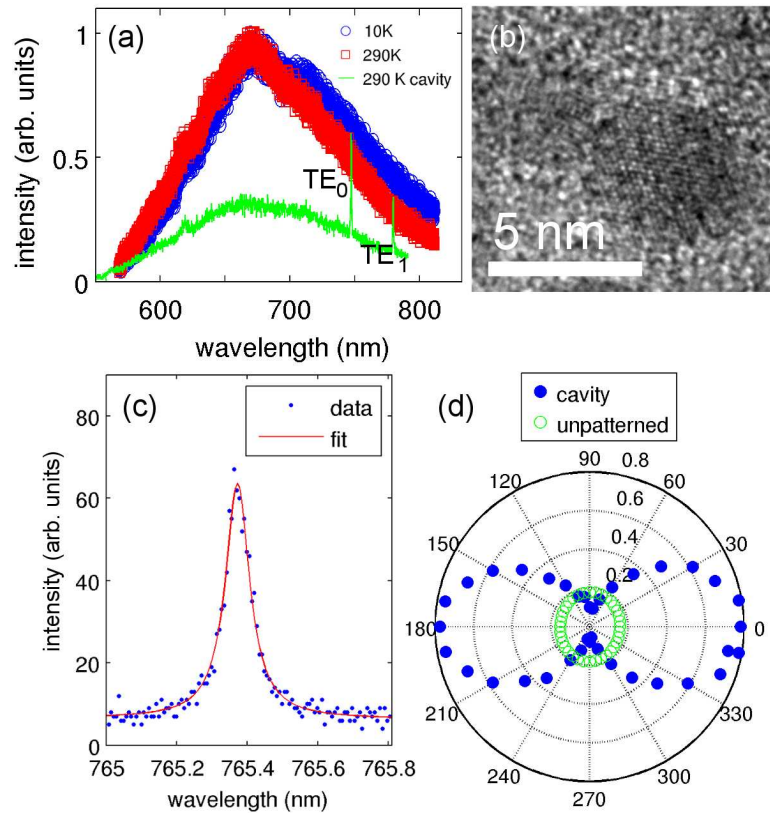


Figure 3.1: (a) PL spectra from unpatterned oxide film with Si-NCs at 10 K and 290 K, as well as a cavity spectrum at 290 K with the first two TE modes visible. (b) TEM image of representative Si-NCs. (c) The PL spectrum of a representative fundamental cavity mode at 290 K, and the fit to a Lorentzian with $Q = 9,000$. (d) The polarization angle dependence of the cavity mode at 290 K, along with the angle dependence of PL from an unpatterned region. 0° corresponds to the y -direction of Fig. 2.3(d).

The micro-photoluminescence (μ -PL) experiments are conducted with a $63\times$ objective lens with numerical aperture $NA = 0.75$, focusing the pump to a $5 \mu\text{m}$ diameter spot (See Appendix C). The sample is pumped from normal incidence [z in Fig. 2.3(b)] with either a CW 405 nm laser diode or a frequency doubled Ti:Sapphire (Ti:Sapph) laser at 390 nm with 3 ps pulses and repetition rate 80 MHz. The photoluminescence is also collected from normal incidence through the same objective and directed to a Si CCD array in a spectrometer, with resolution of 0.01 nm. The cryogenic temperature experiments are conducted in a helium flow cryostat, with temperatures as low as 5 K. Room temperature data was taken outside of vacuum. We observe the PL from an unpatterned region of the sample at both 10 K and 290 K, using the CW laser as the pump [Fig. 3.1(a)]. The PL spectrum is centered at around 670 nm, and is the same at both temperatures, which suggests that the change in the homogeneous linewidth for the Si-NCs is small with temperature. Finally, we observe that the PL of the sample pumped with the pulsed Ti:Sapph laser (not shown) was the same as the PL in Fig. 3.1(a) at both temperatures, similar to previous work [95].

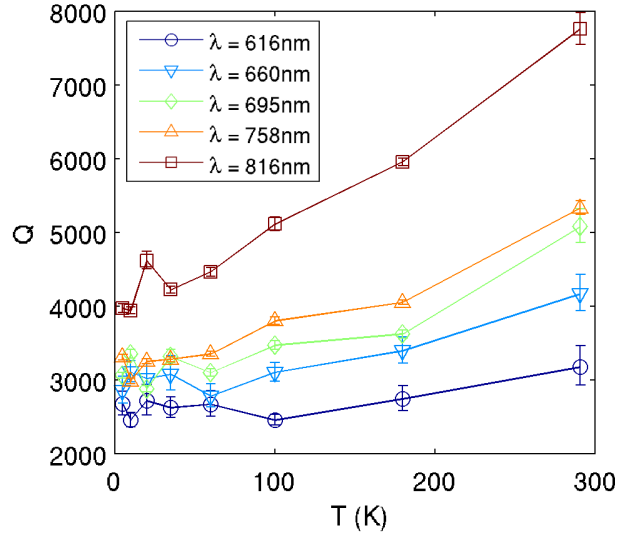


Figure 3.2: The Q s of nanobeam oxide cavities with Si-NCs at different wavelengths as a function of temperature.

We also investigate the cavities in the same μ -PL configuration, first at room

temperature. A representative cavity spectrum at 290 K is shown in Fig. 3.1(a), where at least the first two orders of transverse electric- (TE-) like modes (TE_0 and TE_1) are visible. We also plot the spectrum of the fundamental mode of a high- Q cavity along with a fit to a Lorentzian lineshape, representing $Q = 9,000$, in Fig 3.1(c). Finally, we measure the polarization angle dependence of the cavity mode by placing a polarizer and a half waveplate in the PL collection path, plotted in Fig. 3.1(d). The cavity mode is dominated by the E_y field, and the mode is measured to have a linear polarization in the y -direction. On the other hand, the PL collected from the unpatterned region is unpolarized. As seen from the finite-difference time-domain (FDTD) simulations, the TE_0 mode has the highest Q and lowest V_m . Thus, we choose to work with the fundamental mode to maximize the Purcell effect.

We measure the Q -factors of various cavities throughout the Si-NC PL spectrum at temperatures between room temperature and 5 K, as shown in Fig 3.2. The cavities are all pumped with the CW diode laser and very low pump powers (200 nW), which is necessary to reduce the cavity losses stemming from free carrier absorption (FCA). The different cavities have different lattice constant a , but have the same fixed $w/a = 3.2$ ratio, $d = 200$ nm, and the same air hole design. We find that for all cavities, the cavity Q continuously drops to approximately one half of the room temperature value at 5 K. Such change in cavity Q can be attributed to the difference in the homogeneous linewidth of the Si-NCs at the two temperatures. As seen in previous work on coupling Er emission to PC cavities, the Purcell enhancement of absorption is degraded when the homogeneous linewidth of the emitter far exceeds that of the cavity linewidth [96]. Single Si-NCs have measured linewidths of over 100 nm at room temperature, but have far narrower linewidths down to 1 nm at 35 K [97]. Thus, the narrower linewidth at low temperature increases the absorption of the Si-NCs coupled to the cavity mode, and lowers the Q of the cavities. The temperature dependence of Q suggests that the homogeneous linewidth of the Si-NCs continuously decreases with temperature, much as in previous work [97].

In addition, we study the Q s of many cavities at the extremes of the temperature (10 K and room temperature), where the same set of cavities was measured at both temperatures [Fig. 3.3(a)]. We again notice that the Q s of the cavities are higher

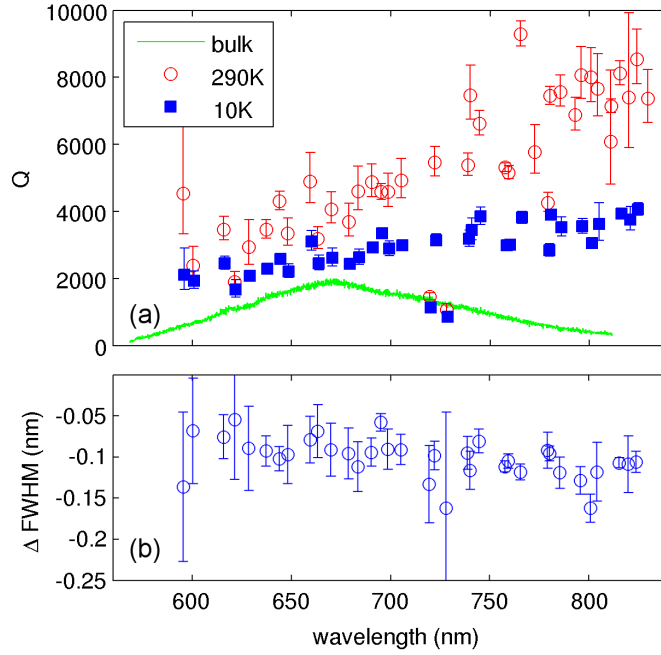


Figure 3.3: (a) The Q s of the one set of cavities vs. the cavity wavelengths, at 10 K and 290 K. The PL from an unpatterned region of the sample is shown for reference. (b) The change in the cavity linewidth as the temperature is increased from 10 K to 290 K. Lower Q s at low temperature are attributed to the increase in Si-NC absorption, resulting from narrowing of the Si-NC linewidth.

at room temperature than the Q s of the same cavities at 10 K. Because the lattice constant increases for the longer wavelength cavities, the d/a ratio decreases with increasing cavity wavelength. We note in Fig. 3.2 and Fig. 3.3(a) that the cavities have increasing Q at longer wavelengths, which disagrees with the simulated trend of higher Q s for thicker beams (higher d/a). While this discrepancy could be caused by higher sensitivity to surface roughness for cavities operating at shorter wavelengths, we do not observe this effect in similar cavities made in pure SiO_2 [69]. Thus, we attribute the decreasing Q with decreasing lattice constant to the material absorption of the Si-NCs, which increases with decreasing wavelength (as more NCs contribute to absorption). We also measure the change in the cavity linewidth for the same set of cavities between 290 K and 10 K, shown in Fig. 3.3(b). We notice that the decrease in the linewidth with increasing temperature is approximately uniform and

equal to 0.10-0.15 nm for the entire wavelength range of the Si-NC PL. The losses in the cavity can be related to the cavity Q by:

$$\frac{\omega}{Q} = \frac{\omega}{Q_0} + \gamma(T, P) \quad (3.1)$$

where ω is the cavity frequency, Q_0 is the intrinsic cavity Q , and $\gamma(T, P)$ is the pump power and temperature dependent loss rate. The intrinsic Q change with temperature is negligible, as a result of the small change in refractive index (the change in cavity wavelength with temperature is negligible). In this case, the measured linewidth difference is the change in $\gamma(T, P)$ with temperature, and suggests that the linewidth narrowing of the Si-NCs is uniform throughout the PL spectrum.

We also use 10 K and 290 K as representative temperatures for measuring the power dependence of the cavities. We employ both the CW diode laser and the pulsed doubled Ti:Sapph laser in the power dependence studies, and we pump various representative cavities throughout the PL wavelength range. By fitting the obtained spectra to Lorentzian lineshapes, we obtain the integrated emission, cavity wavelength, and cavity linewidth. In Fig 3.4(a)-(b), we first investigate the integrated cavity intensity obtained from the fits at 290 K and 10 K, respectively, as a function of pump power. We observe that the cavity output is approximately linear in the pump power, with some slight sub-linear characteristics, mostly likely due to FCA. In addition, we find that at both temperatures, the output for the pulsed pump generates slightly more PL. Finally, at room temperature, the output intensities of the cavities have slightly lower slope for the pulsed pump than for the CW pump. On the other hand, the slopes of the light-in light-out curves are approximately the same for the different types of pump at 10 K. Such sub-linear behavior at small pump powers is similar to the trend from previous work with Si-NCs coupled to μ -disk cavity modes [93]. The smaller increases in the cavity amplitude with increasing pump power for pulsed pumping suggest that lossy mechanisms are more readily found with pulses and high instantaneous pump intensities.

We also find the pump dependence of the change in the cavity wavelength from the fits to a Lorentzian lineshape, and plot the results for the cavities around 720

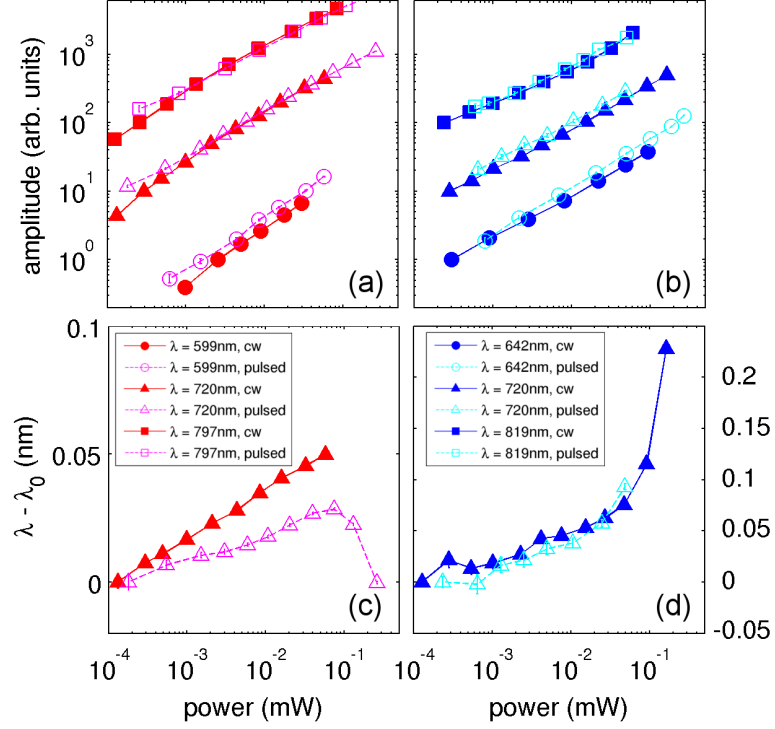


Figure 3.4: The pump power dependence of the integrated intensity for different cavities at (a) 290 K and (b) 10 K. The amplitude traces of each cavity are offset by factors of 10 to allow clear viewing. The pump power dependence of the change in cavity wavelength (with respect to the low pump power wavelength, λ_0) for different cavities at (c) 290 K and (d) 10 K. Power dependences were taken with both the CW diode laser and the pulsed frequency-doubled Ti:Sapph. The pump power is measured in front of the objective.

nm in Fig. 3.4(c)-(d), obtained at 290 K and 10 K, respectively. We observe that in both cases, the cavity continuously red-shifts with increasing pump power, implying the thermal-optic effect as the cause [93]. At room temperature, the pulsed pump generates far less heating than the CW pump, while at 10 K, the wavelength shifts are approximately the same between the two pump methods. In addition, at high pump powers for both CW and pulsed pumping, we observe melting of the cavities, where the wavelength of the cavities abruptly blueshifts [e. g. in Fig. 3.4(c) for the pulsed pumping]. In order to avoid this regime, pump powers are kept below 500 μ W for all experiments. We also note that the wavelength shift for the cavities can be

related to the index of refraction change caused by the thermal-optic effect by (using the perturbation method of Ref. [98]):

$$\Delta\lambda \approx \lambda \frac{\Xi}{2} \frac{\Delta\epsilon}{\epsilon}, \quad (3.2)$$

where Ξ is the fraction of the mode overlapping with the Si-NC doped oxide, λ is the unperturbed cavity wavelength, $\Delta\lambda$ is the change in cavity wavelength, $\Delta\epsilon$ is the change in dielectric constant, and ϵ is the dielectric constant of the Si-NC doped oxide. For the TE_0 cavity mode at 720 nm, we obtain $\Gamma = 0.52$ from FDTD simulations, and find that the index of refraction shift is $\Delta n = 2.2 \times 10^{-4}$, which corresponds to a temperature change of 20 K, using the bulk thermal-optic coefficient of oxide, $dn/dT = 1 \times 10^{-5}/K$. Such a change in index (and temperature) is achieved with approximately two orders of magnitude less power than in the μ -disk setting [93]. This large change is due to the lack of heat conduction from the nanobeam cavities, as noted from previous work with thermal-optical bistability in 1D nanobeam cavities fabricated in silicon [99]. The changes in index with temperature are doubled when pumping the cavities at 10 K, possibly due to reduced air convection inside a vacuum.

Finally, we measure the cavity linewidth for representative cavities throughout the Si-NC PL spectrum, at both 290 K and 10 K in Fig. 3.5(a) and (b), respectively. We note that the cavity linewidth continuously increases with increasing pump power, regardless of cavity wavelength or cavity Q . The linewidth data resembles the linewidth data for μ -disk modes in Ref. [93], though the low pump power Q s for the nanobeam cavities are approximately 4-8 times higher. Such broadening of the cavity linewidth can be attributed to FCA. Taking the pump beam spot area to be $4 \mu m^2$, we find that the power necessary to observe FCA is more than an order of magnitude less than in μ -disks, corresponding to a pump flux of $3 W/cm^2$ [93]. Following the slope of the curves in Fig. 3.5, smaller powers could also generate losses from free carrier absorption. As described previously [93], the onset of FCA only occurs when the FCA dominates other processes such as Mie scattering and band-to-band absorption in nanocrystals. On the other hand, in high Q , low V_m systems, we observe that free-carrier absorption dominates the other processes, and that linewidth broadening

effect from FCA occurs at even small powers. In addition, the linewidth increases until at high pump powers ($> 100\mu\text{W}$), there is a sudden increase due to overheating and melting of the cavities. In previous work, the losses arising from FCA in μ -disks were saturated when the carrier density is sufficiently high to promote Auger recombination [93]. However, we do not reach that regime, as the pump intensities required are higher than that to destroy the cavities. We further note that the cavity linewidth for each cavity is narrower with the CW pump than with the pulsed pump at room temperature. Such evidence corroborates the conclusion that pulsed pumping induces more losses in the cavities than CW pumping.

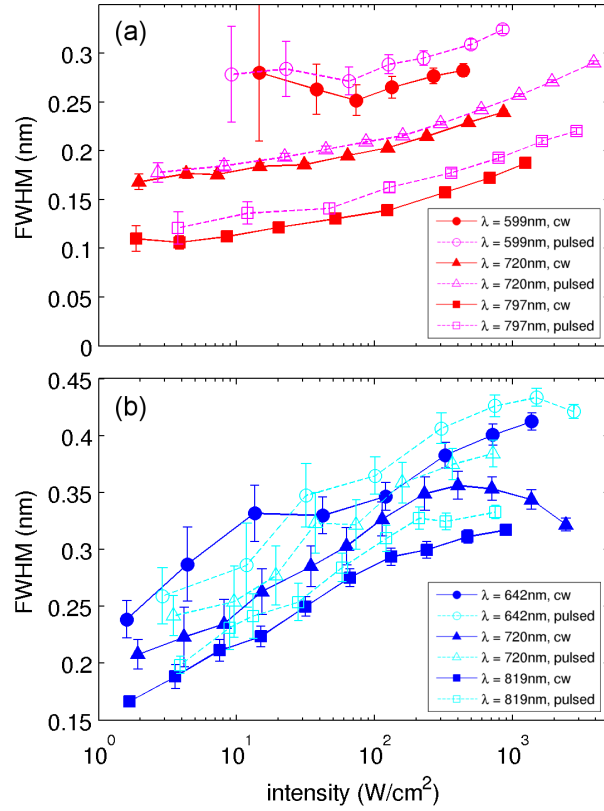


Figure 3.5: The linewidths of representative cavities as the pump power is changed at (a) 290 K and (b) 10 K. Both a CW diode laser and a frequency doubled mode-locked Ti:Sapph laser are used as the pump source. The pump power is measured in front of the objective.

We attempt to characterize the FCA mechanism following the procedure in Ref.

[93]. First, we find the distribution of Si-NC sizes by assuming that the energy of emission for the Si-NCs is related to the size of the NCs by [93, 100]:

$$\hbar\omega = E_{g,Si} + \frac{3.73}{(2R)^{1.39}}, \quad (3.3)$$

where $E_{g,Si} = 1.12$ eV is the bandgap energy of bulk Si, $\hbar\omega$ is the energy of emission in eV, and R is the radius of the NC in nanometers. The emission at each energy is proportional to the density of nanocrystals at a particular size, and the proportionality constant is found by finding the volume ratio of Si in the entire film, assuming complete phase segregation. By finding the mass fractions of Si ($x_{Si} = 0.42$) and O ($x_O = 0.47$) obtained from x-ray photoelectron spectroscopy (XPS), we find that the distribution of nanocrystal sizes ($\rho(R)$) as the distribution shown in Fig. 3.6(a). As expected, the distribution of NCs has smaller radii than the NCs of Ref. [93], as the NC emission has been pushed to shorter wavelengths. By integrating the distribution for all radii, we find a total nanocrystal density of $N_{NC} = 7 \times 10^{18}$ cm⁻³, which is comparable to the densities obtained in other works [36, 93].

We also find the pump power dependent rise (τ_r) and fall (τ_f) times of the Si-NCs, by chopping the CW diode pump with an acousto-optic modulator with 15 ns rise and fall times. Representative time traces from unpatterned regions of the sample can be found in Fig. 3.6(b), for the sample at 290 K and 10 K. Stretched-exponential functions are fitted to the data to find τ_r and τ_f [101]. The τ_f of the sample is found to be approximately 20 μ s at 290 K, and approximately 80 μ s at 10 K [Fig. 3.6(c)]. The longer lifetime at low temperatures is expected, as similar samples of porous silicon also demonstrate a dramatic increase in lifetime with decreasing temperature, which was attributed to longer radiative lifetimes and higher fraction of the emission coming from the diffusion of carriers [101]. It is also possible that non-radiative recombination centers and recombination at dangling bonds are reduced with temperature. The excitation cross section of the Si-NCs at a particular wavelength λ ($\sigma_{ex}(\lambda)$) can be related to τ_r , τ_f , and the pump flux ϕ by [93]:

$$\frac{1}{\tau_r(\lambda)} = \sigma_{ex}(\lambda)\phi + \frac{1}{\tau_f(\lambda)}. \quad (3.4)$$

By conducting time-resolved measurements at various wavelengths, using 10 nm band-pass filters to spectrally filter the emission, we find σ_{ex} by a linear fit of the pump flux dependent difference of $1/\tau_r - 1/\tau_f$ to ϕ , with the results shown in Fig. 3.6(c). Finally, the occupation (the number of electron-hole pairs) of individual Si-NCs at a particular size and pump flux ($f(R, \phi)$) is found by the relation [93]:

$$\frac{\sigma_{ex}(\lambda)\phi}{\hbar\omega_p} - \frac{f(R, \phi)}{\tau_f(\lambda)} - \frac{f^3(R, \phi)}{\tau_A(\lambda)} = 0, \quad (3.5)$$

where ω_p is the pump laser frequency, and τ_A is the Auger recombination time. The Auger time constant can be found by $\tau_A = 1/C_A \times (V/2)^2$, where $C_A = 4 \times 10^{-31}$

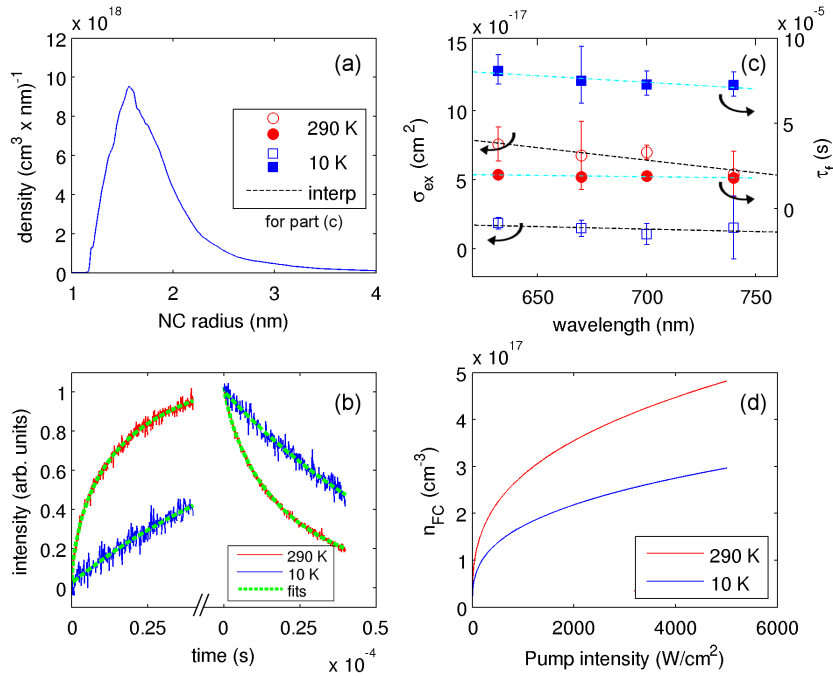


Figure 3.6: (a) The Si-NC density distribution of this sample as a function of Si-NC radius. (b) Time resolved measurements of the Si-NC rise and fall time. Fits to extended exponential distributions yield a rise time of 17 μ s and a fall time of 20 μ s for the sample at 290 K, and a rise time of 78 μ s and a fall time of 79 μ s for the sample at 10 K. (c) The excitation cross section and the lifetimes (τ_f) of the Si-NCs as a function of emission wavelength, for both 290 K and 10 K. (d) The calculated free carrier concentration as a function of pump intensity for 290 K and 10 K.

cm^6/s is the Auger recombination coefficient for bulk Si, and V is the volume of the Si-NC assuming a spherical particle shape [102, 93]. Although the bulk Si Auger coefficient is used, the Auger recombination time of Si-NCs with similar sizes as the ones in this work has been observed to match well with the bulk Auger time constant [102]. Finally, the density of free carriers at a pump flux ϕ ($n_{FC}(\phi)$) can be found by integrating the occupation for NCs of all sizes [93]:

$$n_{FC}(\phi) = \int_R f(R, \phi) \rho(R) dR. \quad (3.6)$$

We plot the results in Fig. 3.6(d), and observe that due to the smaller excitation cross-section at 10 K, the free carrier concentration at 10 K at any particular pump flux is approximately one half that of the free carrier concentration at 290 K.

Finally, this free carrier concentration can be related to the change in linewidth of the cavity modes, assuming the FCA is the dominant absorption process:

$$\Delta\text{FWHM} = \frac{\lambda^2 \Xi}{2\pi n_{eff}} \sigma_{FCA}(\lambda) n_{FC}, \quad (3.7)$$

where ΔFWHM is the change in the cavity linewidth, n_{eff} is the effective index of the cavity mode, and $\sigma_{FCA}(\lambda)$ is the free carrier absorption cross-section. We calculate n_{eff} and Ξ from the FDTD simulations with various beam dimensions. We plot the change in linewidth (obtained from the power dependence curves) against n_{FC} , and find σ_{FCA} through a linear fit to the slope [Fig. 3.7(a), showing data from the cavity near 720 nm] for cavities at both 290 K and 10 K. In addition, we plot all of the fitted σ_{FCA} for different cavities throughout the Si-NC PL spectrum at both temperatures, as a function of the cavity wavelength, in Fig. 3.7(b). We first note that the mean free carrier absorption obtained in the nanobeam cavities is a factor of 4 increased from that obtained in Ref. [93] at room temperature. In addition, as seen in Fig. 3.7(a), the change in the cavity linewidth with increasing pump power is larger at 10 K than at 290 K for the same cavity. Even more, because the free carrier density at the same pump power is lower at 10 K than at 290 K, we calculate that the σ_{FCA} is approximately 6 times higher at 10 K than at 290 K [Fig. 3.7(b)].

While FCA in bulk crystalline materials decreases with temperature [103], the FCA mechanism in Si-NCs of scattering at the Si-NC boundary [93] could be less sensitive to temperature. However, we do not observe the λ^2 dependence of σ_{FCA} generally associated with FCA [93], especially at room temperature, where σ_{FCA} is seen to decrease with wavelength.

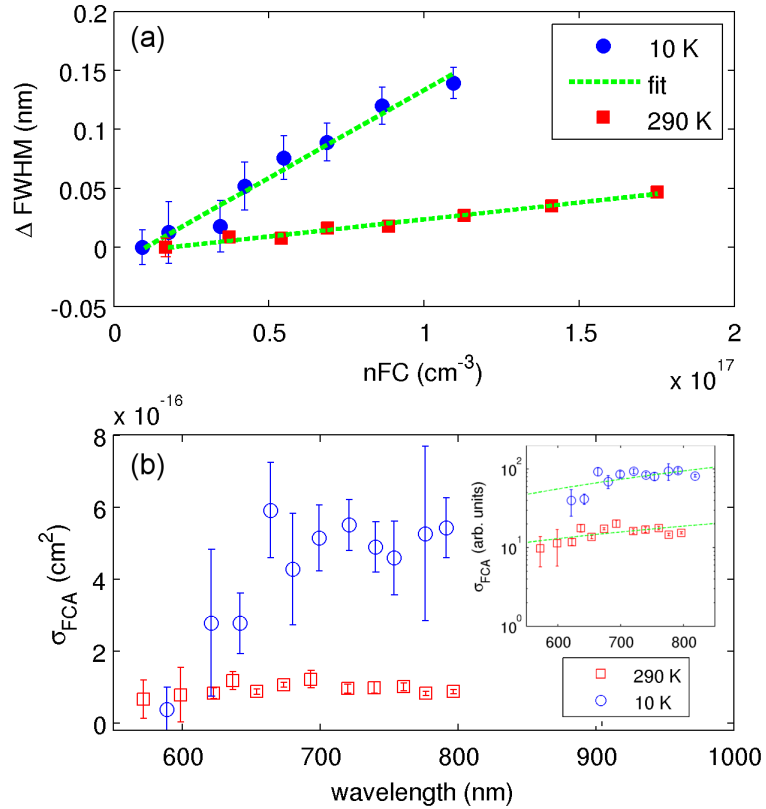


Figure 3.7: (a) The change in cavity linewidth as a function free carrier density for a representative cavity around 720 nm at 290 K and 10 K. Linear fits to the data are also shown. (b) The free carrier absorption cross-section (σ_{FCA}) obtained from linear fits such as those in part (a), as a function of wavelength, for different cavities throughout the PL spectrum of the Si-NCs. The inset shows the same data renormalized in a small V_m setting. The dashed lines represent fits to a λ^b model, where $b = 1.3$ and 1.8 for the 290 K and 10 K data, respectively.

While the calculation above allows easy direct comparison with the figures obtained in Ref. [93], they assume that the optical mode of the cavity is traveling in

an effective medium with some effective index and group velocity. While such an assumption is valid for large cavities such as μ -disks, they are oversimplified for the case of high Q , low V_m cavities. In the cavity setting, the Purcell enhanced strength of absorption is given by [104]:

$$\gamma \propto \int_{\omega} |g_0|^2 \rho(\omega) d\omega \propto \int_{\omega} \rho(\omega) / V_m d\omega, \quad (3.8)$$

where $|g_0|^2 \propto 1/V_m$ is the emitter-field interaction term, and $\rho(\omega)$ is the joint density of states associated with the electronic transition for FCA and the optical density of states of the cavity. However, since the transition for FCA is a broad continuum, the normalized narrow bandwidth optical density of states from the cavity is integrated out, resulting in no enhancement of the absorption rate in high Q cavities. Thus, in this case, the Purcell enhanced absorption should only be proportional to Ξ and the inverse of V_m . We renormalize the calculated σ_{FCA} of Fig. 3.7(b) with those considerations and plot the results in the inset of the same figure, along with their respective fits to a $\sigma_{FCA} \propto \lambda^b$ model. We obtained $b = 1.3$ and 1.8 for the 290 K and 10 K cases, respectively, which is more consistent with FCA being the cause of the power dependent absorption. This evidence suggests that cavity enhanced absorption may be applicable to processes such as FCA, and are not limited to just emission of single quantum dots [57], ensembles of atoms with large homogeneous broadening [96], and even Mie scattering [105]. Even more, the large effective absorption coefficients of Si-NCs in microcavities could hamper development of a lasing source, whether the Si-NCs serve as the emitters or as the sensitizer as in Si-NCs mediated emission from Er doped SiO_x . Finally, it is likely that cooling down systems involving Si-NCs would present additional challenges. Although many non-radiative phonon mediated recombination processes decrease with decreasing temperature, we have demonstrated that FCA increases dramatically with decreasing temperature as well, possibly offsetting some of the gains.

3.2 Erbium-doped Amorphous Silicon Nitride

In previous work, we have already demonstrated enhancement of Er PL in Er doped amorphous silicon nitride (Er:SiN_x) coupled to a two-dimensional (2D) hybrid Er:SiN_x -Si PC membrane cavity, including linewidth narrowing of the PC cavity mode and Purcell enhancement of the Er emission rate [96, 106]. Although silicon-based PC cavities have high Q and small V_m , the overlap of the cavity mode with the active material is small, as most of the cavity mode is confined in the higher index Si portion of the membrane. In addition, absorptive losses, stemming mostly from the Si portion of the membrane absorbing the pump light and creating free carriers, also limit the gain. As seen in the previous section, nanobeam cavity design enable high- Q cavities made with low index materials. Here we report on a nanobeam PC cavity design made entirely of the Er:SiN_x material, which have 12 times mode overlap relative to previous cavity designs [96] and reduced absorptive losses, as there is no longer Si present in the cavity. We demonstrate enhanced linewidth narrowing for these nanobeam cavities, and observe of material transparency.

We use the fabrication procedures of Appendix A.3, to fabricate the cavity designs of Sec. 2.1.3. The cavities are fabricated with a Type I membrane [inset of Fig. 3.8(a)] where the Er:SiN_x layer is 500 nm thick with an Er concentration of $3.0 \times 10^{20} \text{ cm}^{-3}$. We also fabricate cavities in Type II samples, shown in the inset of Fig. 3.8(b), with have only the middle third of the membrane doped with Er. The scanning electron micrograph (SEM) of the fabricated beam with a width of $w = 1.5a$ is shown in Figure 2.5(a).

As in previous work, we pump the Er $I_{15/2} \rightarrow I_{11/2}$ transition at 980 nm in order to reduce the total material losses [96, 107]. Micro-photoluminescence is performed from normal incidence for both the pump and the collection beams with a $100\times$ objective lens with numerical aperture $NA = 0.5$, and the emission is directed to an InGaAs CCD spectrometer. The bulk PL is shown in Fig. 3.8(a) for both room and 5.5 K temperatures. In the cavity PL we observe the two TE-like modes, and we choose to work with the first order (fundamental) mode, as it has the lowest mode volume. A sample cavity PL spectrum is shown in Fig. 3.8(a), and typical cavities

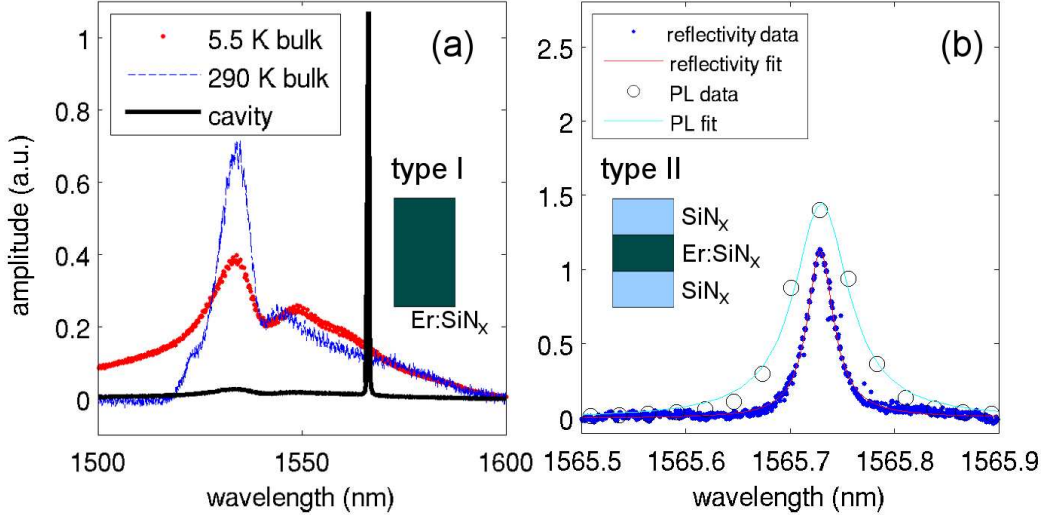


Figure 3.8: (a) Photoluminescence from the cavity at room temperature and the unpatterned film at room temperature and 5.5 K. The whole membrane is composed of Er:SiN_x in this case (type I, shown in inset). (b) Spectrum of a cavity fabricated in SiN_x with only the middle third doped with Er (type II, shown in inset). Dots correspond to the spectrum obtained by a laser scan in cross-polarization reflectivity, and circles to PL measured by the spectrometer. Fits to a Lorentzian lineshape gives a $Q = 52,000$ from the reflectivity scan and a spectrometer resolution limited $Q = 25,000$.

have $Q > 12,000$.

In addition, we also fabricate larger cavities with the same design parameters, except with $w = 2.5a$ and only the middle one-third of the slab doped with Er [type II in the inset of Fig. 3.8(b)]. In such a cavity, we measure a Q of 25,000 from PL taken with the spectrometer [Fig. 3.8(b)]. However, since the corresponding linewidth of 0.06 nm is limited by spectrometer resolution, a scan of the cavity is performed in cross-polarization reflectivity [58, 108] in steps of 0.002 nm with a tunable laser. The reflectivity scan data are also shown in Fig. 3.8(b), and yields a Q of 52,000.

We perform power series measurements on one cavity (type I) at both room and cryogenic temperatures, with pump powers varying from 0.030 mW to 40 mW. We plot the integrated intensity from the cavity, and the integrated intensity of the uncoupled PL from the main Er emission lobe at 1525 nm – 1540 nm (excluding the cavity, as the cavity and main Er emission lobe overlap), at both room temperature

and 5.5K [Fig. 3.9(a)]. The amplitudes of the cavity and spectrally decoupled PL both increase sublinearly at both temperatures. However, it is interesting to note that the PL from the spectrally decoupled regions have approximately the same saturation characteristics at both temperatures, while the PL from the cavity resonance rise with a higher slope on the log-log plot than that of their uncoupled counterparts at both temperatures. Such behavior suggests a faster spontaneous emission rate at the cavity resonance, due to Purcell enhancement of radiative emission rate. In addition, at both temperatures, the cavities redshift at high pump power, suggesting cavity heating [Fig. 3.9(b)]. Finally, Fig. 3.9(c) shows that at 5.5 K, the Q increases dramatically with pump power from 6,000 to over 15,000. On the other hand, at room temperature, the Q only increases from 14,000 to 16,000. In our previous work with an Er:SiN_x layer coupled to a Si 2D PC cavity, we observed a smaller increase in Q at cryogenic temperatures and negligible increase in Q at room temperature [96]. As previously, here we attribute the difference in the behavior of Q at the two temperatures to the broadening of the homogeneous linewidth of the Er emission transition with increasing temperature, which degrades Purcell enhancements of emission and absorption [96]. The larger changes in Q in the nanobeam cavity (relatively to the change in [96]) at both temperatures are the result of greater mode overlap with the active material and the reduction of free carrier absorption, as the 980 nm pump is absorbed more by Si than by SiN_x. Because of the redshift in the cavity resonance wavelength with increasing pump power, we conclude that heating mechanisms due to free carriers or Er-Er interactions may still lead to increased absorption at high pump powers. Nevertheless, the reduced cavity losses of the new cavity design have enabled the observation of linewidth narrowing at room temperature.

By changing the PC lattice constant, and while maintaining the same cavity design, we fabricate cavities with a variety of wavelengths that span the Er emission spectrum. At room temperature, we observe that all cavities have Q s at or above 10,000, at high or low pump power [Fig. 3.10(a)]. However at low temperature, all the cavities that overlap with the main Er emission lobe demonstrate lower Q s at low pump power (below 10 μ W pump). Then, by increasing the pump power, we observe a decrease in cavity linewidth and an increase in Q [Fig 3.10(b)], much like

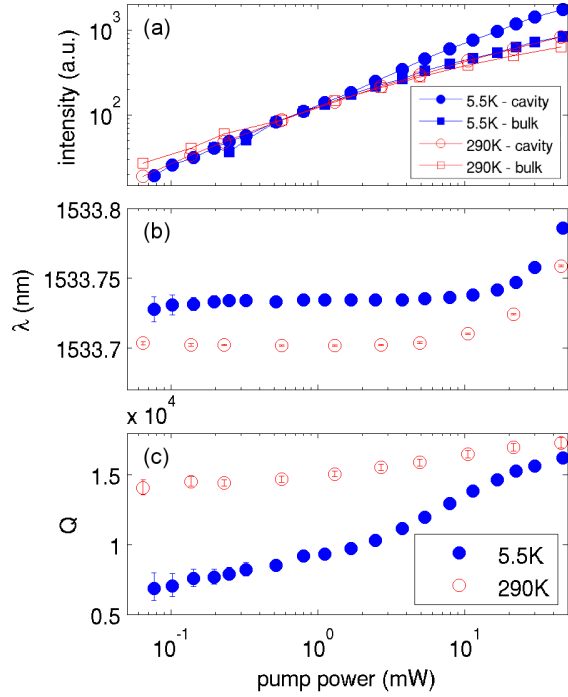


Figure 3.9: The pump power dependence of the (a) integrated PC cavity intensity and PL spectrally decoupled from the cavity, (b) the cavity resonance wavelength, and (c) the cavity Q , all at 5.5K and 290K. The pump power is measured in front of the objective lens.

in our previous work [96]. However, the linewidth narrowing observed in this work is more than double that of our prior work, as expected, because of the higher mode overlap and reduced free carrier absorption. The maximum observed linewidth narrowing is by 0.23 nm at 5.5 K. In addition, the change in linewidth decreases with increasing cavity wavelength to almost negligible amounts. The spectral dependence of the linewidth narrowing is expected, as the wavelength range from 1525 nm to 1540 nm corresponds to the peak of Er absorption, and the absorption decreases with increasing wavelength. As opposed to our prior work [96], here we observe linewidth narrowing for all cavities at room temperature as well [Fig 3.10(b)]. Although the linewidth changes at room temperature are much smaller than the changes for the same cavities at 5.5 K, they are still significant. At room temperature, the linewidth change is nearly the same for all cavity wavelengths. This can be explained by the

large homogeneous linewidth of the Er at room temperature (up to 10 nm in glass hosts), such that a significant portion of the Er population couples to the cavity resonance. We have previously found that the Q s of the cavities, and thus the Er homogeneous linewidth, vary smoothly between 5.5 K and room temperature [96]. In addition, as the system is in the bad emitter limit, the absorption and emission rate enhancements depend only on the mode volume and not the cavity Q factor. Thus, we have explored the two extremes of the temperature (5.5 K and 290 K) in order to display the largest variation in linewidth (at low pump power).

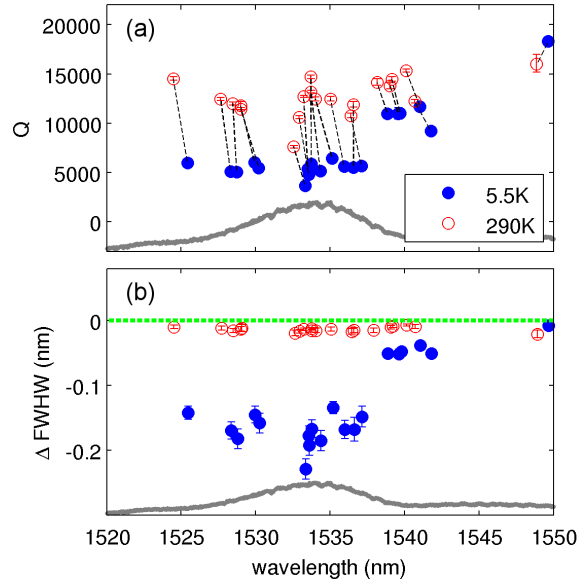


Figure 3.10: (a) The Q s of the cavities at 5.5K and 290K, both with low pump power (less than 10 μ W). The dashed lines connect the data for the same cavity at the two different temperatures. The shift in wavelength between the two temperatures is most likely due to a shift of the sample position in the cryostat as temperature is varied. (b) The change in the linewidth (full-width at half-max, FWHM) for individual cavities as pump power is switched from less than 10 μ W to 40 mW, at 5.5 K and room temperature. The scaled and shifted Er spectrum is shown in gray as a reference.

Time-resolved PL measurements are performed using the same setup as in our previous work [96]. In summary, a 980 nm pump laser is chopped at 50 Hz by a mechanical chopper, and the decay of the PL is sent to a superconducting nanowire

single-photon detector (SNSPD), which is held at a temperature of ~ 3 K in a closed-cycle helium cryocooler [109]. The chopper provides start pulses to the time-sampling electronics, while the SNSPD provides a stop pulse each time it detects a photon. The electronics record a histogram of the number of stop counts arriving in each 20 μ s time interval after a start pulse; this histogram is proportional to the time response of the PL to the square wave pump. Time-resolved PL for the cavity design with $w = 2.5a$ and the type II Er:SiN_x membrane [Fig 3.11(b)] for pump powers varying from 2 mW to 30 mW for the sample also at ~ 3 K. A clear increase in the initial decay rate from the cavity is observed. We also fit the decay traces to a double exponential with the decay time constants shown in Fig. 3.11(b). We observe that both the long and short decay lifetimes vary with pump power, which is consistent with the concept of stimulated emission. We note that the initial decay time constant is 4.0 ms for unpatterned film and 0.73 ms for cavity resonant emission. The measured total PL emission decay time constant (τ) from the unpatterned film is the parallel sum of the radiative (τ_r) and the non-radiative (τ_{nr}) decay time constants. On the other hand for a cavity, the radiative decay time constant is shortened by Purcell factor F_p , and the measured overall time constant for a cavity is:

$$1/\tau_{cav} = F_p/\tau_r + 1/\tau_{nr}. \quad (3.9)$$

The lower bound of the radiative lifetime of Er in bulk Si₃N₄ is 7 ms, as it is the longest total (combined radiative and non-radiative) lifetime observed for such a system [110]. Using this figure, we conservatively estimate $F_p = 6$ at 3 K at the lowest pump power.

We also observe that the Q s of the cavities with the type I membrane at 5.5 K and at high pump powers can sometimes exceed the Q s of the same cavities at high pump powers at room temperature. We find the difference between the linewidths of the cavity resonances at the two different temperatures at the same high pump power and plot them in Fig. 3.12(a). We observe that a cluster of cavities between 1535 nm and 1539 nm exhibit narrower linewidth at low temperature than at room temperature. Understandably, this range lies on the longer-wavelength side of the Er emission peak, where absorption from Er is lower compared to the shorter-wavelength

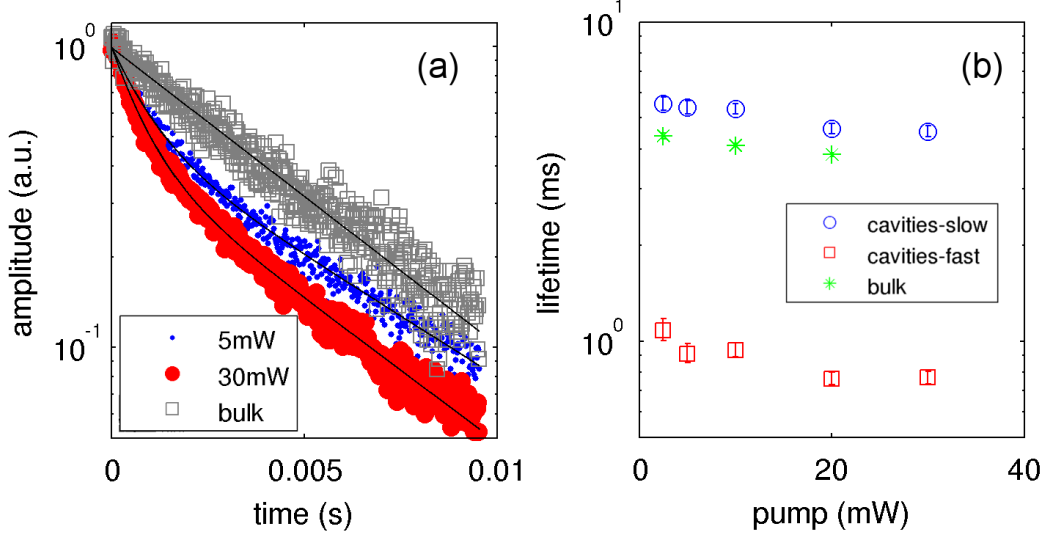


Figure 3.11: (a) Time-resolved PL measurements of the cavity resonance for various pump powers at ~ 3 K, as well as unpatterned film (integrated for all wavelengths). Solid lines for the cavity time traces are fits to a bi-exponential model. (b) The fast and slow components from the fits in part (a), as well as for an unpatterned film lifetimes for various pump powers.

side of the Er emission peak. The observation of narrower linewidth at 5.5 K indicates that larger gain is achievable at low temperatures than at room temperature.

In addition, we expect the pump power and temperature dependent absorption rate ($\gamma_a(P, T)$) to be related to the observed Q -factor of the cavity (Q_{obs}) by:

$$\frac{\omega_0}{Q_{obs}} = \frac{\omega_0}{Q_{cav}} - \gamma_a(P, T), \quad (3.10)$$

where ω_0 is the cavity frequency, and Q_{cav} is the intrinsic (no gain or loss) cavity Q . Because the light-in light-out (LL) curve does not indicate clear threshold behavior, the system operates well under any lasing conditions, and Eq. 3.10 is valid. However, as discussed in our previous work [96], $\gamma_a(T)$ is dependent on the Er homogeneous linewidth, and thus has a strong dependence on temperature. By using the time-resolved data above, we have estimated that the average enhancement of radiative lifetime to be 5 to 7 times stronger at ~ 3 K than at room temperature, the same as in our previous work [96]. At room temperature, the homogeneous linewidth of

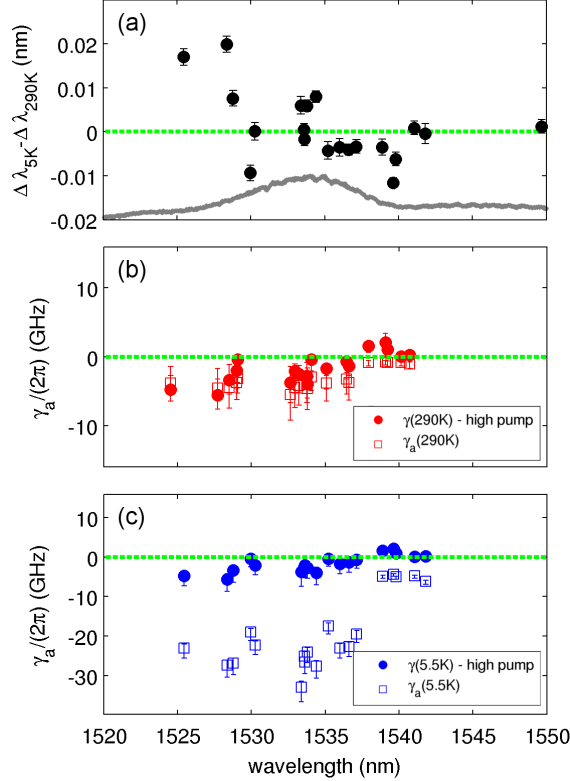


Figure 3.12: (a) The difference in between the cavity linewidth at 5.5 K and 290 K, under high pump power (greater than 40 mW). The scaled and shifted Er spectrum is shown as a reference. (b) The absorption rate achieved at room temperature under high pump power (circles) and low pump power (squares) calculated by use of the cavity Q_s measured in experiment, with error bounds assuming that the Er homogeneous linewidth at room temperature is between $\eta = 4$ and $\eta = 8$ times that at 5.5 K. (c) The absorption rate achieved at 5.5 K at high pump power (circles) and low pump power (squares), with the same error bounds as part (b). Regions with positive γ_a correspond to gain achieved with the system.

Er in SiN_x is estimated to be greater than 1 nm, and is much broader than the cavity linewidth. In that case, the system is in the bad emitter limit [111], and the spontaneous emission rate enhancement at room temperature is $F(T) \propto Q_{Er}/V_{mode}$, where $Q_{Er} = \omega_0/\Delta\omega_{Er}$, and ω_0 and $\Delta\omega_{Er}$ are the Er transition frequency and Er homogeneous linewidth, respectively. On the other hand, at cryogenic temperatures, if $\Delta\omega_{Er}$ were to be comparable to or smaller than the cavity linewidth (bad cavity limit), we would expect $F(T) \propto Q_{cav}/V_{mode}$, which in this case would be over 50 times

larger than at room temperature. Since we observe a change in Purcell enhancement of only 5 to 7, we confirm that the Er homogeneous linewidth limits Purcell enhancement at cryogenic temperatures as well.

Next, we use the time-resolved data to estimate the Er inversion fraction. We may write for a single cavity that $\gamma_a(290 \text{ K}) = \gamma_a$, where γ_a is the cavity dependent absorption rate, and that $\gamma_a(5.5 \text{ K}) = \eta\gamma_a$, where η is the factor by which the Er homogeneous linewidth decreases between room temperature and 5.5 K. By using $\eta = 6$ as observed from time-resolved spectroscopy, along with Q_{obs} (deconvolved from the spectrometer response) at low pump powers (Er all in the ground state) at 290 K and 5.5 K, we can find γ_a and Q_{cav} for each cavity using Eq. 3.10. We plot γ_a in Fig. 3.12(b) and (c) for room temperature and 5.5 K, respectively, and the data match well with the expected absorption spectrum of Er. In addition, we find the effective gain (or absorption) rate, namely, $\omega_0/Q_{obs} - \omega_0/Q_{cav}$, achieved at the cavity resonance wavelength for each cavity under different pump powers. We plot the results for room temperature and 5.5 K in Fig. 3.12(b) and (c), respectively, with the cases of $\eta = 4$ and $\eta = 8$ as the error bar bounds. As with the data in Fig 3.12(a), we observe that the fraction of inverted Er rises above transparency, i.e., γ_a equal to or greater than zero (otherwise $\gamma_a < 0$ denotes absorption loss), for the cavities coupled to the longer wavelength side of the main Er emission peak at both room temperature and 5.5 K. Once again, such an effect matches well with the pump power dependent gain curves of Er in glass [22]. The absorption coefficient (α) can be calculated from the absorption rate by $\alpha = -\gamma_a/(2\pi)/(c\Gamma/n_{eff})$, where for this cavity mode the effective index is $n_{eff} = 1.6$ and mode overlap with the active material is $\Gamma = 0.52$. At the Er emission peak, we obtain an absorption rate of $\gamma_a = 2\pi \times 6 \text{ GHz}$, which corresponds to an absorption coefficient of 0.6 cm^{-1} and is consistent with absorption rate of Er doped materials in silicon nanocrystal doped oxide and phosphate glass waveguide systems [112, 113]. Similarly, the maximum gain ($\gamma_a > 0$) obtained at 5.5 K and 290 K is $\gamma_a = 2\pi \times 2 \text{ GHz}$, which corresponds to $\alpha = -0.22 \pm 0.05 \text{ cm}^{-1}$. In general, we observe that at the long wavelength edge of the main Er emission peak, cavities are pumped to transparency.

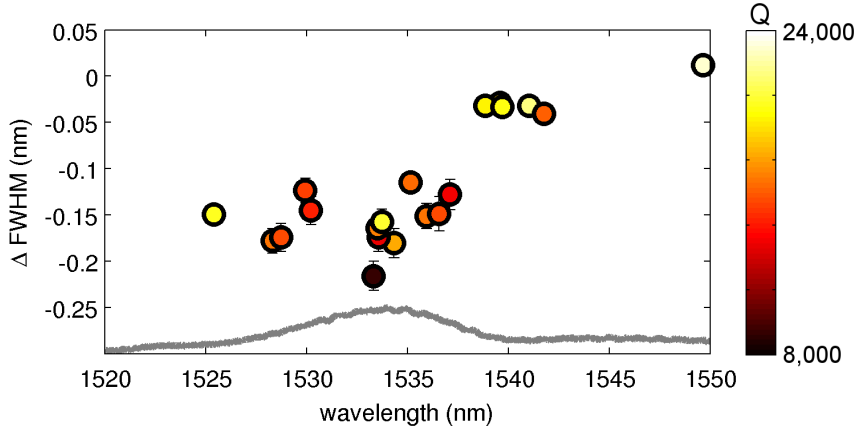


Figure 3.13: (a) The change in linewidth between 5.5 K and room temperature, both measured at low pump powers (below $10 \mu\text{W}$). The color of the points represents the intrinsic cavity Q -factor (Q_{cav}). The scaled and shifted Er spectrum is shown as a reference.

Finally, we confirm that the Purcell enhancement is degraded by the large homogeneous linewidth of the Er transition at both 5.5 K and room temperature. We plot the change in the cavity linewidth at low pump power between 5.5 K and room temperature for various cavities, which is representative of the absorption of the cavities at cryogenic temperatures, and simultaneously plot Q_{cav} on a color scale in Fig. 3.13. We observe that the change in the linewidth (i.e., the change in absorption) between the two temperatures is not strongly correlated with the intrinsic cavity Q -factor. Therefore, minimizing the cavity mode volume while keeping the cavity linewidth comparable to the homogeneous Er linewidth would achieve the maximum Purcell enhancement for Er coupled to nano-cavity structures.

3.3 InAs Quantum Dots in GaAs nanobeam laser

Two-dimensional PC cavities have had a large impact in the field of low-threshold lasers [114, 115], as high Q , low V_m cavities reduce the lasing threshold by increasing the spontaneous emission rate and channeling the enhanced emission into the cavity mode. The 1D nanobeam cavity design of previous sections can accomplish same effect, and very recently, lasing in such cavities incorporating quantum well material

has been demonstrated [116, 117]. In this section, we couple emission from InAs quantum dots (QDs) to nanobeam PC cavities, as the QDs have less non-radiative decay channels than quantum wells, and thus could enable very low lasing thresholds. Because the 1D PC lasers have small footprint, the cavities also have nanomechanical properties that could theoretically enable tunable lasers [118]. Finally, the nanobeam laser are also suitable for coupling to fiber taper, which is demonstrated in this section. We employ this coupling to tune the lasing wavelength by up to 7 nm by controlling the overlap between the cavity and the taper.

We study the lasing properties of GaAs nanobeam cavities with InAs quantum QDs at room temperature. We employ the same cavity design as in Sec. 2.1.4, fabricating cavities on a GaAs membrane of 240 nm (Appendix A.4). An example of a fabricated structure is shown in Fig. 2.6(a). We work with the fundamental TE-like mode (E -field in the xy -plane in the middle of the nanobeam) as it has the highest Q and lowest V_m among all TE-like modes. In experiment, we observe a significant reduction in Q relative to theoretical prediction (by an order of magnitude), resulting from fabrication imperfections (such as edge roughness from the dry etch and lithographic tolerances to the hole position), or from absorption losses in the QDs and the wetting layer. In fact, by simulating this structure directly [119] without absorption losses, we observe a reduction in Q to $Q \approx 20,000$.

We pump the cavities at both 780 nm (above the GaAs band gap positioned at $\lambda_g = 870\text{nm}$) and at 980nm (longer wavelength than λ_g , but shorter wavelength than the emission wavelength of the QDs, and slightly above the emission wavelength of the quantum well wetting layer at 1000 nm), both at room temperature. Suspended bridge nanobeam cavities have been shown to have very small heat conduction [99]. However, the 980 nm pumping avoids heating of the cavity at high pump powers, and allows high power continuous wave (CW) pumping. The CW pump laser is focused onto the beam from normal incidence with a $100\times$ objective lens with numerical aperture NA = 0.5. The photoluminescence (PL) from the sample is also collected from the direction perpendicular to the plane of the chip and sent to a spectrometer with an InGaAs CCD array. The PL from QDs in a unpatterned region of the sample is shown in Fig. 3.14. The PL spectra of various cavities with slightly different lattice

constants and radii are also shown in Fig. 3.14, with pump powers above threshold with the 980 nm pump. The Lorentzian fit to a cavity spectrum (pumped at 14 μW , below threshold) with $Q = 9,700$ is shown in the inset of Fig. 3.14.

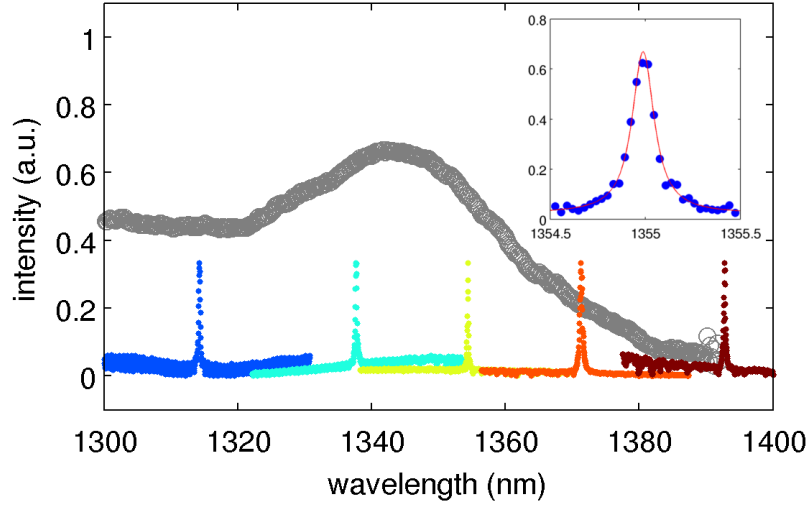


Figure 3.14: Normalized PL spectra from representative GaAs nanobeam cavities with embedded InAs QDs above lasing threshold (colored points). The PL spectrum from QDs in bulk (unpatterned film) is also shown (gray circles). The inset shows a zoomed-in cavity spectrum (pumped at 14 μW , below the lasing threshold) and its fit to a Lorentzian lineshape, corresponding to $Q = 9,700$.

We also study the pump power dependence of cavities by varying the pump power of an unchopped CW 980 nm laser from as little as 0.1 μW to as much as 10mW. The output power of the nanobeam laser as a function of the pump power is shown in Fig. 3.15(a). The experiment is repeated with the same cavity, but with the 780 nm pump [Fig. 3.15(b)]. We fit the data to the standard rate equations [120]:

$$\frac{dN}{dt} = \eta \frac{L_{in}}{\hbar\omega V_a} - N \left(\frac{F}{\tau_r} + \frac{1}{\tau_{nr}} \right) - v_g g P \quad (3.11)$$

$$\frac{dP}{dt} = \Gamma v_g g P + \Gamma \beta \frac{N}{\tau_r} - \frac{P}{\tau_p}, \quad (3.12)$$

where $N(P)$ represents the carrier (photon) density, F is the Purcell factor, η represents the fraction of incident pump power (L_{in}) absorbed in the active region, V_a is

the active volume of the laser, τ_r (τ_{nr}) is the radiative (non-radiative) recombination lifetime, $v_g = 1 \times 10^{10} \text{ cm/s}$ is the group velocity of light in the active medium, τ_p is the photon lifetime of the cavity, β is the fraction of spontaneous emission coupled to the cavity mode, and Γ is the mode overlap with the QDs. Because the homogeneous linewidth of such QDs at room temperature is approximately 10 meV [54], which far exceeds the cavity linewidth, the Purcell enhancement is negligible ($F \approx 1$) [21]. A logarithmic gain model $g = g_0 \ln(N/N_{tr})$ is used where g_0 is the gain coefficient in units of cm^{-1} and N_{tr} is the transparency carrier density in units of cm^{-3} [54]. The photon lifetime $\tau_p = Q/\omega$ is estimated from the linewidth of the cavity resonance around threshold to be 7.1 ps. The QD radiative lifetime in bulk, τ_r , is estimated from the literature to be about 3 ns [54], and the non-radiative lifetime, τ_{nr} , is too long to significantly affect the fits. We also expect that the non-radiative recombination occurring at the surfaces in our structures is significantly lower than in quantum well lasers, as a result of the spatial confinement of the QD exciton. This small non-radiative recombination rate, in addition to low threshold, causes a soft turn-on of the laser structures shown in Fig. 3.15(a).

Since it is difficult to estimate the gain parameters and the fraction of absorbed pump power in our structures, we fit the rate equations with β , g_0 , N_{tr} , and η as variable parameters. We simultaneously fit the data from the 780 nm pump and the 980 nm pump to the model with the same β , g_0 , and N_{tr} , but different η . The best fit to the data is obtained with $g_0 = 6.2 \times 10^4 \text{ cm}^2$ and $N_{tr} = 7.9 \times 10^{15} \text{ cm}^{-3}$, comparable to previous studies with similar quantum dots [54]. For our lasers we find $\beta = 0.88$, $\eta = 1.3 \times 10^{-5}$ for the 980 nm pump, and $\eta = 6.3 \times 10^{-4}$ for the 780 nm pump. The difference in η for the two pump powers is expected, since the 980 nm pump laser has lower energy than the GaAs band gap and therefore is weakly absorbed (only by QDs and the wetting layer). Despite low Purcell enhancement, a high β factor is achieved, resulting from redirection of spontaneous emission into a single mode, similar to vertical nanowire antennas [121, 122]. To find the threshold of the laser we use a linear fit to the light-in light-out curve above threshold, and find the thresholds to be $19 \mu\text{W}$ and $0.3 \mu\text{W}$, for the 980 nm and 780 nm pump, respectively. Again, the reduction in threshold at the shorter pump wavelength highlights the improved

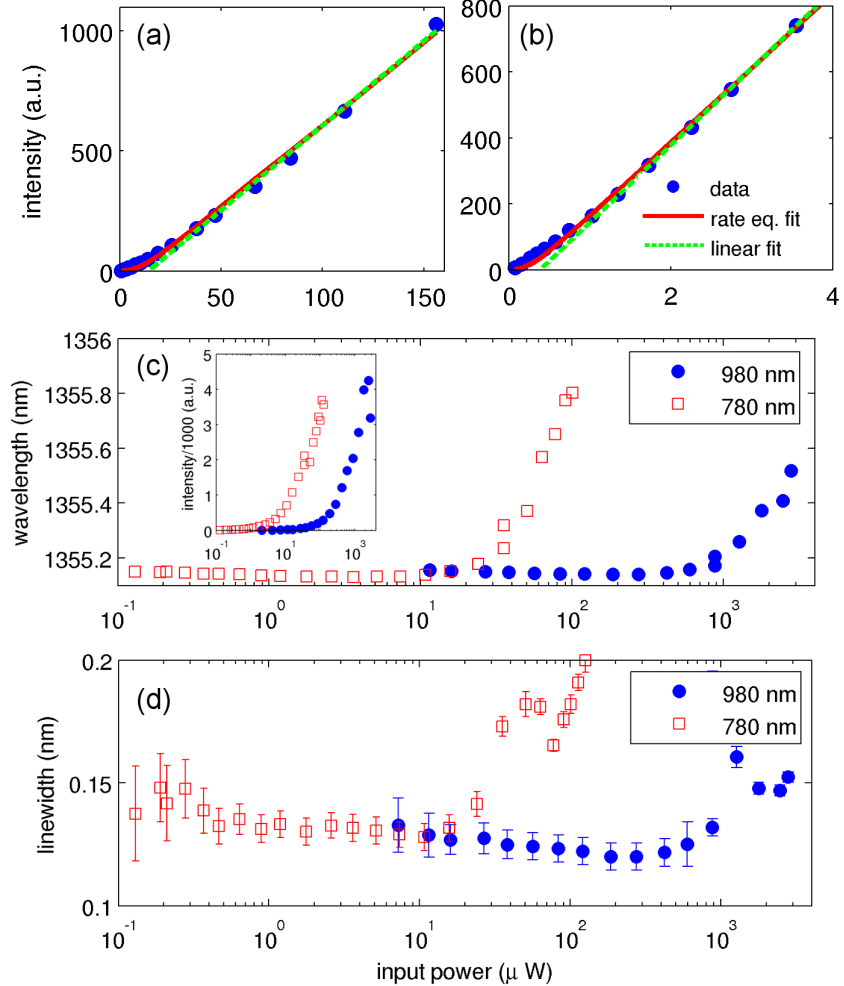


Figure 3.15: The light-in light-out curves of a representative cavity, using CW pumping at (a) 980 nm and (b) 780 nm. Fits from the rate equations, and linear fits to the above threshold behavior are also shown. (c) The power dependence of the cavity wavelength with 780 nm and 980 nm pump. The red-shift at high pump powers indicates structure heating, and it kicks off sooner if the above-GaAs bandgap laser (780nm) is employed, as expected. The inset shows the cavity intensity for larger pump powers, where the beginning of saturation is observed toward the end of both traces. (d) The power dependence of the cavity linewidth with 780 nm and 980 nm pump. The pump power (horizontal axis) is measured before the objective in all cases.

pump efficiency with the 780 nm pump. The threshold with the 780 nm pump is an order of magnitude lower than that ($25 \mu\text{W}$) reported in Ref. [54], where a chopped

CW pump ($100 \mu\text{s}$ on in a period of 1 ms) was used to reduce heating effects, and that ($2.5 \mu\text{W}$, in front of the objective) in Ref. [55], with CW pumping. We observe a reduction in threshold despite not using any chopping, which could come from the reduced number of QDs layers in our structure, or from the high β -factor of this cavity design.

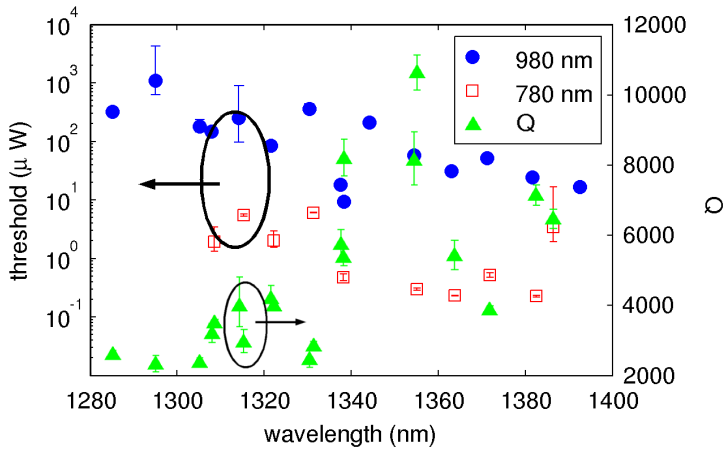


Figure 3.16: The thresholds of various nanobeam lasers obtained by linear fit to the above threshold behavior, using both the 780 nm and the 980 nm pump. Threshold pump powers are measured before the objective lens in all cases. The Q s of various cavities (all below threshold) are also shown.

In addition, we notice that two pump wavelengths create different behavior in the cavity heating. For both pump wavelengths, the cavity wavelength is unchanged at low pump powers, but begins to red shift at high pump powers [Fig. 3.15(c)]. Moreover, the wavelength shift for the 780 nm pump begins at lower powers than the one for the 980 nm pump, which is expected, as the 780 nm pump is more efficiently absorbed in the material. We also study the cavity linewidth as a function of pump power, but observe only a small narrowing [Fig. 3.15(d)], as the cavity linewidth is near the resolution of our spectrometer and small linewidth narrowing at threshold is a signature of high β factor lasers [123]. There is a noticeable increase in linewidth above $10 \mu\text{W}$ pump power associated with heating losses, and again occurring sooner with the 780 nm pump. Finally, in the inset of Fig. 3.15(c), we show the high pump power dependence of the cavity output intensity, and the end of each trace

represents the pump power where the cavity output starts to decrease. While the two pump wavelengths show approximately the same power output, the cavity linewidth is irreversibly broadened with the 780 nm before the saturation behavior (as in Fig. 3.15(d)), suggesting heating damage to the cavity. On the other hand, damage to the cavity is not observed with the 980 nm pump.

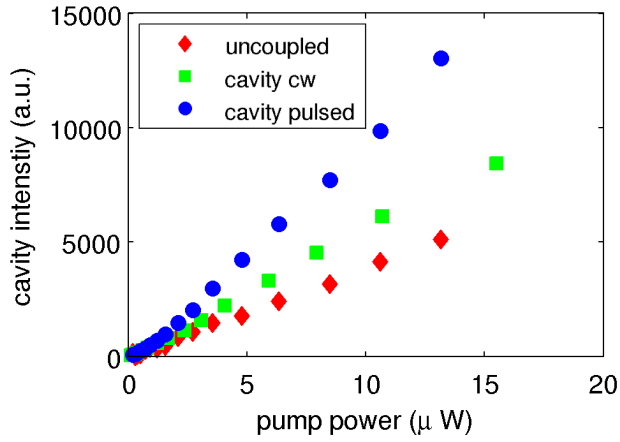


Figure 3.17: The light-in light-out curve for the same cavity as in Fig 3.15(a)-(b), pumped with a pulsed 830 nm laser, and by a CW 830 nm laser. The emission from a portion of the PL spectrum not coupled to the cavity is also shown. Pump powers are measured in front of the objective.

We also investigate multiple cavities throughout the PL spectrum of the QDs, finding each threshold by a linear fit to the above threshold behavior and plotting the results in Fig. 3.16. First, we notice that the thresholds increase by nearly an order of magnitude as we move toward the blue side of the PL spectrum, for both the 780 nm and the 980 nm pump. This results from the degradation of the cavity Q -factor with decreasing wavelength (Fig. 3.16). As more quantum dots are able to absorb the emission from the cavity, the Q falls well below the radiation limited Q found by simulation. In addition, we also observe that the use of the 780 nm pump always results in lower thresholds than the 980 nm, by approximately two orders of magnitude. Again, this corroborates the fact that the pumping above the GaAs band gap efficiently delivers carriers to the QDs.

In order to check the loss mechanisms due to heating, we also pump the cavity

with a pulsed 830 nm laser (35 ns pulse, 150 ns repetition period). It should be noted that this corresponds to a quasi-CW regime, as the pulse duration is much longer than any recombination time scales of the system, but the modulation helps reduce heating losses. The cavity emission as a function of the peak CW power is plotted in Fig. 3.17 for the various cases of CW and pulsed pumping. Lasing is observed in both cases, but the pulsed pump generated a higher slope of the LL curve. Moreover, the saturation at higher pump powers is delayed in the case of the pulsed pumping. This is attributed to the reduction of the heating effect, which leads to higher laser efficiency.

Finally, we attempt to tune the wavelength of the nanobeam cavities by bringing a fiber taper in close proximity to the cavity. Fiber taper fabrication details and experimental setup are the same as in Ref. [124], and a fiber taper with a diameter of approximately 1 μm was used in this work. In this configuration, we are able to both pump the cavity (at 780 nm) and collect the resulting 1.3 μm emission through the fiber. We observe the cavity spectrum as we move the fiber to different positions around the cavity, thereby changing the coupling between the fiber and the cavity. Because the fiber has a higher index of refraction than air, the effective index of the cavity is increased as the fiber overlaps more with the cavity mode, leading to a red-shift of the cavity mode [124]. In particular, we move the fiber along the y and z directions of Fig. 2.6(b), and plot the resulting spectra in Fig. 3.18(a). With the movements in the two directions, we demonstrate tuning of the cavity mode by over 7 nm. In addition, the Q factor of the cavity is not greatly deteriorated throughout the movement of the fiber, as the free space measured Q is 5,500, while the measured Q in the spectra in Fig. 3.18(a) range from 3,800 to 5,400. We simulate the full structure of the cavity with the fiber represented by a 1 μm diameter silica ($n = 1.5$) cylinder lying horizontally along the nanobeam long axis [inset, Fig. 3.18(b)]. We find via simulation that the fiber in full contact with the nanobeam redshifts the cavity resonance by 8.4 nm from the free space resonance wavelength, while supporting the same cavity mode with $Q = 15,000$ (compared to $Q=35,000$ of an unoptimized design without the presence of the fiber). These theoretical results match the experimental result of minimal perturbation of the cavity Q in experiment, while the reduced tuning

range of 7 nm could be due to imperfect positioning of the fiber on top of the cavity. If we were to use thinner membranes, the tuning range of the cavity mode could be even larger, as the design of the nanobeam cavity with $d/a = 0.7$ confines the mode well in the z direction.

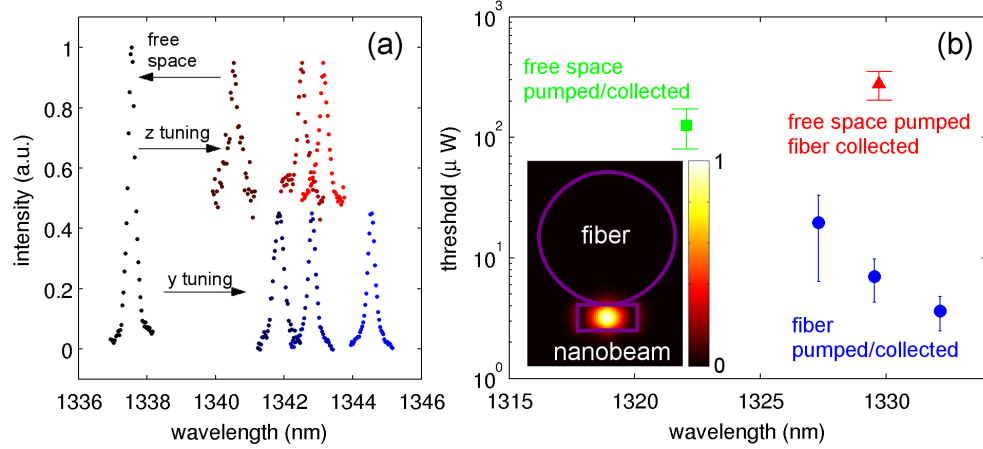


Figure 3.18: (a) Spectra from a nanobeam cavity as it is tuned by the movement of a fiber taper in close proximity to the cavity. The free space spectrum without the fiber taper is shown as a reference, and taper movement in the y - and z -directions (shown in Fig. 2.6) tunes the cavity mode by over 7 nm. The spectra for the tuned cavity are scaled for clarity. (b) The lasing thresholds of one cavity pumped from free space (normal incidence) and through the fiber taper, with collection through the fiber taper in both cases. The fiber taper position is varied to tune the lasing wavelengths. A reference case without any fiber tapers is also shown as the data point with the shortest wavelength. The inset shows the geometry simulated by FDTD, as well as the $|E|^2$ field of the cavity mode in the presence of the fiber taper.

We also pump another cavity through the fiber taper and through free space (from normal incidence) with the 980 nm laser, and with the fiber taper in various positions near the cavity (in both cases, emission is collected via the fiber taper). We observe lasing in both cases, with thresholds obtained from a linear fit to the above threshold behavior, as before [Fig. 3.18(b)]. The data point with the shortest wavelength represents the experiment without any fiber tapers, and we again observe that the cavity is red-shifted with the presence of the fiber taper. We also note that the fiber taper efficiently pumps the cavity, as we observe lower thresholds with the fiber taper pumping than with free space pumping. This efficient pumping is due to the localized

pumping of the cavity from the fiber taper [125]. Furthermore, the free space pump case with the presence of the fiber taper has a much higher threshold than any other case, most likely due to the fiber taper reflecting or redirecting the pump away from the cavity. Finally, we notice that the threshold changes by more than a factor of two over a small wavelength range as the cavity wavelength is tuned by the movement of the fiber taper. Such a large change is due to the change in pump efficiency, instead of the change in material absorption with wavelength. The taper is moved farther away from the center of the cavity as the cavity wavelength blue shifts, leading to reduced pumping of the cavity region and a higher threshold.

Chapter 4

Plasmonic Enhancement of Emission from Si-compatible Materials

We explore the alternative strategy of coupling active material to plasmonic structures. Because surface plasmon-polariton (SPP) modes have broad bandwidth, and can be excited in larger areas, they are a good fit for coupling to emitters such as silicon nanocrystals (Si-NCs) and Er. While Si-NCs have been previously coupled to isolated metallic disks [126], coupling to gratings allows enhanced out-coupling and easier configurations for electrical injection. We explore in greater detail the relationship between the size of plasmonic structures and the plasmonic enhancement of emission.

4.1 Plasmonic Enhancement of Silicon Nanocrystals

We first study the enhancement of Si-NC photoluminescence (PL) from a one-sided metallic grating fabricated on top of an active layer. We use the fabrication procedures described in Appendix A.6, which results in a 30 nm thick gold grating layer on top of

a 70 nm layer of Si-NCs, all on top of a quartz substrate (see structure in Sec. 2.2.2). The fabricated gratings have duty cycles of 0.6 to 0.8, but the overall trends of the PL data do not change over this range of duty cycles. Because the SPP mode of interest is confined to the Si-NCs-gold layer interface, we would expect the emission from the SPP mode to be redirected toward the Si-NCs and subsequently toward the quartz substrate. Hence, we pump Si-NCs with a green laser at 532 nm, and collect the emission from the back side of the sample with an objective lens with large numerical aperture NA=0.5, maximizing the collection [Fig. 4.1(b)].

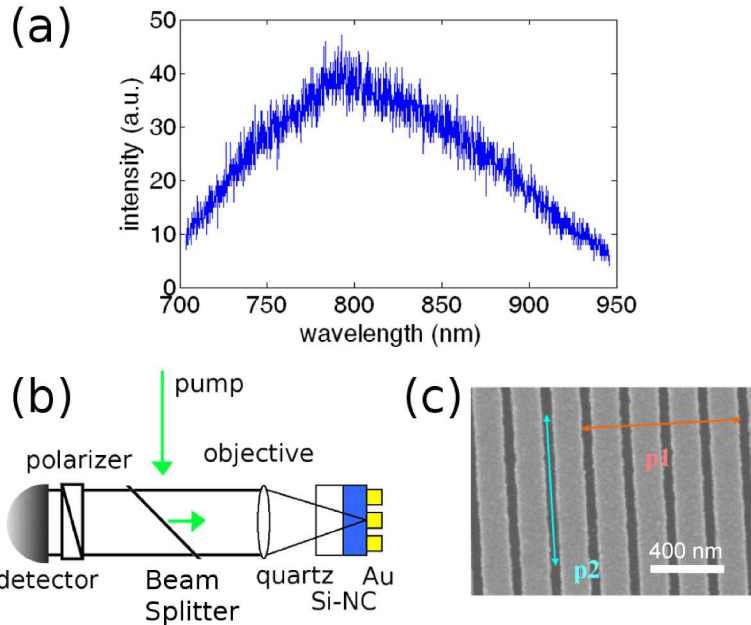


Figure 4.1: (a) PL from the bulk Si-NC wafer (unprocessed, i.e., without metallic grating). (b) Experimental setup. (c) Fabricated gold grating, with p1 and p2 denoting the two polarizations selected in the experiments.

The experimentally observed enhancement in emission rate is:

$$F_{meas} = \frac{\Gamma_{tot}}{\Gamma_0 + \Gamma_{nr}} = \frac{\Gamma_0 + \Gamma_{nr} + \Gamma_{pl}}{\Gamma_0 + \Gamma_{nr}} \quad (4.1)$$

where Γ_0 is the Si-NC spontaneous emission rate in bulk, Γ_{pl} is the emission rate of the Si-NCs coupled to the plasmon mode, and Γ_{nr} is the non-radiative recombination

rate. While the measured enhancement of collected PL intensity differs from the SE rate enhancement $F = \Gamma_{pl}/\Gamma_0$ from above, in the limit that the non-radiative decay rate is negligible ($\Gamma_{nr} \ll \Gamma_0, \Gamma_r$), the two figures are equal (assuming collection efficiencies for Γ_0 and Γ_r are equal in the optical setup). On the same chip, we create gratings with a range of periodicities and analyze the PL for each grating period. The SPP grating modes in Fig. 2.12(b)-(d) are predominantly polarized in the direction perpendicular to the grating bars [p1 in Fig. 4.1(c)]. In order to separate the enhancement due to SPP modes from other effects, we isolate two polarizations (p1 and p2) in experiment by collecting with different polarizer settings. The results are shown in Fig. 4.2(a)-(b). We observe that the PL polarized in the p1 direction (which coincides with the SPP polarization) has a shift in the peak wavelength with respect to the grating period, while the PL polarized in the p2 direction is fairly constant for all grating periods. The ratio of the two spectra, PL_{p1}/PL_{p2} , is then calculated and plotted in Fig. 4.2(c). There is a noticeable shift in the peak of the PL enhancement, and this enhancement can be strictly attributed to the enhancement of coupling to the grating SPP modes. The band edge mode frequencies for the second order mode at the Γ point ($k = 0$) and the third order mode at the X point ($k = \pi/a$) from Fig. 2.12(a) are redrawn on top of the experimental data. The theoretical and experimental data are a good match, as we see enhancement for the second order mode, which is in the collection cone of our objective, and suppression for the third order mode, which is outside of the collection cone. For the mode at the Γ point, we obtain an experimental maximum Purcell enhancement of approximately 2. While such enhancements are comparable to previous references, we also note that the obtained Purcell enhancement is averaged over the exponential decay tail of the SPP mode. Peak enhancements for some nanocrystals are thus even larger, much like in the case where quantum wells of smaller thicknesses are placed at an optimal distance away from the metal-dielectric interface [24].

To reach the range of the first order mode, we repeat the experiment for smaller grating periods (200 - 320 nm) as well, and plot the same PL_{p1}/PL_{p2} ratio in Fig. 4.2(d). We find that the PL emission is suppressed for grating periods below 350 nm by as much as a factor of 2, and the theoretically predicted first order mode wavelength

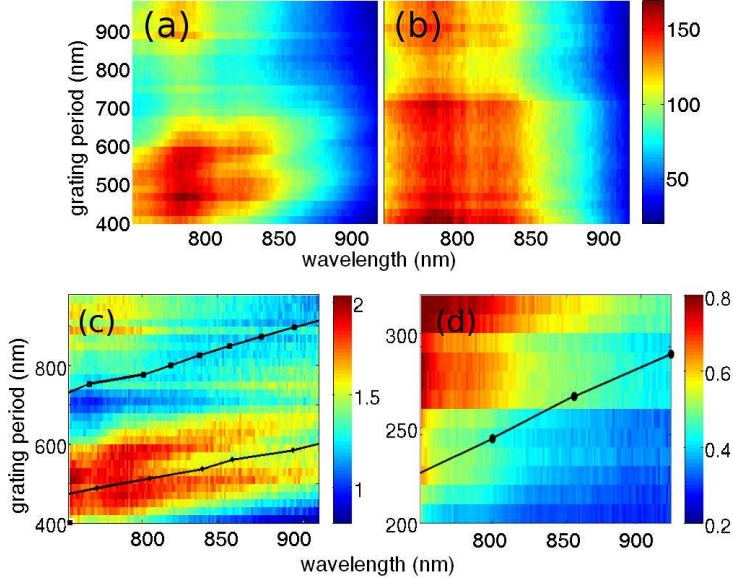


Figure 4.2: PL from Si-NCs near the grating for the (a) p1 and (b) p2 polarizations, from Fig. 4.1(a). (c) The ratio of PL spectra for the p1 and p2 polarizations. The second (diamond) and third (square) order mode wavelengths from FDTD are plotted again from Fig. 2.12(a). (d) PL_{p1}/PL_{p2} from Si-NCs coupled to the first order SPP grating mode. The FDTD calculated first order mode wavelengths are plotted again from Fig. 2.12(a).

matches the suppressed PL region in the middle and lower right the figure. Because the first order grating modes fall below the light line, they will not be collected into the objective, leading to the suppression of emission.

In order to extract the first order mode emission, we employ biharmonic gratings as discussed in previous works [127, 128]. In all the examples above, the single periodicity of the gold bars, a , establishes the edge of the first Brillouin zone at the X point. By introducing a secondary periodicity ($2a$) twice as large as the primary periodicity (a) into the gratings, we can scatter modes at the X point back to the Γ point, i.e., into the collection cone of the objective lens. In particular, the approach that was taken in this work was to create a skewed grating with a unit cell of two gold bars where the unit cell period is $2a$, the bar center-to-center width is a , the larger of the two bars has width $2ad$, and the ratio of the bar sizes is $1 : (1 - d)$ [Fig. 4.3(a)]. The gratings with primary periodicities from 200 - 320 nm and $d = 0.3$ are fabricated with the above

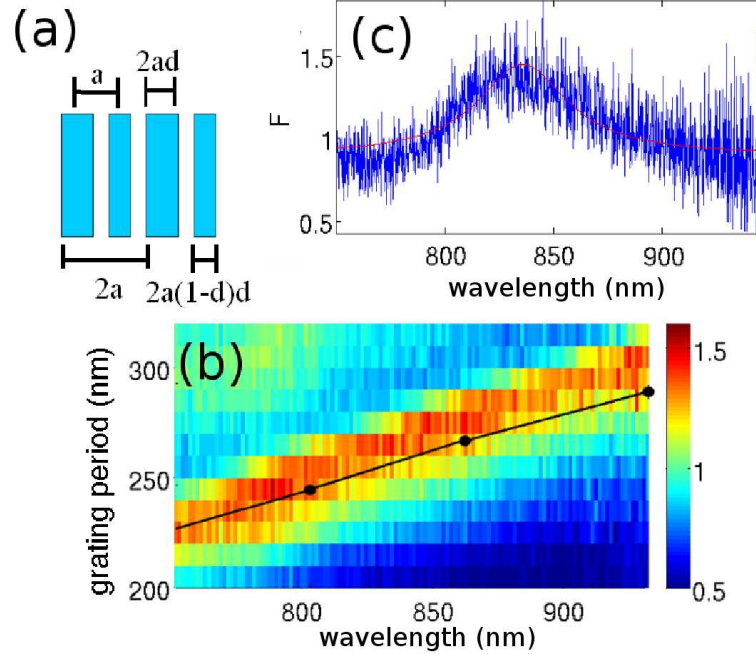


Figure 4.3: (a) Biharmonic grating design, where a is the grating period that couples Si-NC to the SPP mode at π/a , and d is the duty cycle that can vary between 0 and 1. (b) The enhancement of the p1 polarization by the biharmonic gratings. The first order mode wavelengths from FDTD are plotted again from Fig. 2.12(a). (c) Enhancement for one particular grating periodicity, with the red line being a Lorentzian fit of to data, representing quality factor $Q = 16$.

procedures and we plot the ratio PL_{p1}/PL_{p2} once more for these structures in Fig. 4.3(b). We observe the same red-shift in the PL as the grating period increases, but also observe a much narrower linewidth of the enhancement than in the enhancement from the second order grating. We show a fit to a Lorentzian lineshape corresponding to quality factor $Q = 16$ in Fig. 4.3(c). We redraw the grating periodicity against the band edges of the first order mode from the FDTD simulations above, and the peak enhancement follows the band edge at π/a well, implying that the first order mode is successfully extracted via such biharmonic gratings.

4.2 Enhancement of Er Photoluminescence via Metal-Insulator-Metal modes

We can also employ SPP modes to enhance broad homogeneous linewidth emitters such as Er, using devices like those detailed for enhancing Si-NC emission in the last section. Because Er emits at $1.5 \mu\text{m}$, we expect reduced ohmic losses for devices involving Er compared to Si-NCs. In addition, we employ metal-insulator-metal (MIM) modes to obtain high confinement of the SPP mode, using metallic confinement on two sides of an active material. The MIM confinement becomes more effective for longer emission wavelengths, as the effective mode volume (V_m) of the plasmonic mode is reduced for the same active material thickness. Active MIM devices have been previously considered in only III-V semiconductors [29] and in organic thin films [129]. On the other hand, single-sided modes have been used to enhance Er emission, where silver nanoparticles deposited on an Er doped silicon-oxide sample enhanced the collected emission from an ensemble of Er ions by a factor of 2 [130].

The material properties of the Er doped nitride layer are also suitable for incorporations in MIM devices, as Er-doped amorphous silicon nitride (Er:SiN_x) is a very robust material and can be deposited on a gold substrate at room temperature. Thus, the MIM structure with Er:SiN_x as the insulator can be fabricated with a bottom-up procedure, without the need for complicated epitaxial lift-off processes as in the case of crystalline semiconductors [29]. We use the fabrication procedure described in Appendix A.7, to fabricate MIM grating devices with various grating periods [30 nm gold grating - 52 nm Er:SiN_x - 100 nm gold substrate - silicon dioxide substrate, shown in Fig. 2.13(b)] such as the device shown in Fig. 4.4(a), imaged in an SEM.

In the experiment, we pump the MIM structure through the top-side plasmonic grating with a 400 nm wavelength laser diode, focused by a $100\times$ objective lens with numerical aperture $\text{NA} = 0.5$. The beam is focused down to approximately a $3 \mu\text{m}$ radius, smaller than the size of the structures ($10 \mu\text{m} \times 10 \mu\text{m}$). The output is collected through the same objective, and is directed to a spectrometer with the pump laser filtered out. The output PL for Er-doped amorphous silicon nitride (Er:SiN_x) deposited on gold, as well as for a sample grown and annealed on a quartz

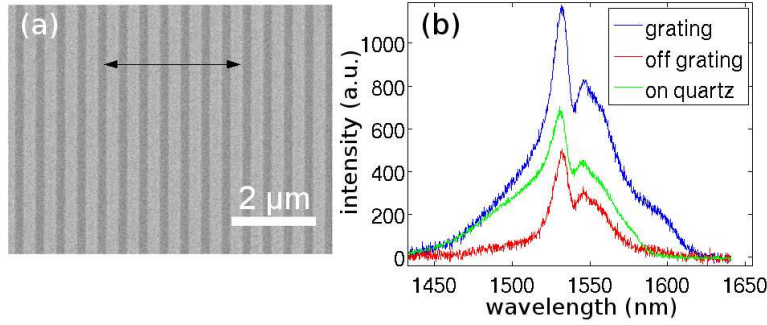


Figure 4.4: (a) Top gold grating fabricated on the $\text{Er:SiN}_x/\text{Au}$ substrate imaged by SEM. The double arrows indicate the approximate alignment of the polarizer (0°) (b) PL from on and off the grating structure, as well as from a reference sample with the same Er:SiN_x thickness grown on quartz. The same excitation power was used in all three cases. The region off the grating is a region with Er:SiN_x on top of Au without the top metal layer.

substrate under the same conditions, is shown in Fig. 4.4(b). The PL spectrum from the Er:SiN_x layer on gold is similar to the spectrum of Er:SiN_x deposited on quartz, while the total integrated intensity from the sample on the gold substrate is reduced by approximately a factor of 2. We perform lifetime measurements using the demodulation technique [131], and find that the Er:SiN_x deposited on gold has a lifetime of $100 \mu\text{s}$. We also measure the lifetime of the quartz substrate sample, both with and without a 30 nm gold layer on top of the Er:SiN_x layer, and observe lifetimes of $100 - 130 \mu\text{s}$. On the other hand, for samples of Er:SiN_x of the same thickness grown on quartz annealed at 1100°C , we observe lifetimes of 1.0 ms and 1.5 ms with and without a thick gold layer on top, respectively. In addition, the integrated PL for such samples was approximately 3 times higher than any of the samples annealed at lower temperatures. Based on these measurements, we conclude that the large decrease in Er emission efficiency when grown on metal is due to non-optimal annealing conditions. However, we also attribute some losses to the imperfect film quality on top of the gold substrate, but not to non-radiative decay mediated by SPP modes on the gold substrate.

Next we vary the period of the grating, and observe the enhancement of PL relative to the sample without the top metal layer (labeled as “off grating”). As seen in the PL

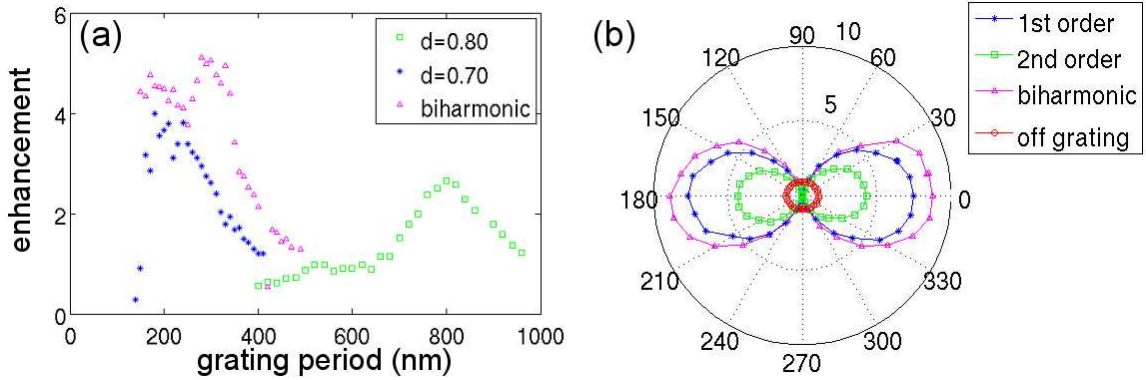


Figure 4.5: (a) The enhancement of integrated emission from grating structures relative to off grating areas, as a function of grating period. The three curves correspond to two different duty cycles (d), and to a biharmonic grating. (b) The enhancement of emission as a function of polarization angle for the resonant first and second order grating modes, as well as for the resonant biharmonic grating. The emission polarization angle dependence of the Er:SiN_x on Au off grating is also shown.

trace from an example grating structure in Fig. 4.4(b), the output is enhanced relative to the case without the grating. Because the observed plasmonic mode linewidth is broader than the erbium emission, we plot the integrated PL intensity over the emission spectrum for different periods of the grating, normalized by PL from an area off grating [Fig. 4.5(a)]. The duty cycle $d=0.7$, was fabricated at low grating periodicities, due to minimum feature sizes required for liftoff, while a higher duty cycle of $d=0.8$ was fabricated for higher grating periods. We find several resonant grating periods with maximum enhancement of approximately 4 and 3, respectively, for the periods of 250 nm and 800 nm. These correspond well to the FDTD calculated grating periods of 300 nm and 740 nm for the first and second order modes with resonances around $\lambda_0 = 1.54 \mu\text{m}$. The particular resonant grating period of 250 nm is well below the $\lambda/(2n)$ cutoff of purely dielectric modes, suggesting that the enhanced emission is coupled to plasmonic modes. Finally, the enhancement rolls off as the grating becomes non-resonant, with the enhancement of emission returning to unity. From the FDTD calculation, we estimate the Q -factors of the first and second order modes to be 3 and 5, respectively. We do not expect the linewidth of these modes to be broadened by collecting more than one point of the dispersion relation, as we

filter for one emission direction in the Fourier plane of the collection path without observing any changes in the spectral shape of the emission.

In addition, we perform polarization measurements on the periodic array by placing a half waveplate followed by a polarizer in the collection path. In all subsequent measurements, the horizontal direction (0°) corresponds to the polarizer set perpendicular to the grating bars (i.e., aligned with the wave-vector k), as shown in Fig. 4.4(a). In Fig. 4.5(b), we plot the angle dependence of the integrated emission intensity from structures at the two maxima of enhancement in Fig. 4.5(a), as well as from a region off grating. First, we find that the emission from off grating is unpolarized, as the angle dependence of the emission is mostly flat with minor perturbation coming from the angle dependent deflection from the optics. For the first order mode with the highest intensity enhancement, we find that the 0° polarization is greatly enhanced compared to the off grating emission, by factor of 7. As the polarization dependent enhancement rejects one half of the unpolarized off grating emission, the peak angular enhancement corresponds well to the peak enhancements of 3 to 4 measured without the polarizer. The maximum enhancement at 0° is expected, as the SPP mode is a longitudinal mode with polarization parallel to its k -vector. On the other hand, the emission in the orthogonal polarization is greatly suppressed. The suppression indicates that the PL in the orthogonal direction does not couple to the grating mode. In such a manner, the one-dimensional grating is an efficient polarization selective enhancement device.

We also attempt to enhance the output by employing biharmonic gratings as in previous reports [92]. Again, due to limitations in fabrication, the duty cycle was kept low for proper liftoff. The maximum duty cycle fabricated has average metal coverage of 56%. The enhancement with respect to the fundamental grating period is plotted in Fig. 4.5(a) and the angle dependence of the emission from the grating with maximum enhancement plotted in Fig. 4.5(b). As expected, the resonant grating period matches well with the resonance of single period grating, and also maintains the broad resonance of the first order grating modes. However, the maximum angle dependent enhancement increased to only 9.

In order to enhance the output for both polarizations, we fabricate nano-particle

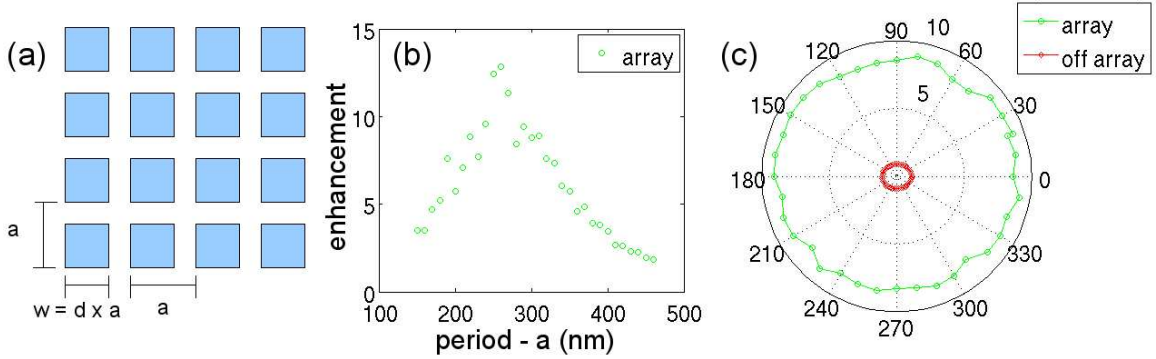


Figure 4.6: (a) The design of the square array of square metal particles. (b) The enhancement of emission from the shown nano-particle array structures relative to off-array areas, as a function of array period (a). (c) The angle dependence of the emission from a near-resonant nano-particle array with lattice constant of $a = 290$ nm.

arrays using the same procedure. In particular, we design a square lattice of square metal particles, with similar lattice constant as the one-dimensional gratings and duty cycle $d=0.7$ as defined in Fig. 4.6(a). We pump these structures in the same manner and observe the intensity of the output, plotted in Fig. 4.6(b). We note a maximum enhancement of approximately 12 for some structures, and the resonant lattice constant is similar to the resonant grating period of the one-dimensional grating. In addition, by measuring the angular dependence of the enhancement for the resonant lattice constant $a = 290$ nm as shown in Fig. 4.6(b), we notice that the output is unpolarized, which is expected from the symmetry of the two orthogonal plasmonic modes in the square lattice. We do not observe the diagonal traveling modes with grating period $250\text{ nm}/\sqrt{2}$, most likely due to the lack of symmetry of the individual square particles.

As shown in Figs. 4.5 and 4.6, we managed to collect emission from the first order modes of both the grating and the nano-particle array although they should be positioned below the light line. This suggests that scattering from rough metal surfaces or plasmonic resonances localized to individual metal particles, as opposed to coupled grating modes, may be the dominant effect in the observed enhancement. In order to study this effect in greater detail, we fabricate square arrays with the design in Fig. 4.6(a), but vary the duty cycle from $d = 0.3$ to $d = 0.7$. We plot the

enhancements corresponding to various duty cycles in Fig. 4.7(a). By plotting the enhancement versus the particle width ($w = d \times a$) in Fig. 4.7(b), we notice that the resonances correspond to similar particle widths, especially for low duty cycle. This indicates that modes localized to individual particles are the main contributors to emission enhancement and extraction. Furthermore, as the duty cycle increases, the particle width corresponding to maximum enhancement decreases. This is explained by the formation of coupled modes between the particles. For coupled modes, as shown by the field profiles in Fig. 2.13(b)-(c), the MIM mode is more confined to the Er:SiN_x layer, thus increasing the effective index. Such an effect in turn slightly reduces the frequency of the MIM mode for the same particle width, and requires a smaller particle to achieve the same resonant wavelength. We also note that the arrays of smaller period maintain relatively high enhancement despite being away from the plasmonic resonance. However, the modes of these closely packed particles resemble traveling waves of an unpatterned MIM slab (instead of individual particle resonances) and thus have wide bandwidth. Finally, the maximum enhancement increases with duty cycle. Because the effective pump reaching the Er decreases with increasing duty cycle (due to the presence of more metal), this indicates that the actual enhancements in the high duty cycle arrays are even higher than 12 and higher than in the low duty cycle case.

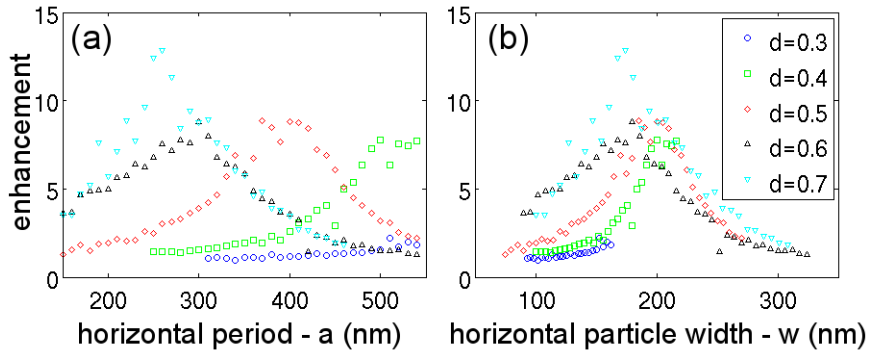


Figure 4.7: (a) The enhancement of emission from a square array of square metallic particles (Fig. 4.6(a)), as the duty cycle (d) and lattice constant (a) are varied. (b) The same set of data is replotted against the particle width, $w = d \times a$.

Finally, we attempt to quantify the coupling between the particles as a function

of particle separation and polarization. To do this, we fabricate rectangular arrays, where in the horizontal direction, gratings have width $w = 0.8a$, and we vary the period a . In the other direction, we vary period (v) by increments of 200 nm, with metal bar height (h) fixed to be $0.4v$ [Fig. 4.8(a)]. We measure the enhancements for different horizontal and vertical distances without a polarizer, and plot the results in Fig. 4.8(b). Here, we observe that the resonant horizontal periods of 210 nm and 550 nm are the same for all three vertical periods, while the overall enhancement is reduced for higher vertical period. This suggests that the plasmonic oscillations that enhance emission at the resonant grating periods are primarily in the horizontal direction, and that the oscillation frequency does not change with inter-particle separation in the vertical direction. The reduction in enhancement for larger vertical separation is due to the reduced overlap between the SPP mode and the active material for large v .

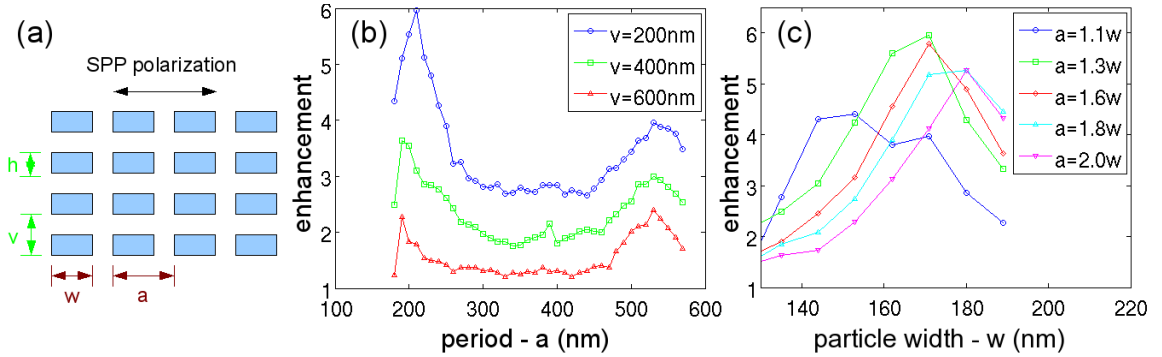


Figure 4.8: (a) Asymmetric particle arrays used to examine the role of inter-particle distance in the directions parallel and perpendicular to the plasmonic mode polarization. The vertical period v and horizontal period a are changed independently of each other. The polarization of the plasmonic resonances observed is shown by the double arrows. (b) The enhancement of emission from asymmetric particle arrays as a function of horizontal period a , while v is changed. Vertical period v is increased in increments of 200 nm. The particle has a width of $w = 0.8a$, and height of $h = 0.4v$ for all measurements. The horizontal period a that produces maximum enhancement remains the same for all v . (c) The enhancement of emission from arrays where v is fixed at 600 nm, h is fixed at 360 nm, and the horizontal width and period are varied independently.

In order to determine the role of inter-particle spacing in the direction of the plasmonic mode polarization, we fabricate gratings with the same fixed $v = 600$ nm

and $h = 360$ nm, but vary the horizontal particle width w and horizontal period a [Fig. 4.8(a)]. We plot the enhancement against the particle width for different horizontal separations in Fig. 4.8(c). As with the square lattice arrays, we observe a distinct shift in the resonant horizontal particle width as the horizontal inter-particle spacing is varied. The resonant particle width increases as the particles are pulled away from each other, again suggesting a decrease in the coupling between SPP modes on separate particles and a decrease in the overlap with the active material. This confirms that the particle arrays have resonant fields confined to the individual particles for large inter-particle separation, while supporting coupled modes for small inter-particle separation. We also note that the peak enhancement decreases with increasing particle separation above $a \geq 1.3w$, suggesting that coupled modes, with higher overlap with the active material, increase the overall enhancement. While the $a = 1.1w$ case has lower peak enhancement, pumping efficiency and outcoupling efficiency are reduced because of large metal coverage, and the effective enhancement may be larger.

Chapter 5

Passive Nanobeam Cavities

In this section, we experimentally demonstrate high Q passive cavities in silicon dioxide and silicon, which have relatively low and high index of refraction for semiconductor materials, respectively. We develop high Q cavities in these systems also using the nanobeam photonic crystal cavity design. The possible applications include bio-sensing and nano-opto-mechanics (described in Chapter 6).

5.1 Silicon dioxide nanobeam cavities

Silicon dioxide is an abundant material which is convenient for bio-medical applications because of the easy fabrication, low toxicity, and low absorption at visible wavelengths. However, designing a high- Q , small mode volume cavity in this material is a challenge, because of its low refractive index ($n = 1.5$) and the associated small size of the 2D PC bandgap. We use the low dimensional 1D PC (nanobeam) cavities that enables high Q .

We fabricated the device from Sec. 2.1.1 using the procedure in Appendix A.1, on a 270 nm thick SiO_2 layer on top of Si. The final fabricated structure is shown in Fig. 2.1(a). We vary the lattice constant a from 260 nm to 300 nm in fabrication to create cavities with a variety of wavelengths.

We characterize the cavities using the cross-polarized reflectivity measurement technique [58, 108]. In summary, white light linearly polarized 45° from the cavity

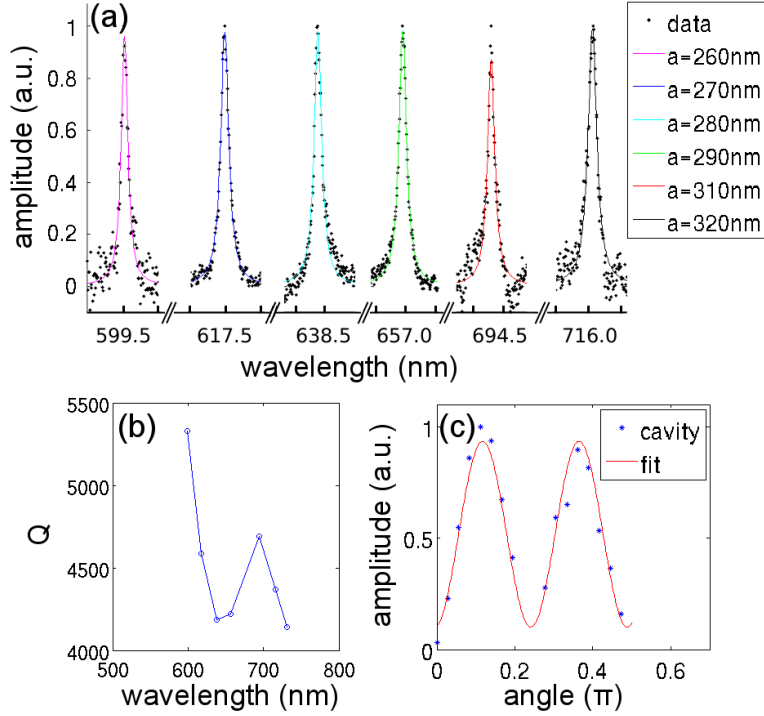


Figure 5.1: (a) The cavities spectra measured in reflectivity from structures with different lattice constants are normalized and shown together, with fits to Lorentzian lineshapes plotted on top of the data points. The cavity spectra are shown from left to right with increasing a . (b) The Q s of the cavities shown in part (a) plotted against the wavelengths of the cavities. (c) The angle dependence of the reflectivity amplitude. The horizontal axis corresponds to the half-waveplate angle, which is placed in front of the objective lens that is in front of the chip (and thus placed in both the incident and collection paths). The fit to the reflectivity amplitude shows a period very close to $\pi/4$, indicating a linearly polarized cavity mode.

polarization is directed at the cavity through an objective lens from above (z direction), and emission in the polarization orthogonal to the excitation (135°) is collected also from above and detected by a spectrometer. The fundamental mode of the cavity is linearly polarized in the direction perpendicular to the beam length [y -polarized in Fig. 1(b)], much like the fundamental TE mode of a rectangular slab waveguide. We observe cavities of different resonant wavelengths that span 600-716 nm in the visible wavelength range for different lattice constants, as shown in Fig. 5.1(a). The cavities are shown from left to right with increasing a . The measured cavity wavelengths and

Q s of the cavities are plotted in Fig. 5.1(b). While the measured $Q = 5,000$ is lower than the simulated value of 20,000, and the reduced value can be attributed to fabrication tolerances of the hole positions and edge roughness of the etched structure. Nevertheless, the experimentally achieved Q is a significant fraction of the simulated value. Similarly, the local variations of Q in Fig. 5.1(b) can be attributed to the same causes. By placing a half-waveplate in the incident/collection path, we confirm that the observed cavity mode is linearly polarized, as the angle dependent reflectivity amplitude has a period of $\pi/4$ with respect to the half-waveplate angle [Fig. 5.1(c)].

5.2 Silicon nanobeam cavities

High Q passive cavities in Si (without light emitters) are also interesting for a variety of applications, as Si is transparent in the telecommunication wavelengths around 1.5 μm , where cavities in Si can serve as filter banks and other functions. In addition, the Si cavities can be used for studies in optomechanics, as discussed in Chapter 6.

An alternative cavity design to the designs used in Chapter 3 (where the holes size shrinks toward the center of the cavity) is the design in Sec. 2.1.4, where the holes radii are tapered down away from the central cavity. We fabricate the single beam cavities (length of 13 μm , single beam widths of 550 nm, $r = 0.28a$, and the total cavity length is 34 holes), again with the procedures described in Appendix A.5, on a 160 nm thick SOI sample. The fabricated cavity is shown in Fig. 5.2(a), and also has waveguides attached configured for cross-polarization measurements [such as the ones shown in Fig. 6.1(a)]. The optical transmission spectrum is shown in Fig. 5.2(b), and again we observe the multiple orders of modes. The inset of Fig. 5.2(b) shows a laser scan of the fundamental mode, with a fit to a Lorentzian lineshape with $Q = 1.3 \times 10^5$. Thus, we are able to measure the cavity transmission of a high- Q cavity in this configuration.

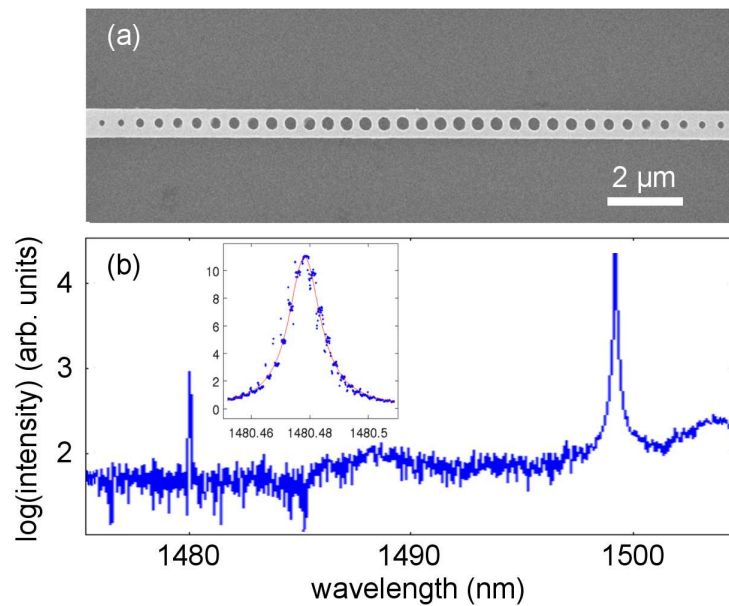


Figure 5.2: (a) SEM image of the fabricated structure with the alternative hole taper-out design. (b) The transmission spectrum of this cavity found with a broadband LED bank. The inset shows a laser scan of the fundamental cavity peak in transmission, along with a fit to a Lorentzian lineshape with $Q = 1.3 \times 10^5$.

Chapter 6

Optomechanics in One-dimensional Photonic Crystal Cavities

Optomechanics, the study of the interaction between light and mechanical motion, has recently captured the imagination of photonics researchers [132, 133]. For example, researchers have probed radio frequency (RF) mechanical motion of nanometer sized objects [67, 134]. In addition, proposals for using the optical gradient force to induce mechanical motion [135, 136, 137] with [134, 138, 139, 140, 141] and without [142, 143, 144] the use of an optical cavity have been experimentally demonstrated. In fact, at very high optical and mechanical confinement [134, 145, 146], the amplitude of a mechanical mode can be greatly increased. In such a manner, cavities with passive light emitting materials can serve as active emission sources of phonons.

The experiments above have been done with continuous-wave (CW) excitation of an optical cavity or modulated excitation of a waveguide. However, the CW excitation mechanism requires the mechanical motion to induce an out-of-phase modulation of the laser input, as only those forces in quadrature with the mechanical motion perform mechanical work on the structure. Such effects are generally small, as the thermal motion of the structure only weakly perturbs the optical transmission properties of a waveguide or cavity. In the CW case, the amount of work done on the mechanical cavity is proportional to κ^{-2} , where κ is the optical field decay rate in the cavity.

However, an alternative to increase the transduction between optical power and mechanical motion is to use modulated pumping [142, 143]. Such a scheme can do work that is proportional to κ^{-1} , and greatly reduce the amount of power needed to excite the mechanical mode (see Appendix D). In this section, we demonstrate the use of optical pump modulation in conjunction with an optical cavity to reduce the amount of power needed to actuate the mechanical mode. Because of the optical confinement and recirculation of photons, we hope to obtain large mechanical oscillations without regenerative feedback.

In particular, we choose to work with the double beam one-dimensional photonic crystal (PC) cavity configuration in silicon, such as the cavities in Sec. 5.2. Due to its high optical quality factor ($Q > 10^4$), which enhances the circulating optical power inside the cavity, and low mode volume ($\sim (\lambda/n)^3$), which also enhances the local field potential, the PC cavity can greatly enhance the optical gradient force. The optomechanical coupling rate is defined as:

$$g_{\text{OM}} = \frac{d\omega}{dx}, \quad (6.1)$$

where ω is the optical cavity frequency and x is the mechanical displacement of the cavity. By using cavities where the E -field is increased near material boundaries (such as in a slotted design [67, 147]), the frequency perturbation with mechanical motion and the optomechanical coupling can both be tailored.

We fabricate devices on a silicon-on-insulator (SOI) wafer with a 150 nm thick layer of Si and a 1 μm thick oxide layer, such as the cavity shown in Fig. 6.1(a). The beam cavities have lengths of approximately 13 μm , single beam widths of 550 nm, and a middle slot width of 100 nm. We use the design of Ref. [76], and detailed in Sec. 2.1.4 with the hole lattice constant $a = 400$ nm. The hole at the center of the cavity has radius $r = 0.28a$, and the total cavity length is 34 holes. The cavities are fabricated with the procedures in Appendix A.5 on a 160 nm thick silicon on insulator (SOI) layer with a 1 μm oxide sacrificial layer. In addition to the beam cavity, we also attach coupling waveguides on both sides of the cavity, and one of the waveguides is bent 90° to configure the device to be probed in a cross-polarization geometry [Fig.

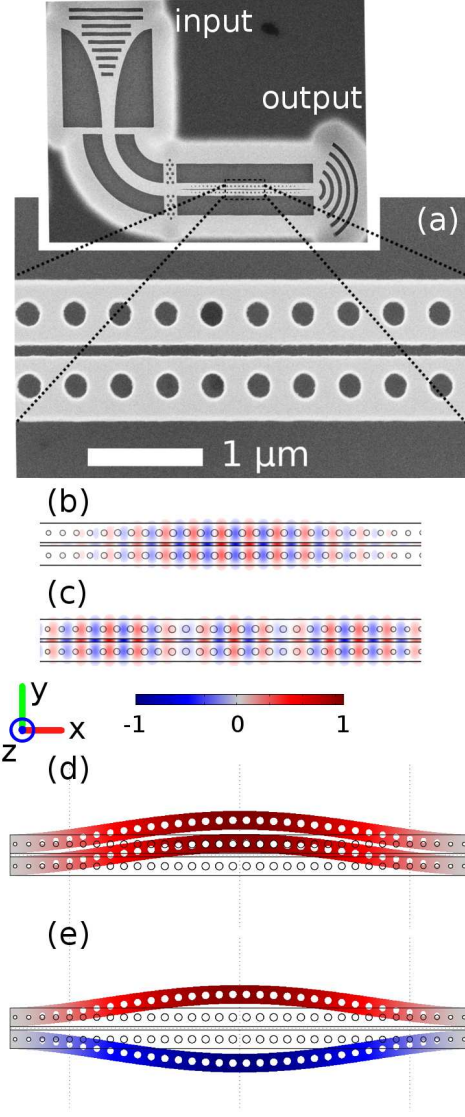


Figure 6.1: (a) Scanning electron microscope image of the fabricated cavity. The E_y field of the (b) $TE_{1,+}$ and (c) $TE_{2,+}$ optical modes. (d) The first order common in-plane mechanical mode, and (e) the first order differential in-plane mechanical modes are plotted with the color map assigned to the in-plane (y) motion.

6.1(a)] [58, 108].

We first simulate the beam cavities in the optical regime using the three dimensional finite-difference time-domain (3D-FDTD) method. Double beam cavities support bonded (+) and anti-bonded (-) optical super-modes, formed from the

transverse-electric (TE) modes of the individual beam cavities. In particular, the E_y field is symmetric or anti-symmetric about the xz -plane going through the slot for the bonded and anti-bonded modes, respectively. We find that the first ($\text{TE}_{1,+}$) and second ($\text{TE}_{2,+}$) order bonded modes [see Fig. 6.1(b)-(c)] have theoretical radiation-limited Q s of 30,000 and 1,500, respectively. We observe an enhanced electric field in the air slot region for the bonded modes because of the continuity conditions for the dominant E_y field at the slot boundaries (i.e. continuity of the displacement vector $\epsilon\vec{E}$). Thus, we expect that the bonded optical modes have the highest optomechanical coupling to the in-plane mechanical modes, as the high electric field concentration in the middle of the cavity enhances the change in the optical cavity frequency with mechanical deformations. For this reason, we work with the first and second order bonded optical modes in our experiments.

We experimentally analyze the optical properties of the cavity using the setup in Fig. 6.2(a). We pump the cavities with a broadband LED bank, which is coupled into a waveguide using a dielectric grating coupler. We align the cavity such that the input grating polarization is along $|H\rangle$, while the output polarization is along $|V\rangle$, to obtain the maximum signal to noise ratio. The transmission characteristics of the cavity are shown in Fig. 6.2(b), where we are able to observe the first two orders of the bonded and the anti-bonded modes. We are able to differentiate the bonded modes from the anti-bonded modes by moving the input beam on the grating coupler to change the input parity. The first order modes have high Q -factors, and we use a tunable laser to fully characterize the cavity. The laser scan at low input powers (1 nW) shows a Lorentzian spectrum with $Q \approx 15,000$ for the bonded first order mode ($\text{TE}_{1,+}$) [inset, Fig. 6.2(b)]. In addition, we observe that the higher order bonded mode ($\text{TE}_{2,+}$) has $Q \approx 2,000$. Both Q values are comparable to the FDTD simulated values.

We next use the COMSOL finite element solver to find the frequencies of the mechanical modes, using library parameters for silicon: Young's modulus of 131 GPa, Poisson's ratio of 0.27, and a density of 2.33 g/cm³. As described above and in previous work [67], mechanical modes with in-plane (in this case, referring to the xy plane) motion will have significant optomechanical coupling to the bonded modes. In

particular, we find the first order common and differential modes for in-plane motion [67]. The common and differential modes have the beams moving in phase and out of phase, primarily in the y -direction, and have displacement profiles shown in Fig. 6.1(d) and (e), respectively. By simulating the structure observed in the SEM image, we find that these two mechanical modes have mechanical frequencies of 25.72 MHz and 26.74 MHz. We find the optomechanical coupling strength similarly to previous work [134], with the optomechanical coupling length defined as:

$$\frac{1}{L_{\text{OM}}} = \frac{1}{2} \frac{\int dA \left(\frac{dq}{d\alpha} \cdot \hat{n} \right) \left(\Delta\epsilon |E_{||}|^2 - \Delta(\epsilon^{-1}) |D_{\perp}|^2 \right)}{\int dV \epsilon |E|^2}. \quad (6.2)$$

Here, q is the mechanical displacement, α is the parameterized displacement of the mechanical mode, \hat{n} is the surface normal vector, $E_{||}$ is the electric field parallel to the surface, D_{\perp} is displacement field normal to the surface, $\Delta\epsilon = \epsilon_1 - \epsilon_2$, and $\Delta(\epsilon)^{-1} = \epsilon_1^{-1} - \epsilon_2^{-1}$, with ϵ_1 being the dielectric constant of silicon, and ϵ_2 the dielectric constant of the surrounding medium. Because of the high E -field enhancement in the slot and the differential mechanical resonance having opposite parity to the E_y field, we observe very strong optomechanical coupling lengths of $L_{\text{OM}} = 1.3 \mu\text{m}$ and $1.8 \mu\text{m}$ for the coupling between the differential mechanical mode and the $\text{TE}_{1,+}$ and $\text{TE}_{2,+}$ optical modes, respectively. On the other hand, the coupling between the $\text{TE}_{1,+}$ and $\text{TE}_{2,+}$ optical modes and the common mechanical mode was calculated to be far weaker ($L_{\text{OM}} > 40 \mu\text{m}$), because this mechanical mode has the same parity as the optical field.

In order to first characterize the mechanical modes of the system, we pump the second order bonded mode with a red detuned probe laser, at the cavity half-max, with low pump power ($300 \mu\text{W}$ before the objective) to observe the mechanical modes in air. The transmission signal is fiber-coupled and sent to a photodiode detector with a transimpedance gain of $2.5 \times 10^4 \text{ V/A}$ and a bandwidth of 125 MHz, and the electrical signal is then read by an RF spectrum analyzer. We estimate coupling efficiencies of 2% to the $\text{TE}_{2,+}$ mode and 0.5% to the $\text{TE}_{1,+}$ mode, assuming symmetric losses at the input and output gratings, and accounting for the transmission losses of the coupling waveguides using FDTD simulations. We observe the two mechanical modes

in the RF spectrum, shown in Fig. 6.3(a), which correspond well to the simulated in-plane mechanical mode frequencies, and slight discrepancies can be attributed to minor differences in the clamping conditions of the fabricated device. Because of the low optical Q of the $\text{TE}_{2,+}$ mode and the low optical power buildup, we do not observe the giant optical spring effect seen in previous works [67, 141], as the mechanical modes do not change frequency with increasing pump power. We also do not observe significant changes in the optical cavity wavelength with pump power, suggesting minimal heating. Because of the mechanical damping of the ambient atmosphere, the mechanical Q -factors of these modes are limited to 50-100. When we test the same cavity in vacuum, we observe the two modes more clearly, as shown in Fig. 6.3(b). In vacuum, the mechanical Q ’s are as high as 2,500, and are limited by the clamping geometry of our cavity. We choose to work with the higher frequency mode (the differential mode), as it is the in-plane mechanical mode with higher optomechanical coupling to the second order optical mode.

Next, we pump the $\text{TE}_{1,+}$ mode with a second (pump) laser tuned to the optical cavity resonance wavelength and sinusoidally modulated near the RF frequency of the mechanical mode, while keeping the first CW laser tuned to the half-maximum of $\text{TE}_{2,+}$. We observe the effect of the second, modulated laser on the RF modulation of the first laser. We scan through the first-order optical mode with various unmodulated powers, and observe that the first order cavity resonance is not significantly changed, suggesting that the injected power on the first order optical mode does not change the temperature of the beam, and thus does not modulate the beam transmission via the thermo-optic effect. Although both lasers pass through the cavity and are extracted with the same output grating coupler, the laser on $\text{TE}_{1,+}$ is blocked by a band-pass filter centered at 1550 nm with a full-width at half-max of 12 nm. The power of the laser on $\text{TE}_{1,+}$ is modulated by a Mach-Zender interferometer modulator with a bandwidth of 2.5 GHz and full modulation depth [Fig. 6.2(a)]. First, we fix the input power on the first-order optical mode at under $2 \mu\text{W}$, and scan the modulation frequency through the mechanical resonance. When we tune the RF input frequency near the mechanical resonance frequency, we observe a narrow response in the RF spectrum (of the laser on $\text{TE}_{2,+}$) [Fig. 6.3(c)]. In addition, as the RF input frequency

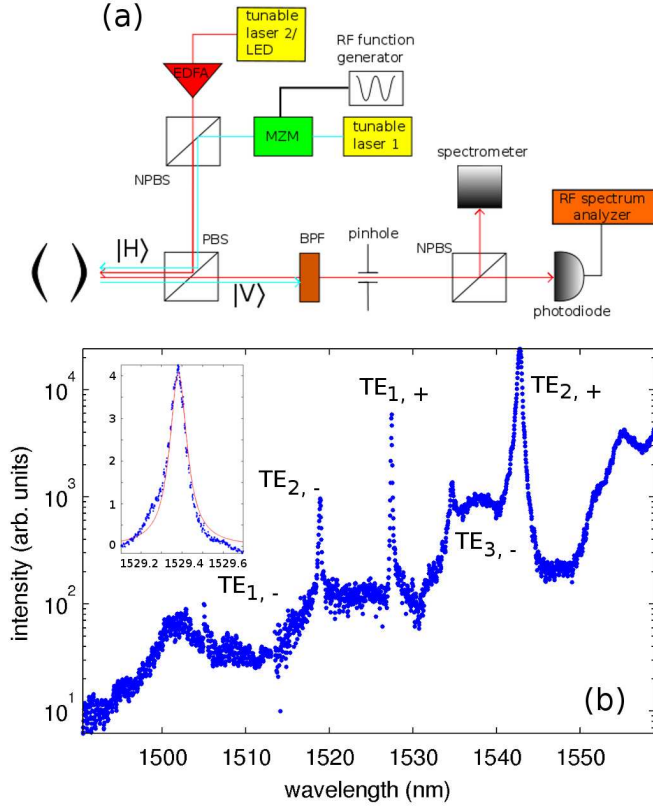


Figure 6.2: (a) The optical setup used to probe the optomechanical cavity. (b) Spectrum of the cavity observed in transmission using a broadband LED. The first and second order bonded (+) and anti-bonded (-) modes are labeled. The inset shows a laser scan of the $TE_{1,+}$ cavity mode for excitation, with a fit to a Lorentzian lineshape having $Q \approx 15,000$.

is tuned around the mechanical resonance frequency, we observe that the integrated power within the narrow bandwidth response matches exactly that of the mechanical cavity resonance [Fig. 6.3(d)], suggesting that the optical power in the first order mode is modulating the transmission properties of the second order mode through the mechanical resonance. In addition, we observe the Lorentzian mechanical mode with far better signal to noise, and can observe the tails of the mechanical mode even when detuned by more than three mechanical cavity linewidths.

We also measure the RF response of the probe laser on $TE_{2,+}$ as we change the power of the modulated pump laser on $TE_{1,+}$. We first do so with the probe power

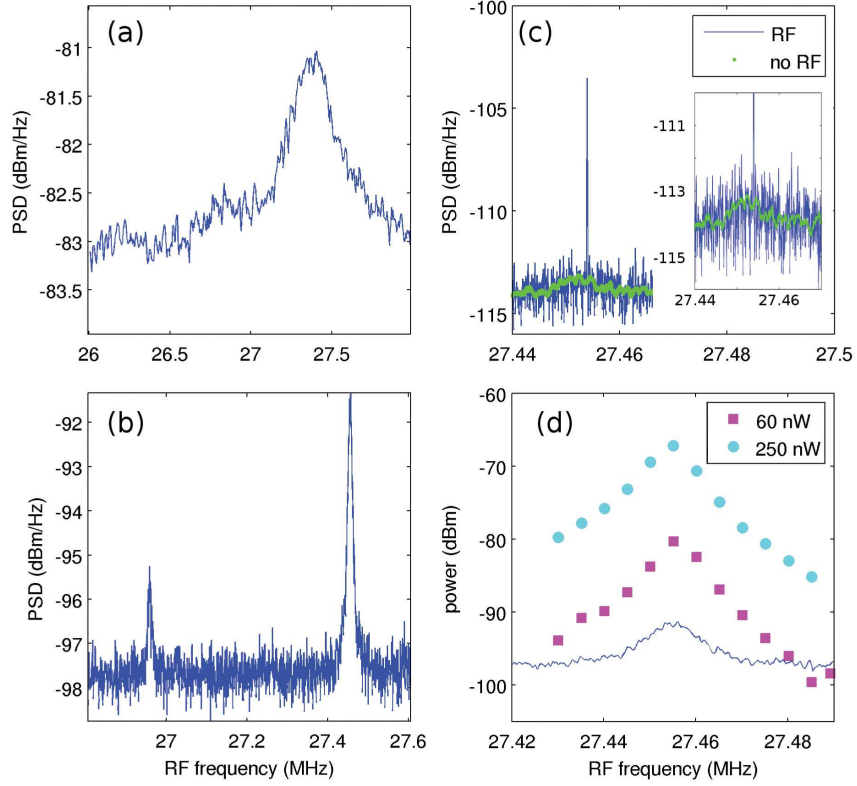


Figure 6.3: The RF spectrum of the mechanical modes under study in (a) ambient atmosphere, and in (b) vacuum. (c) The time averaged spectrum of the differential mechanical mode from part (b) is shown (green points), observed as RF sidebands of the laser tuned to $\text{TE}_{2,+}$. The non-averaged RF spectrum showing the sharp RF response when a modulated laser is pumped on $\text{TE}_{1,+}$ is also plotted (blue line). The inset shows the same data zoomed in, to observe the thermal driven mechanical mode in the background. (d) The integrated power within the sharp RF response of the laser on $\text{TE}_{2,+}$ [from (c)] with different RF modulation frequencies of the laser on $\text{TE}_{1,+}$. The two dotted curves correspond to two different average input powers on the first order mode and fixed input power on the second order mode. A closer zoom of the mode shown in part (b) of the figure is shown as a reference at the bottom (blue).

for $\text{TE}_{2,+}$ fixed at $2 \mu\text{W}$ coupled into the cavity, and observe the RF response with varying average power on $\text{TE}_{1,+}$ for different RF detunings from the mechanical resonance [plotted on a log-log scale in Fig 6.4(a)]. Similar to the data in Fig. 6.3(d), we observe the RF response is decreased as the modulation frequency is detuned from

the mechanical resonance. We observe that the relationship between the integrated power in the RF response and the input laser power on $\text{TE}_{1,+}$ is quadratic for all detunings. This is expected, as the RF spectrum analyzer measures the power of the voltage signal from the transimpedance amplifier of our detector, and that power has a quadratic relationship with the amplifier output voltage and thus a quadratic relationship with the output RF oscillation amplitude. This indicates a linear relationship between displacement and input pump power on the first order mode.

We also measure the RF power spectrum from $\text{TE}_{2,+}$ when we fix the average laser power on $\text{TE}_{1,+}$, and increase the power of the pump on the second order mode, as shown in Fig 6.4(b). Again, we observe that the integrated RF response of the driven mechanical mode is quadratic with the input power, which is expected as the sideband amplitude is linearly related to the probe power. We also obtain the RF response as a function of the input power on $\text{TE}_{1,+}$ for various probe powers on $\text{TE}_{2,+}$, shown in Fig 6.4(c). The RF response is reduced for lower input powers, as the sideband powers are proportional to the input probe power. However, we are able to observe an RF response with only 100 nW coupled to the $\text{TE}_{1,+}$ mode to drive the mechanical oscillations, and only 200 nW coupled to the $\text{TE}_{2,+}$ mode to sense the mechanical motion.

Finally, we compare the efficiency of exciting the mechanical mode in vacuum and in ambient atmosphere. We fix the input power for the probe laser on the $\text{TE}_{2,+}$ mode in both air and vacuum to 2 μW , and obtain the same output coupled power into our photodetector. We obtain the power series from the same cavity under both conditions, which is shown in Fig. 6.4(d). As expected, the amplitude of the mechanical oscillation is significantly higher in vacuum than in ambient atmosphere, due to the higher mechanical Q . In fact, the experimentally measured factor of 20 between the power needed to generate the same RF response in air and vacuum matches well with the ratio of mechanical Q s for the two conditions (31).

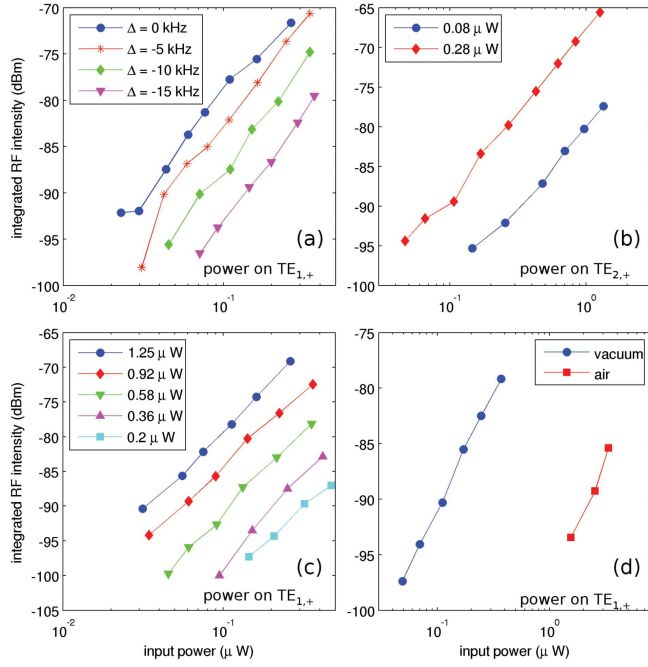


Figure 6.4: (a) The integrated intensity in the RF response collected from $\text{TE}_{2,+}$ as a function of average input power on $\text{TE}_{1,+}$ for different detunings of the RF modulation frequency from the mechanical resonance at a fixed probe power ($2 \mu\text{W}$) on $\text{TE}_{2,+}$. (b) The integrated intensity in the RF response as a function of different probe powers on $\text{TE}_{2,+}$, at two different fixed average pump powers on $\text{TE}_{1,+}$. (c) The RF response as a function of input power on $\text{TE}_{1,+}$ with different probe pump powers on $\text{TE}_{2,+}$. (d) The integrated RF response as a function of average pump power on $\text{TE}_{1,+}$. The two curves correspond to the response at ambient atmosphere and in vacuum, both with the same probe intensity on the $\text{TE}_{2,+}$ ($2 \mu\text{W}$).

Chapter 7

Conclusion and Future Directions

Because of the low light emission efficiency of silicon compatible materials, significant research must be done to promote the integration of electronics and optics. We have demonstrated a variety of nanophotonic structures to enhance the emission of silicon compatible materials, and demonstrated that these devices can also be applied to novel studies such as optomechanics.

First, we have theoretically and experimentally implemented high Q 1D PC cavities for low index materials such as silicon oxide and silicon nitride. Due to the reduced dimensionality, 1D PCs have bandgaps that are more conducive to making confined cavities modes. We have designed cavities with $Q > 10,000$ for materials with index as low as $n = 1.5$, and implemented the same designs for higher index materials. We were also able to obtain experimental $Q > 5 \times 10^3$, while maintaining low mode volumes in SiO_2 , while obtaining $Q > 10^5$ in a high index $n = 3.5$ Si system.

We have also applied these cavities to a variety of active materials, including Si-NC doped silicon oxide, Er-doped silicon nitride (Er:SiN_x), and InAs quantum quantum dots (QDs) in GaAs. First, we fabricated the nanobeam cavities in the Si-NC material, operating in the visible wavelengths. We were able to measure the free carrier absorption processes in such cavities, indicating that the absorption cross-section of the Si-NCs is further increased when the NCs are placed in a high Q , low V_m cavity, and we observed a difference in behavior between room temperature and cryogenic temperatures. We also applied the nanobeam design to the Er:SiN_x system. We

have observed enhanced absorption and gain characteristics in the Er:SiN_x compared to our previous work with a hybrid Er:SiN_x-Si PC cavity [96], due to the increased overlap of the cavity mode with the active Er material and the reduction of material losses. Because of the reduced loss mechanisms, we were able to observe material transparency at both room temperature and cryogenic temperatures. Finally, we have demonstrated low threshold CW lasing from InAs QDs embedded in 1D nanobeam PC cavities. We have investigated the wavelength dependence of the lasing threshold, and we have demonstrated that the nanobeam cavity laser can be tuned by a fiber taper in close proximity to the cavity.

In the future, the development of higher Q photonic cavities and the improvement of emission properties of the employed materials should occur simultaneously. The increase of photon confinement and the reduction of loss processes such as free carrier absorption will enable devices to reach the lasing threshold at lower pump power, and spawn devices with a variety of applications. The nanobeam cavities in particular are interesting for sensor applications, as their cavity modes have high overlap with the environment. In addition, the narrow linewidths of nanobeam cavities and the compatibility of the design with a variety of materials could be an enabling technology for displays, as accurate control of colors can be defined from a broad emission background. Nevertheless, cavity design for low index materials remains an interesting challenge, as ultrahigh Q ($> 10^6$) cavities have yet to be fabricated. Finally, the mechanical properties of the nanobeam cavity should be explored, as mechanical flexibility should translate into flexibility in manipulating the optical properties of cavities through a variety of mechanical forces.

As an alternative to high- Q photonic modes, we have also designed plasmonic cavity and grating structures that have moderate Q but low mode volumes that break the diffraction limit. First, we have proposed and studied a planar DBR plasmonic cavity that could enable high radiative quality factor. We have demonstrated that such a cavity indeed arises from the bandgap effect of plasmonic gratings, and that small V_m cavities can enable high Purcell enhancements. We have also demonstrated enhancement of emission from Si-NCs coupled to wide area SPP grating modes and Er:SiN_x coupled to metal-insulator-metal (MIM) SPP modes. Because of the higher

confinement of the MIM mode, we were able to demonstrate an order of magnitude increase in collected emission intensity from a MIM structure with Er:SiN_x as the active material. The device has been fabricated with simple bottom-up procedure and does not require complicated flip-chip bonding [29]. In addition, we have identified both local and coupled SPP modes supported by metallic gratings and nano-particle arrays.

For all of the plasmonic structure designs, future work should focus on confining the electromagnetic field in the third dimension (besides the SPP evanescent field direction and the DBR direction), so as to fully realize the small mode volumes of the SPP modes. In addition to improving the material properties of silicon-compatible emitters, work should also focus on improving the fabrication processes so that metals can be placed next to active materials without reducing the efficiency of emitters. Finally, metallic systems such as the MIM structure certainly have the potential to be electrically pumped since the metal layers could serve as the electrodes, and proper band engineering must be investigated to inject carriers into the active material in this configuration.

Finally, we have demonstrated resonant actuation of a mechanical mode with optical gradient forces in a Si nanobeam cavity. The input power needed to observe driven motion of the mechanical cavity is greatly decreased in the presence of an optical cavity, and hundreds of nanowatts can drive the mechanical motion via a modulated laser coupled to a second cavity mode. The research of optical forces coupled to mechanical structures is nascent, and there are a variety of opportunities available. First, the mechanical motion itself can be thought of as an active material, generating phonons. Thus, the control, emission, and transport of the phonon quantum can be greatly explored. In addition, the mechanical deformations can be coupled to a wide variety of active materials, such as InAs quantum dots, and the rich area of electron-phonon interactions can be explored. Finally, the actuation of mechanical motion can also be used for a variety of applications, such as mechanical motors that do work on nanometer-sized objects, finally enabling Richard Feynman's dream of machines building machines on the nanoscale.

Because of the new capabilities and figures of merit achieved by optical cavities,

new applications using the control of light at the nanoscale will continue to become available, from telecommunications to lighting, from quantum optics to mechanical motion. As always, there will need to be foresight to fit nanoscale devices into the niche demands and appropriate usage. The future of nano-optics will certainly be bright as the field finds and meets the desirable applications.

Appendix A

Fabrication

The specific fabrication processes for the various photonic crystal and plasmonic structures are described below. The electron beam resist (polymethylmethacrylate - PMMA, or ZEP-520A) was spun by the Headway spinner. ZEP-520A requires a 30 minute warm up time at room temperature. Both PMMA and ZEP-520A were baked at 200°C for 2 minutes. After etching or evaporation, PMMA was removed by acetone, while ZEP-520A was removed by remover PG, with or without sonication. If additional cleaning was required, an oxygen plasma was used at 20 sccm, 150 mTorr, and 100 W RF power on Drytek 4.

A.1 Silicon Dioxide beam cavities

We start by oxidizing a silicon wafer, forming a 270 nm layer of SiO_2 on top of silicon. Next, e-beam lithography is performed with a 250 nm layer of ZEP-520A as the resist (8.0 krpm spin). After development of the resist, the pattern is transferred to the oxide layer with a $\text{CHF}_3:\text{O}_2$ (100 sccm/2 sccm ratio) chemistry dry etch, at 100 mTorr and 150 W forward power (Drytek 4) for 380 s. Finally, the beam is undercut with a 1.0 Torr XeF_2 dry etch for 30 s, removing approximately 4 μm of silicon under the oxide layer.

A.2 Silicon dioxide beam cavities with embedded Si nanocrystals

The Si-NC doped oxide layer is grown on top of a silicon substrate by PECVD at 350°C in a N₂ atmosphere with a gas flow of SiH₄:N₂O=1400:300 sccm. The growth rate is approximately 46 nm/min, and the final oxide thickness is 200 nm. The sample is then annealed in a N₂ atmosphere at 900°C for 1 hr, followed by a forming gas (95% N₂, 5% H₂) anneal at 500°C for 1 hr. The refractive index of the layer is measured as $n = 1.7$ at 700 nm by ellipsometry. Next, e-beam lithography is performed with a 250 nm layer of ZEP-520A as the resist. After development of the resist, the pattern is transferred to the oxide layer with a CHF₃:O₂ (100 sccm/2 sccm ratio) chemistry dry etch, at 100 mTorr and 150 W forward power (Drytek 4) for 330 s. [69]. Finally, the beam is undercut with a 1.0 Torr XeF₂ dry etch for 30 s, removing approximately 3 μm of silicon under the oxide layer.

A.3 Er-doped Silicon Nitride Beam Cavities

Er:SiN_x is grown on top of an oxidized silicon wafer by N₂ reactive magnetron co-sputtering from Si and Er targets in a Denton Discovery 18 confocal-target sputtering system, as discussed elsewhere [43, 44], on top of an oxidized silicon wafer. The sacrificial oxide layer is 700 nm thick. The growth is followed by a post-annealing process in a rapid thermal annealing furnace at 1180 °C for 480 s under forming gas (5% H₂, 95% N₂) atmosphere. The fabrication of the resonators employs electron beam lithography with 400 nm of ZEP-520A as the resist (3.5 krpm). The written pattern is then etched into the Er:SiN_x or SiN_x slab with a CHF₃:O₂ (100 sccm/5 sccm ratio) chemistry dry etch, at 100 mTorr and 150 W forward power (Drytek 4) for 330 s. Finally, suspended PC membranes can be formed by undercutting the oxide layer with a 6:1 buffered oxide etch (20 minutes), and further undercutting of 3 μm of the silicon substrate with a XeF₂ etcher at 1.0 Torr for 30 s.

A.4 GaAs Beam Cavities

The employed membrane structure was grown by molecular beam epitaxy (MBE) and consists of a $1\text{ }\mu\text{m}$ $\text{Al}_{0.8}\text{Ga}_{0.2}\text{As}$ sacrificial layer and a 240 nm GaAs membrane that contains three layers of InAs quantum dots separated by 50 nm GaAs spacers. To achieve emission at $1.3\text{ }\mu\text{m}$, the dots were capped with a 6 nm $\text{In}_{0.15}\text{Ga}_{0.85}\text{As}$ strain-reducing layer. The quantum dots were formed by depositing 2.8 monolayer (ML) of InAs at 510°C using a growth rate of 0.05 ML/s. These growth conditions result in a dot density of $3 \times 10^{10}\text{ cm}^{-2}$, as estimated from atomic force microscopy (AFM) measurements of uncapped quantum dot samples. Fabrication of the PC cavities is done by spinning a 300 nm layer of the electron beam resist ZEP-520A on top of the wafer (5.0 krpm spin), and performing e-beam lithography. The written pattern is then transferred to the GaAs membrane using a $\text{Cl}_2:\text{BCl}_3:\text{Ar}$ (3.0:10.0:15.0 sccm, RF 40 W, forward power 200 W) dry etch. Finally, the nanobeam is undercut with a 7% HF solution in water for 10-20 dips of 1s-2s.

A.5 Si Beam Cavities

A silicon-on-insulator (SOI) wafer with a 160 nm layer of Si and $1\text{ }\mu\text{m}$ thick layer of oxide is used. The cavity is fabricated with electron-beam lithography with a 300 nm layer of ZEP-520A (5.0 krpm) as the resist, and the pattern is transferred into the silicon layer by a $\text{Cl}_2:\text{HBr}$ (20 sccm/15 sccm) plasma dry etch, at 100 mTorr, 200 W forward power, and 30 Gauss magnetic field (Applied Materials P5000 etcher). The oxide sacrificial layer is then etched away by dipping in 6:1 buffered oxide etch (BOE) for 15 minutes to obtain the free standing beams.

A.6 Metallic Gratings on Si-NC layer

The studied structures are fabricated by the following procedure: A 70nm thick layer of Silicon Dioxide (SiO_2 , $n = 1.5$) is grown on polycrystalline quartz by plasma-enhanced chemical vapor deposition (PECVD) with a 14:1 mixture of SiH_4 (diluted

to 2% with N₂) and N₂O at 350°C. The wafer is subsequently annealed in nitrogen at 1100°C to form the Si-NCs. The Si-NC enriched SiO₂ layer has an effective refractive index of $n_{NC} = 1.7$. Then, a 100 nm layer of 2% PMMA (2.0 krpm) is spun on top of the wafer followed by subsequent e-beam lithography to define the grating pattern. Finally, a 30nm layer of gold (Au) is evaporated on top of the PMMA layer with a 3 nm Cr sticking layer and the grating is fabricated by lift-off in acetone.

A.7 Metallic Gratings in MIM Configuration

The structures under study are fabricated by first evaporating an 8 nm Chromium (Cr) sticking layer followed by a 100 nm gold layer on top of an oxidized silicon wafer. The 1 μ m oxidized silicon serves as a diffusion blocking layer beneath the gold. Then, a 52 nm erbium doped amorphous silicon nitride (Er:SiN_x) layer is deposited on top of the gold substrate by N₂ reactive magnetron co-sputtering from Si and Er targets in a Denton Discovery 18 confocal-target sputtering system [43, 44]. The growth is followed by a post annealing process in a rapid thermal annealing furnace at 600°C for 600s under forming gas (5% H₂, 95% N₂) atmosphere. While the optimal annealing temperature to maximize erbium emission efficiency is 1150°C, degradation of the gold substrate at high temperatures restricts the annealing temperature to be below 600°C. The top side grating pattern is then formed by electron beam lithography with a 100 nm layer of PMMA as the resist. Finally, the grating is fabricated by depositing a 3 nm Cr sticking layer followed by a 30 nm layer of Au on top of the patterned resist, and lifting off in acetone.

Appendix B

Finite Difference Time Domain Simulations

The Yee algorithm [148] was first proposed to numerically simulate Maxwell's equation. The basic concept is to discretize Maxwell's curl equations on a spatial grid, and numerically integrate the time evolution using Euler's method. The spatial discretization is shown in Fig. B.1, where each unit cell includes a set of (E_x, E_y, E_z) and (H_x, H_y, H_z) . The E -field components are aligned on the edges of the Yee cube, while the H -fields are aligned perpendicular to the faces of the cube. It can be seen that each E or H is surrounded by 4 components from the H and E fields, respectively, and these surrounding components forms the curl around the appropriate component.

In more detail, assuming non-magnetic media and lossless dielectrics ($\mu = 1$, $\sigma = 0$) the Maxwell curl equations can be written as:

$$\frac{\partial \vec{H}}{\partial t} = -\nabla \times \vec{E}, \quad (\text{B.1})$$

$$\frac{\partial \vec{E}}{\partial t} = \frac{1}{\epsilon(\vec{r})} (\nabla \times \vec{H} - \vec{J}), \quad (\text{B.2})$$

where \vec{E} and \vec{H} are the electric and magnetic fields, $\epsilon(\vec{r})$ is the dielectric structure, and \vec{J} is the current density. We will examine only the x components of the E and H field on the left hand side of the equations, as the other equations can be obtained

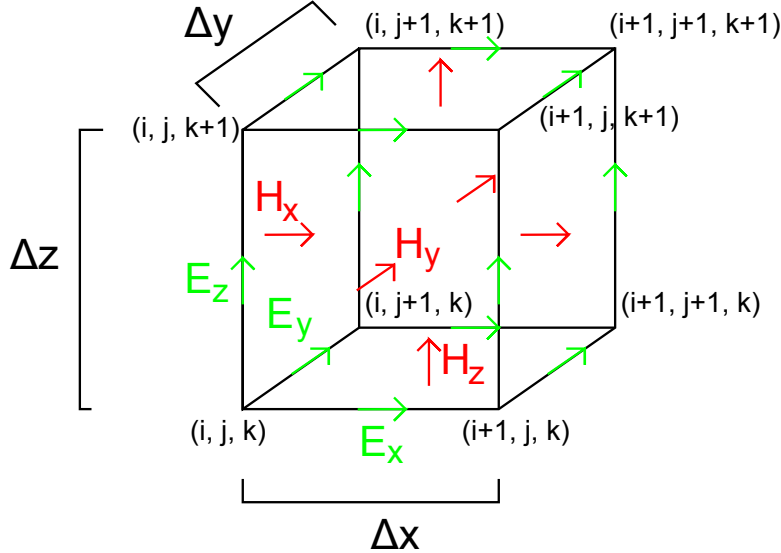


Figure B.1: The FDTD grid from Yee's algorithm. The (i, j, k) label the spatial coordinates of the grid, while the components of the E and H fields are labeled in color arrows.

using a cyclic permutation of (x, y, z) . In particular:

$$\frac{\partial H_x}{\partial t} = - \left(\frac{\partial E_z}{\partial y} - \frac{\partial E_y}{\partial z} \right) \quad (\text{B.3})$$

$$\frac{\partial E_x}{\partial t} = \frac{1}{\epsilon(\vec{r})} \left(\frac{\partial H_z}{\partial y} - \frac{\partial H_y}{\partial z} - \vec{J} \right) \quad (\text{B.4})$$

We then obtain the appropriate components from Fig. B.1, discretize the fields in time and space [i. e. the field F in the \hat{x} direction is enumerated as $F_x(i, j, k, t)$], and evolve in a leapfrog fashion:

$$H_x(i, j, k, t + 1/2) = H_x(i, j, k, t - 1/2) - \left[\frac{E_z(i, j + 1, k, t) - E_z(i, j, k, t)}{\Delta} \right. \\ \left. - \frac{E_y(i, j, k + 1, t) - E_y(i, j, k, t)}{\Delta} \right] \quad (\text{B.5})$$

$$E_x(i, j, k, t + 1) = E_x(i, j, k, t) + \left[\frac{H_z(i, j, k, t) - H_z(i, j - 1, k, t)}{\Delta\epsilon(i, j, k)} \right. \\ \left. - \frac{H_y(i, j, k, t) - H_y(i, j, k - 1, t)}{\Delta\epsilon(i, j, k)} \right] + \frac{\vec{J}}{\epsilon(i, j, k)} \quad (\text{B.6})$$

where we have assumed that the grid is discretized in the same units in the x , y and z directions ($\Delta x = \Delta y = \Delta z = \Delta$). Note that by using the normalized units of $\epsilon_0 = 1$, $\mu_0 = 1$, $\Delta = 1$, and thus $c = 1$, we obtain very simple evolution equations. In order to meet the Courant condition, which ensures that the FDTD simulation converges, we use a time step of $\Delta t = 0.99/\sqrt{3}$ for our simulations.

We may excite modes of the dielectric structure through the current term \vec{J} . By inserting a time dependent current inside the structure at a particular point:

$$\vec{J}(i, j, k, t) = \exp\left[-\frac{(t - t_0)^2}{T^2}\right] \cos(\omega t), \quad (\text{B.7})$$

we excite a frequency bandwidth of $\Delta\omega = \pi/T$ centered around frequency ω . We can excite the structure with a broadband excitation to excite many supported modes, and then selectively excite modes by using excitation with narrow bandwidth. One example of this process is shown in Fig. B.2, when simulating the structure in Fig. 2.7. First, we excite with a broad band pulse, with the time response in Fig. B.2(a), and the frequency response in Fig. B.2(b), which is the Fourier transform of the time response. We note that we are able to initiate a brief pulse [first peak on the left of Fig. B.2(a) for broadband excitation], and have the system evolve afterwards. We find multiple peaks in the frequency response in Fig. B.2(b) that rise above the background, representing the high Q modes of the system, and that there is a broad envelope representing the broadband excitation. We run separate simulations with narrow band excitation to isolate those modes, and the first and second order TE-like modes shown in Fig. 2.7 are found in this manner. The high Q mode (at higher frequency) has extremely slow temporal decay of the field amplitude, and the moderate Q mode (at lower frequency) has visible decay of the field amplitude. We find that the frequency response at the various cavity resonances match the cavity responses from the broadband excitation, but isolated to one cavity frequency. At the end of the narrow band excitation, we obtain the two modes shown in Fig. 2.7.

Finally, we can calculate the Q of the cavities by measuring the time-averaged radiated power from the cavity. The time-averaged power radiated through a surface

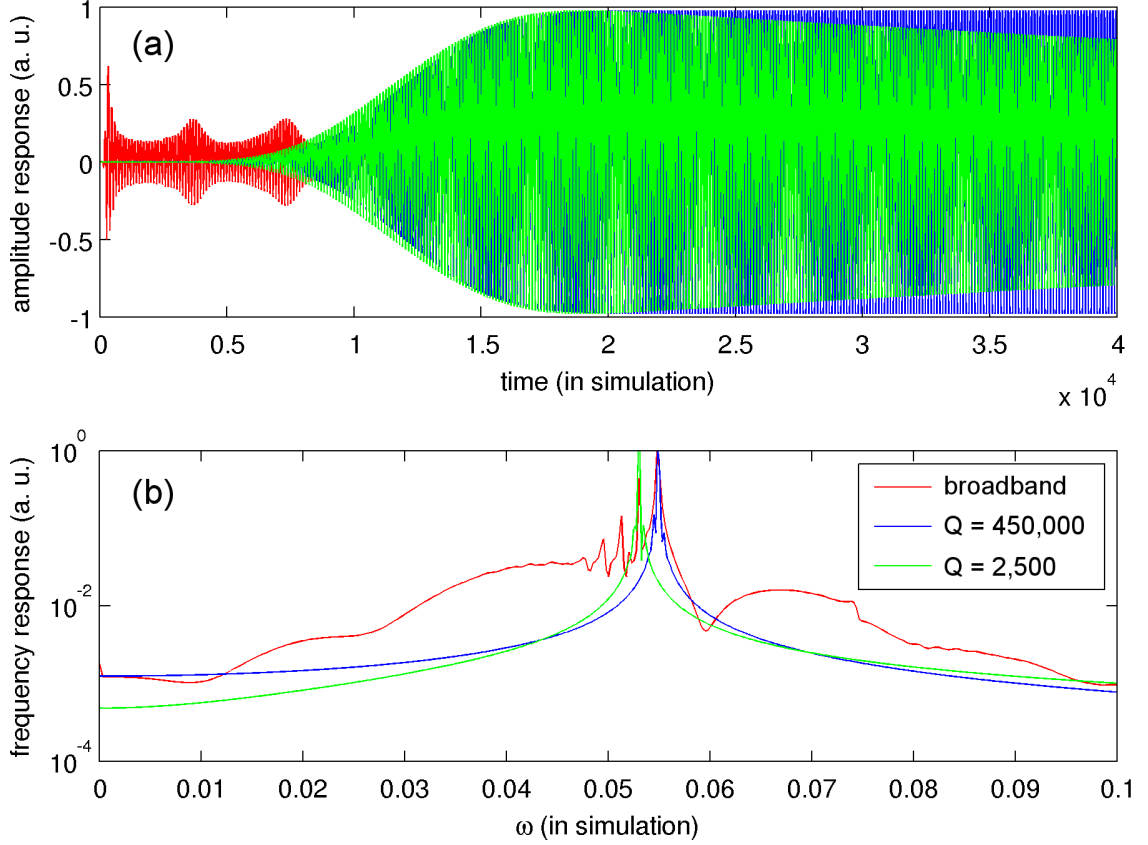


Figure B.2: (a) The time dependent H_z amplitude response of the cavity structure to different excitations. Broadband excitation, along with narrow band excitation for high Q cavity modes are shown. (b) The frequency response to the three excitations shown in part (a), obtained from a Fourier transform relation.

is computed from the spatial integral of the Poynting vector on a surface:

$$\langle P \rangle_T = \left\langle \oint \vec{E} \times \vec{H} \cdot d\vec{A} \right\rangle_T, \quad (\text{B.8})$$

where $d\vec{A}$ is in the surface normal direction, and the averaging takes place over an optical cycle of the cavity mode, $T = 2\pi/\omega$. We use the discretized E and H to calculate the cross product and the Poynting vector. We then calculate the Q -factor using the relation, $Q = \omega U / \langle P \rangle$, where U is the total energy in the cavity structure, and ω is the resonance frequency. In the particular case of the nanobeam cavity,

we define three integrating surfaces to measure radiation in different directions (Fig. B.3). Here, we can see that the Q_{PC} surface captures radiation propagating through the ends of the beams, the $Q_{||}$ surface captures the radiation in the plane of the beam, but out in the y -direction, and the Q_{\perp} surface corresponds to radiation out of the plane of the beam. The total Q is calculated from $Q_{tot} = (Q_{PC}^{-1} + Q_{||}^{-1} + Q_{\perp}^{-1})^{-1}$. With proper placement of the various surfaces, we obtain good match (within 5%) between the Q_{tot} calculated from the radiation method and the Q calculated from the field-decay in the time series when exciting at the cavity resonance [the right hand side of Fig. B.2(a)].

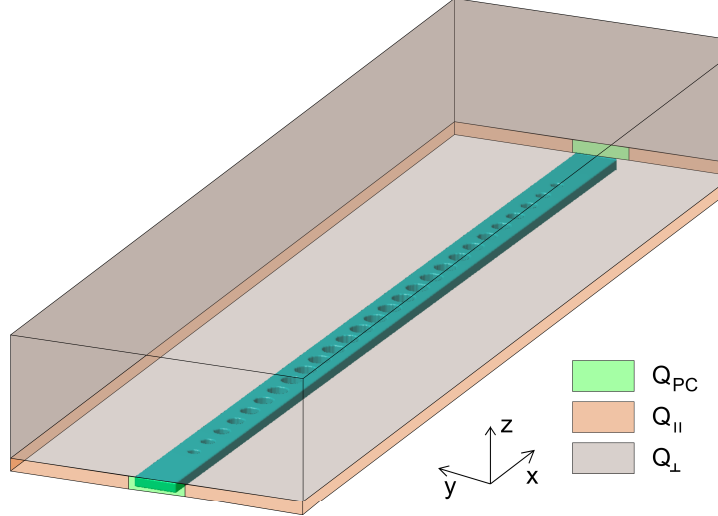


Figure B.3: The nanobeam cavity structure is shown, along with the integrating surfaces for Q_{PC} , $Q_{||}$, and Q_{\perp} . For clarity, the bottom half of surfaces for Q_{\perp} are omitted.

In addition, plasmonic structures can be simulated by including the material conductivity and a frequency dependent current response into Eqn. B.2. Under the

Drude model, which assumes that free electrons collide with ion cores in a memoryless process with a time constant τ_p , the frequency response of the conductivity ($\sigma(\omega)$) is defined with a first order pole as [149]:

$$\vec{J} = \sigma(\omega) \vec{E} = \frac{\epsilon'}{1 + j\omega\tau_p} \vec{E} \quad (\text{B.9})$$

where ϵ' is the amplitude of the dielectric constant associated with the Drude pole. The time constant τ_p is also known as the damping coefficient (η , from Sec. 2.2.1) for a particular metal. As a finite difference equation, the dispersive current can be calculated from the difference equation:

$$\begin{aligned} J_x(i, j, k, t+1) = & \frac{1 - \Delta t/2\tau_p}{1 + \Delta t/2\tau_p} J_x(i, j, k, t+1) \\ & + \frac{\epsilon' \Delta t / \tau_p}{1 + \Delta t/2\tau_p} \left(\frac{E_x(i, j, k, t+1) - E_x(i, j, k, t)}{\Delta t} \right) \end{aligned} \quad (\text{B.10})$$

Appendix C

Optical Setup

The basic optical setup is approximate the same for all of the photoluminescence setups, shown in Fig. C.1.

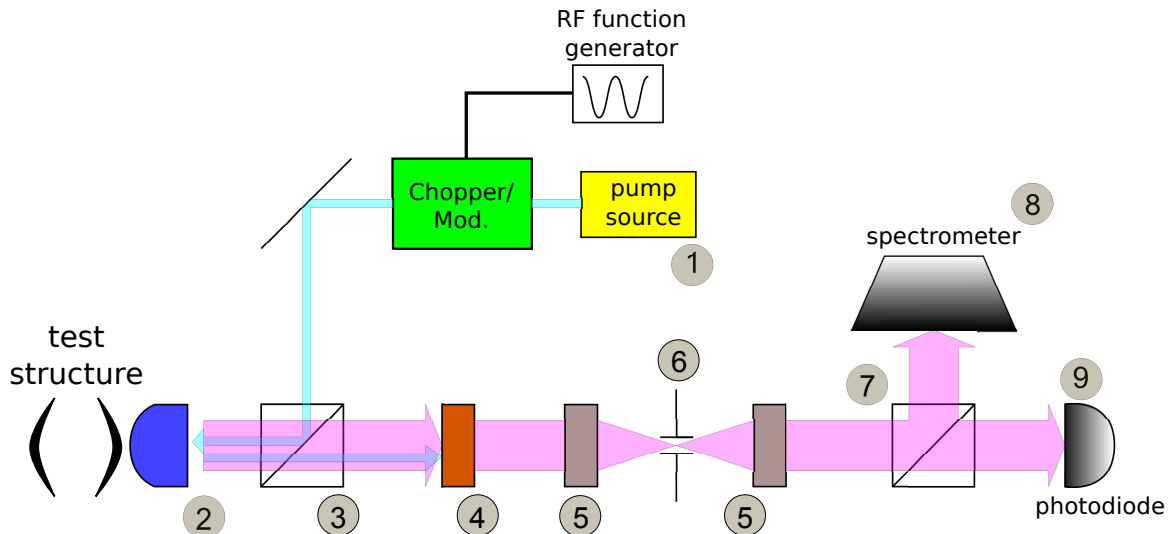


Figure C.1: The optical setup.

The various components in the optical setup is shown below:

number	component	component description
1	Pump sources	doubled Ti:Sapphire (doubled to 400 nm) Thorlabs laser diode LDM405 (405 nm) Qphotonics (980 nm) tunable lasers (Agilent 8164A, Anritsu MG9638A) broadband LED bank (Agilent 83437A Broadband Source)
2	Objective lens	Zeiss 63×, NA = 0.7 (visible) Mitutoyo 100×, NA = 0.5 (infrared)
3	Beam splitter	Thorlabs FM04 Cold mirror (Pump with 400 nm) IR Polarizing beam splitter (Newport 10FC16PB.7)
4	Low pass filter	Varied from 500 nm to 1500 nm
	Waveplate	Half ($\lambda/2$) waveplate
	Polarizer	Glan-Thompson Polarizer
5	Lens telescope	$f = 20$ cm
6	Iris	Adjustable/movable pinhole
7	Beam splitter	Gold mirror IR Polarizing beam splitter (Newport 10FC16PB.7)
8	Spectrometer	for IR :Princeton instruments 750 OMAV 1024 (1024 pixel InGaAs detector, 830 G/mm grating) for visible: Princeton instruments 750 Spec-10:2K (2048×512 pixel Si detector, 1714 G/mm grating)
9	Detectors	New Focus 1811 PIN (125 MHz, Gain = 2.5×10^4) New Focus 1647 APD (1 GHz bandwidth, Gain = 1.0×10^4)

Table C.1: List of optical components.

Appendix D

Theory of Resonant Excitation of a Mechanical Mode through an Optical Cavity Mode

We would like to solve for the mechanical amplitude as a function of the average input power of a modulated laser. We follow the derivation given in Ref. [134] and start with the cavity field equation:

$$\dot{c}(t) = -\left(\frac{\kappa}{2} + i\omega_0\right)c(t) + \frac{i\alpha(t)\omega_0}{L_{OM}}c(t) + \sqrt{\frac{\kappa_e}{2}}s(t)e^{-i\omega t} \quad (\text{D.1})$$

where $s(t)$ is the time-varying pump field, ω_0 is the cavity frequency, κ is the cavity field decay rate, κ_e is the external coupling rate, L_{OM} is the optomechanical coupling, $c(t)$ is the cavity field, and $\alpha(t)$ is the mechanical mode amplitude. In this case, we are inputting a laser at ω which is detuned from the optical cavity mode center frequency, and the input is modulated periodically with frequency Ω , which is detuned from the mechanical mode center frequency Ω_0 .

We assume sinusoidal mechanical motion, such that the beam also moves with modulation frequency Ω :

$$\alpha(t) = \alpha_0 \sin(\Omega t) \quad (\text{D.2})$$

Note that Ω could be different from Ω_0 , but since we're driving the motion, we can

assume the mechanical mode responds with the same frequency. Then the equation becomes:

$$\dot{c}(t) = -\left(\frac{\kappa}{2} + i\omega_0\right)c(t) + \frac{i\omega_0\alpha_0 \sin(\Omega t)}{L_{OM}}c(t) + \sqrt{\frac{\kappa_e}{2}}s(t)e^{-i\omega t} \quad (\text{D.3})$$

The homogeneous solution is:

$$c_h(t) = C_0 \exp\left(-\left(\frac{\kappa}{2} + i\omega_0\right)t\right) \sum_n (-i)^n J_n(\beta) e^{in\Omega t} \quad (\text{D.4})$$

with $\beta = \omega_0\alpha_0/L_{OM}\Omega$, and the inhomogeneous solution is:

$$c_p(t) = \int u \sqrt{\frac{\kappa_e}{2}} s(t) e^{-i\omega t} = \int e^{(\frac{\kappa}{2} + i\omega_0)t} \sum_n i^n J_n(\beta) e^{in\Omega t} \sqrt{\frac{\kappa_e}{2}} s(t) e^{-i\omega t} \quad (\text{D.5})$$

Since our pump is modulated with frequency Ω , we express the input as a Fourier Series with $s(t) = \sum_k a_k e^{ik\Omega t}$:

$$\begin{aligned} c_p(t) &= \int e^{(\frac{\kappa}{2} + i\omega_0)t} \sum_n i^n J_n(\beta) e^{in\Omega t} \sqrt{\frac{\kappa_e}{2}} \sum_k a_k e^{ik\Omega t} e^{-i\omega t} dt \\ &= \sum_{n,k} i^n J_n(\beta) a_k \sqrt{\frac{\kappa_e}{2}} \int e^{(\frac{\kappa}{2} + i(\omega_0 - \omega) + i(n+k)\Omega)t} dt \\ &= \sum_{n,k} \frac{i^n J_n(\beta) a_k}{\frac{\kappa}{2} - i\Delta + i(n+k)\Omega} e^{(\frac{\kappa}{2} - i\Delta + i(n+k)\Omega)t} \end{aligned} \quad (\text{D.6})$$

where we have performed the integration with $\Delta = \omega - \omega_0$, and neglected the $\sqrt{\kappa_e/2}$ term as normalization.

Note that the full particular solution is then:

$$c_p(t) = \sum_{n,k} \frac{i^n J_n(\beta) a_k}{\frac{\kappa}{2} - i\Delta + i(n+k)\Omega} e^{(-i\Delta + i(n+k)\Omega - i\omega_0)t - i\beta \cos(\Omega t))} \quad (\text{D.7})$$

Because the homogeneous solution levels out with rate κ and this is fast, the

particular solution is the steady state solution. The optical force is:

$$\frac{|c_p(t)|^2}{L_{OM}} = \sum_{n,k,m,l} \frac{i^{n-m} J_n(\beta) J_m(\beta) a_k a_l^* / L_{OM}}{(\frac{\kappa}{2} - i\Delta + i(n+k)\Omega)(\frac{\kappa}{2} + i\Delta - i(m+l)\Omega)} e^{i[(n+k)-(m+l)]\Omega t} \quad (\text{D.8})$$

If we assume that $\beta \ll 1$ so that $J_1(\beta) \approx \beta$, we can take only the zeroth order in $J_0(\beta)$:

$$\frac{|c_p(t)|^2}{L_{OM}} = \frac{1}{L_{OM}} \sum_{k,l} \frac{J_0^2(\beta) a_k a_l^*}{(\frac{\kappa}{2} - i\Delta + ik\Omega)(\frac{\kappa}{2} + i\Delta - il\Omega)} e^{i(k-l)\Omega t} \quad (\text{D.9})$$

D.1 Example 1: Cosine input

Let's input $s(t) = s_0(1 + \cos(\Omega t))/2$:

$$s(t) = s_0 \left(\frac{1}{2} + \frac{1}{4} e^{i\Omega t} + \frac{1}{4} e^{-i\Omega t} \right) \quad (\text{D.10})$$

Thus we have $a_0 = 1/2$, $a_1 = a_{-1} = 1/4$.

The normalization for the time dependent portion of the input is $A^2 \int |s(t)|^2 = A^2 \int (1 + \cos(\Omega t))^2/4 = A^2(3\pi)/(4\Omega)$. We want to keep the average power the same, so $A^2(3\pi)/(4\Omega)/T = 1 = A^2(3\pi)/(4\Omega)/(2\pi/\Omega)$, or $A = \sqrt{8/3}$.

The optical force, normalized to the average input power is then:

$$\frac{F}{|s_0|^2 \kappa_e A^2} = \frac{J_0^2(\beta)}{L_{OM}} \sum_{k,l} \frac{a_k a_l^*}{(\frac{\kappa}{2} - i\Delta + ik\Omega)(\frac{\kappa}{2} + i\Delta - il\Omega)} e^{i(k-l)\Omega t} \quad (\text{D.11})$$

We will only consider the elements with frequency Ω , as they will contribute to work getting done on the mechanical mode:

$$\begin{aligned} \frac{F}{|s_0|^2 \kappa_e A^2} &= \frac{J_0^2(\beta)}{8L_{OM}} 2 \left[\frac{(\frac{\kappa^2}{4} + \Delta(\Delta - \Omega)) \cos(\Omega t) + \frac{\Delta\Omega}{2} \sin(\Omega t)}{(\frac{\kappa^2}{4} + \Delta^2)(\frac{\kappa^2}{4} + (\Delta - \Omega)^2)} \right] \\ &\quad + \frac{J_0^2(\beta)}{8L_{OM}} 2 \left[\frac{(\frac{\kappa^2}{4} + \Delta(\Delta + \Omega)) \cos(\Omega t) + \frac{\Delta\Omega}{2} \sin(\Omega t)}{(\frac{\kappa^2}{4} + \Delta^2)(\frac{\kappa^2}{4} + (\Delta + \Omega)^2)} \right] \end{aligned} \quad (\text{D.12})$$

Since only the force in quadrature with the motion of beam does work on the

beam, we isolate the cosine term:

$$\frac{F}{|s_0|^2 \kappa_e A^2} = \frac{J_0^2(\beta)}{4L_{OM}} \cos(\Omega t) \left[\frac{1}{\frac{\kappa^2}{4} + (\Delta - \Omega)^2} + \frac{1}{\frac{\kappa^2}{4} + (\Delta + \Omega)^2} - \frac{\Delta \Omega}{(\frac{\kappa^2}{4} + \Delta^2)(\frac{\kappa^2}{4} + (\Delta - \Omega)^2)} + \frac{\Delta \Omega}{(\frac{\kappa^2}{4} + \Delta^2)(\frac{\kappa^2}{4} + (\Delta + \Omega)^2)} \right] \quad (\text{D.13})$$

Note that this force is maximized near $\Delta = 0$ (as all four terms are near Lorentzian functions in terms of Δ), and we consider the force amplitude (dropping the harmonic variation):

$$\frac{F}{|s_0|^2 \kappa_e A^2} = \frac{J_0^2(\beta)}{2L_{OM}} \left[\frac{1}{\frac{\kappa^2}{4} + \Omega^2} \right] \approx \frac{1}{2L_{OM}} \left[\frac{1}{\frac{\kappa^2}{4} + \Omega^2} \right] \quad (\text{D.14})$$

or with the normalization (such that power input is proportional to $|s|^2$):

$$\frac{F}{|s_0|^2 \kappa_e} = \frac{8}{3} \frac{1}{2L_{OM}} \frac{1}{\frac{\kappa^2}{4} + \Omega^2} \quad (\text{D.15})$$

We note that in the case pumping with a CW laser, the equivalent force is [134]:

$$\frac{F}{|s_0|^2 \kappa_e} = \frac{\beta}{2L_{OM}} \left[\frac{4\kappa\Delta\Omega^2}{(\frac{\kappa^2}{4} + \Delta^2)(\frac{\kappa^2}{4} + (\Delta - \Omega)^2)(\frac{\kappa^2}{4} + (\Delta + \Omega)^2)} \right] \quad (\text{D.16})$$

Thus, comparing some sort of AC pump scheme (assuming $\Delta = 0$, to maximize force) to the DC pumping (assuming $\Delta = \kappa/2$, where the force is approximately maximized), we see that the transferred power should be approximately $\kappa^2/(\beta\Omega^2)$ more efficient. In addition, if we assume that our in-coupling efficiency is sufficiently high, then we would have $\kappa_e \sim \kappa$. Using the above two equations, our optical force is $\propto \kappa^{-2}$ for the CW case, and $\propto \kappa^{-1}$ for the modulated laser case.

Note that our thermal amplitude is $\langle x^2 \rangle = k_b T / m_{\text{eff}} \Omega^2$, and $|\langle x \rangle| \approx 10 \text{ pm}$ in this case, which places us in the high β regime (despite the sidebands being unresolved, we have $\beta = 45$). We can calculate the force as a function of β as well, plotted in Fig. D.1, using real parameters of $m_{\text{eff}} = 2 \times 10^{-15} \text{ kg}$, $\Omega_0 = 2\pi \cdot 22 \times 10^6 \text{ Hz}$, $Q_m = 70$, $\kappa_e = \kappa/2$, $L_{OM} = 2 \mu\text{m}$, and optical wavelength $\lambda = 1500 \text{ nm}$, and optical $Q = 2 \times 10^4$. We plot the kernel of the force term using Eqn. D.8 for different β , but

fixing all other parameters, and plot the results in Fig. D.1. We notice that for our parameters, the force on the beam is relatively unchanged even up to $\beta \approx 100$. Thus, we are able to use sinusoidal pump to increase the force amplitude.

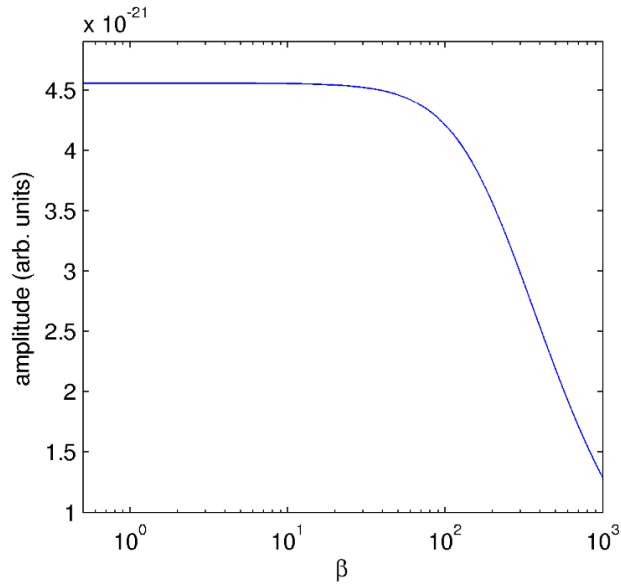


Figure D.1: The theoretical average force on the mechanical mode for a fixed average input power of the modulated input, as a function of β .

Bibliography

- [1] D. A. B. Miller. Device Requirements for Optical Interconnects to Silicon Chips. *Proceedings of the IEEE*, 97(7, Sp. Iss. SI):1166–1185, JUL 2009.
- [2] D. Liang, A. W. Fang, H. Park, T. E. Reynolds, K. Warner, D. C. Oakley, and J. E. Bowers. Low-temperature, strong SiO₂-SiO₂ covalent wafer bonding for III-V compound semiconductors-to-silicon photonic integrated circuits. *Journal of Electronic Materials*, 37(10):1552–1559, OCT 2008.
- [3] Z. Mi, J. Yang, P. Bhattacharya, G. Qin, and Z. Ma. High-performance quantum dot lasers and integrated optoelectronics on si. *Proceedings of the IEEE*, 97(7):1239 –1249, JUL 2009.
- [4] K. J. Vahala. Optical microcavities. *Nature*, 424(6950):839–846, 14 AUG 2003.
- [5] E. M. Purcell. Spontaneous Emission Probabilities at Radio Frequencies. *Physical Review*, 69(11-1):681, 1946.
- [6] M. Scully and M. S. Zubairy. *Quantum Optics*. Cambridge University Press, Cambridge, 1997.
- [7] H. Altug, D. Englund, and J. Vuckovic. Ultrafast photonic crystal nanocavity laser. *Nature Physics*, 2(7):484–488, JUL 2006.
- [8] D. Englund, H. Altug, I. Fushman, and J. Vuckovic. Efficient terahertz room-temperature photonic crystal nanocavity laser. *Applied Physics Letters*, 91(7):071126, 13 AUG 2007.

- [9] E. Yablonovitch. Inhibited Spontaneous Emission in Solid-State Physics and Electronics. *Physical Review Letters*, 58(20):2059–2062, 18 MAY 1987.
- [10] S. John. Strong Localization of Photonics in Certain Disordered Dielectric Superlattices. *Physical Review Letters*, 58(23):2486–2489, 8 JUN 1987.
- [11] J. N. Winn J. D. Joannopoulos, R. D. Meade. *Photonic Crystals: Molding the Flow of Light*. Princeton University Press, Princeton, 1995.
- [12] S. Y. Lin, J. G. Fleming, D. L. Hetherington, B. K. Smith, R. Biswas, K. M. Ho, M. M. Sigalas, W. Zubrzycki, S. R. Kurtz, and J. Bur. A three-dimensional photonic crystal operating at infrared wavelengths. *Nature*, 394(6690):251–253, 16 JUL 1998.
- [13] P. Lodahl, A. F. van Driel, I. S. Nikolaev, A. Irman, K. Overgaag, D. L. Vanmaekelbergh, and W. L. Vos. Controlling the dynamics of spontaneous emission from quantum dots by photonic crystals. *Nature*, 430(7000):654–657, 5 AUG 2004.
- [14] Q. Minghao, E. Lidorikis, P.T. Rakich, S.G. Johnson, J. Joannopoulos, E.P. Ip- pen, and H.I. Smith. A three-dimensional optical photonic crystal with designed point defects. *Nature*, 429(6991):538–42, 3 JUN 2004.
- [15] K. Aoki, D. Guimard, M. Nishioka, M. Nomura, S. Iwamoto, and Y. Arakawa. Coupling of quantum-dot light emission with a three-dimensional photonic-crystal nanocavity. *Nature Photonics*, 2(11):688–692, NOV 2008.
- [16] S. Takahashi, K. Suzuki, M. Okano, M. Imada, T. Nakamori, Y. Ota, K. I. Susumu, and S. Noda. Direct creation of three-dimensional photonic crystals by a top-down approach. *Nature Materials*, 8(9):721–725, SEP 2009.
- [17] J. L. Jewell, J. P. Harbison, A. Scherer, Y. H. Lee, and L. T. Florez. Vertical-cavity surface-emitting lasers - Design, growth, fabrication, characterization. *IEEE Journal of Quantum Electronics*, 27(6):1332–1346, JUN 1991.

- [18] B.-S. Song, S. Noda, T. Asano, and Y. Akahane. Ultra-high-Q photonic double-heterostructure nanocavity. *Nature Materials*, 4(3):207–10, MAR 2005.
- [19] D. Englund, I. Fushman, and J. Vuckovic. General recipe for designing photonic crystal cavities. *Optics Express*, 13(16):5961–5975, 8 AUG 2005.
- [20] H. Raether. *Surface Plasmons on Smooth and Rough Surfaces and on Gratings (Springer Tracts in Modern Physics)*. Springer, DEC 1988.
- [21] M. P. vanExter, G. Nienhuis, and J. P. Woerdman. Two simple expressions for the spontaneous emission factor beta. *Physical Review A*, 54(4):3553–3558, OCT 1996.
- [22] E. Desurvire. *Erbium-doped fiber amplifiers: principles and applications*, pages 230 – 298. Wiley & Sons, New York, 1994.
- [23] A. Neogi, C.-W. Lee, H. O. Everitt, T. Kuroda, A. Tackeuchi, and E. Yablonovitch. Enhancement of spontaneous recombination rate in a quantum well by resonant surface plasmon coupling. *Physical Review B*, 66(15):153305, OCT 2002.
- [24] K. Okamoto, I. Niki, A. Shvartser, Y. Narukawa, T. Mukai, and A. Scherer. Surface-plasmon-enhanced light emitters based on InGaN quantum wells. *Nature Materials*, 3(9):601–605, SEP 2004.
- [25] K. Okamoto, S. Vyawahare, and A. Scherer. Surface-plasmon enhanced bright emission from CdSe quantum-dot nanocrystals. *Journal of the Optical Society of America B - Optical Physics*, 23(8):1674–1678, AUG 2006.
- [26] K.-C. Shen, C.-Y. Chen, C.-F. Huang, J.-Y. Wang, Y.-C. Lu, Y.-W. Kiang, C. C. Yang, and Y.-J. Yang. Polarization dependent coupling of surface plasmon on a one-dimensional Ag grating with an InGaN/GaN dual-quantum-well structure. *Applied Physics Letters*, 92(1):013108–1–3, 7 JAN 2008.

- [27] Y.-J. Hung, I. I. Smolyaninov, C. C. Davis, and H.-C. Wu. Fluorescence enhancement by surface gratings. *Optics Express*, 14(22):10825–10830, 30 OCT 2006.
- [28] N.-F. Chiu, C.-W. Lin, J.-H. Lee, C.-H. Kuan, K.-C. Wu, and C.-K. Lee. Enhanced luminescence of organic/metal nanostructure for grating coupler active long-range surface plasmonic device. *Applied Physics Letters*, 91(8):083114–1–3, 20 AUG 2007.
- [29] J. Vuckovic, M. Loncar, and A. Scherer. Surface plasmon enhanced light-emitting diode. *IEEE Journal of Quantum Electronics*, 36(10):1131–1144, OCT 2000.
- [30] D. E. Chang, A. S. Sørensen, P. R. Hemmer, and M. D. Lukin. Quantum optics with surface plasmons. *Physica Review Letters*, 97(5):053002, AUG 2006.
- [31] A. V. Akimov, A. Mukherjee, C. L. Yu, D. E. Chang, A. S. Zibrov, P. R. Hemmer, H. Park, and M. D. Lukin. Generation of single optical plasmons in metallic nanowires coupled to quantum dots. *Nature*, 450(7168):402–406, 15 NOV 2007.
- [32] R. F. Oulton, V. J. Sorger, D. A. Genov, D. F. P. Pile, and X. Zhang. A hybrid plasmonic waveguide for subwavelength confinement and long-range propagation. *Nature Photonics*, 2(8):496–500, AUG 2008.
- [33] R. F. Oulton, V. J. Sorger, T. Zentgraf, R.-M. Ma, C. Gladden, L. Dai, G. Bartal, and X. Zhang. Plasmon lasers at deep subwavelength scale. *Nature*, 461(7264):629–632, 1 OCT 2009.
- [34] W. A. Saunders, P. C. Sercel, R. B. Lee, Atwater H. A., K. J. Vahala, R. C Flagan, and E. J. Escorciaoaparcio. Synthesis of Luminescent Silicon Clusters by Spark Ablation. *Applied Physics Letters*, 63(11):1549–1551, 13 SEP 1993.
- [35] J. G. Zhu, C. W. White, J. D. Budai, S. P. Withrow, and Y. Chen. Growth of Ge, Si, and SiGe Nanocrystals in SiO₂ Matrices. *Journal of Applied Physics*, 78(7):4386–4389, 1 OCT 1995.

- [36] L. Pavesi, L. Dal Negro, C. Mazzoleni, G. Franzo, and F. Priolo. Optical gain in silicon nanocrystals. *Nature*, 408(6811):440–444, 23 NOV 2000.
- [37] L. Pavesi, S. Gaponenko, and L. Dal Negro, editor. *Towards the First Silicon Laser*. Kluwer Academic Publishers, Netherlands, 2003.
- [38] J. P. Wilcoxon and G. A. Samara. Tailorable, visible light emission from silicon nanocrystals. *Applied Physics Letters*, 74(21):3164–3166, 24 MAY 1999.
- [39] G. Ledoux, O. Guillois, D. Porterat, C. Reynaud, F. Huisken, B. Kohn, and V. Paillard. Photoluminescence properties of silicon nanocrystals as a function of their size. *Physical Review B*, 62(23):15942–15951, 15 DEC 2000.
- [40] R. J. Walters, G. I. Bourianoff, and H. A. Atwater. Field-effect electroluminescence in silicon nanocrystals. *Nature Materials*, 4(2):143–146, FEB 2005.
- [41] A. J. Kenyon, C. E. Chryssou, C. W. Pitt, T. Shimizu-Iwayama, D. E. Hole, N. Sharma, and C. J. Humphreys. Luminescence from erbium-doped silicon nanocrystals in silica: Excitation mechanisms. *Journal of Applied Physics*, 91(1):367–374, 1 JAN 2002.
- [42] J. Heitmann, M. Schmidt, M. Zacharias, V. Y. Timoshenko, M. G. Lisachenko, and P. K. Kashkarov. Fabrication and photoluminescence properties of erbium doped size-controlled silicon nanocrystals. *Materials Science and Engineering B: Solid State Materials for Advanced Technology*, 105(1-3):214–220, 15 DEC 2003.
- [43] S. Yerci, R. Li, S. O. Kucheyev, T. van Buuren, S. N. Basu, and L. Dal Negro. Energy transfer and 1.54 μ m emission in amorphous silicon nitride films. *Applied Physics Letters*, 95(3):031107 (3 pp.), 20 JUL 2009.
- [44] R. Li, S. Yerci, and L. Dal Negro. Temperature dependence of the energy transfer from amorphous silicon nitride to Er ions. *Applied Physics Letters*, 95(4):041111 (3 pp.), 27 JUL 2009.

- [45] W. C. Ding, D. Hu, J. Zheng, P. Chen, B. W. Cheng, J. Z. Yu, and Q. M. Wang. Strong visible and infrared photoluminescence from Er-implanted silicon nitride films. *Journal of Physics D: Applied Physics*, 41(13):135101 (4 pp.), 7 JUL 2008.
- [46] L. Dal Negro, R. Li, J. Warga, S. Yerci, S. Basu, S. Hamel, and G. Galli. *Silicon Nanophotonics: Basic Principles, Present Status and Perspectives*, edited by L. Khriachtchev, chapter Light-emission from silicon-rich nitride nanostructures. World Scientific, Singapore, 2008.
- [47] R. Li, J. R. Schneck, J. Warga, L. D. Ziegler, and L. Dal Negro. Carrier dynamics and erbium sensitization in silicon-rich nitride nanocrystals. *Applied Physics Letters*, 93(9):091119 (3 pp.), 1 SEP 2008.
- [48] L. Dal Negro, R. Li, J. Warga, and S. N. Basu. Sensitized erbium emission from silicon-rich nitride/silicon superlattice structures. *Applied Physics Letters*, 92(18):181105–1–3, 5 MAY 2008.
- [49] J. Warga, R. Li, S.N. Basu, and L. Dal Negro. Electroluminescence from silicon-rich nitride/silicon superlattice structures. *Applied Physics Letters*, 93(15):151116 (3 pp.), 13 OCT 2008.
- [50] S. Yerci, R. Li, and L. Dal Negro. Electroluminescence from Er-doped Si-rich silicon nitride light emitting diodes. *Applied Physics Letters*, 97(8):081109 (3 pp.), 23 AUG 2010.
- [51] Peter Michler, editor. *Single Quantum Dots: Fundamentals, Applications and New Concepts*. Springer-Verlag: Topics in Applied Physics, Berlin, 2003.
- [52] B. Ellis, I. Fushman, D. Englund, B. Zhang, Y. Yamamoto, and J. Vuckovic. Dynamics of quantum dot photonic crystal lasers. *Applied Physics Letters*, 90(15):151102–1–3, 9 APR 2007.
- [53] S. Strauf, K. Hennessy, M. T. Rakher, Y.-S. Choi, A. Badolato, L. C. Andreani, E. L. Hu, P. M. Petroff, and D. Bouwmeester. Self-tuned quantum dot gain in

- photonic crystal lasers. *Physical Review Letters*, 96(12):127404/1–4, 31 MAR 2006.
- [54] M. Nomura, S. Iwamoto, K. Watanabe, N. Kumagai, Y. Nakata, S. Ishida, and Y. Arakawa. Room temperature continuous-wave lasing in photonic crystal nanocavity. *Optics Express*, 14(13):6308–6315, 26 JUN 2006.
- [55] M. Nomura, S. Iwamoto, N. Kumagai, and Y. Arakawa. Temporal coherence of a photonic crystal nanocavity laser with high spontaneous emission coupling factor. *Physical Review B*, 75(19):195313, MAY 2007.
- [56] M. Nomura, N. Kumagai, S. Iwamoto, Y. Ota, and Y. Arakawa. Photonic crystal nanocavity laser with a single quantum dot gain. *Optics Express*, 17(18):15975–15982, 31 AUG 2009.
- [57] D. Englund, D. Fattal, E. Waks, G. Solomon, B. Zhang, T. Nakaoka, Y. Arakawa, Y. Yamamoto, and Jelena Vuckovic. Controlling the spontaneous emission rate of single quantum dots in a two-dimensional photonic crystal. *Phys. Rev. Lett.*, 95(1):013904, JUL 2005.
- [58] D. Englund, A. Faraon, I. Fushman, N. Stoltz, P. Petroff, and J. Vuckovic. Controlling cavity reflectivity with a single quantum dot. *Nature*, 471:857–61, 6 DEC 2007.
- [59] M. Notomi, T. Tanabe, A. Shinya, E. Kuramochi, H. Taniyama, S. Mitsugi, and M. Morita. Nonlinear and adiabatic control of high-q photonic crystal nanocavities. *Optics Express*, 15(26):17458–17481, 2007.
- [60] Y. Takahashi, H. Hagino, Y. Tanaka, B.-S. Song, T. Asano, and S. Noda. High-Q nanocavity with a 2-ns photon lifetime. *Optics Express*, 15(25):17206–17213, 10 DEC 2007.
- [61] C. F. Wang, R. Hanson, D. D. Awschalom, E. L. Hu, T. Feygelson, J. Yang, and J. E. Butler. Fabrication and characterization of two-dimensional photonic crystal microcavities in nanocrystalline diamond. *Applied Physics Letters*, 91(20):201112–1–3, 12 NOV 2007.

- [62] C. Kreuzer, J. Riedrich-Moeller, E. Neu, and C. Becher. Design of photonic crystal microcavities in diamond films. *Optics Express*, 16(3):1632–1644, 4 FEB 2008.
- [63] M. Barth, N. Nuesse, J. Stingl, B. Loechel, and O. Benson. Emission properties of high-Q silicon nitride photonic crystal heterostructure cavities. *Applied Physics Letters*, 93(2):021112, 14 JUL 2008.
- [64] M. Makarova, J. Vuckovic, H. Sanda, and Y. Nishi. Silicon-based photonic crystal nanocavity light emitters. *Applied Physics Letters*, 89(22):221101, 27 NOV 2006.
- [65] J. S. Foresi, P. R. Villeneuve, J. Ferrera, E. R. Thoen, G. Steinmeyer, S. Fan, J. D. Joannopoulos, L. C. Kimerling, H. I. Smith, and E. P. Ippen. Photonic-bandgap microcavities in optical waveguides. *Nature*, 390(6656):143–145, 13 NOV 1997.
- [66] P. B. Deotare, M. W. McCutcheon, I. W. Frank, M. Khan, and M. Loncar. High quality factor photonic crystal nanobeam cavities. *Applied Physics Letters*, 94(12):121106, 23 MAR 2009.
- [67] M. Eichenfield, R. Camacho, J. Chan, K. J. Vahala, and O. Painter. A picogram- and nanometre-scale photonic-crystal optomechanical cavity. *Nature*, 459(7246):550–U79, 28 MAY 2009.
- [68] M. W. McCutcheon and M. Loncar. Design of a silicon nitride photonic crystal nanocavity with a quality factor of one million for coupling to a diamond nanocrystal. *Optics Express*, 16(23):19136–19145, 2008.
- [69] Y. Gong and J. Vuckovic. Photonic crystal cavities in silicon dioxide. *Applied Physics Letters*, 96(3):031107, 18 JAN 2010.
- [70] M. Notomi, E. Kuramochi, and H. Taniyama. Ultrahigh-Q nanocavity with 1D photonic gap. *Optics Express*, 16(15):11095–11102, 21 JUL 2008.

- [71] J. Chan, M. Eichenfield, R. Camacho, and O. Painter. Optical and mechanical design of a “zipper” photonic crystal optomechanical cavity. *Optics Express*, 17(5):3802–3817, 2 MAR 2009.
- [72] R. D. Kekatpure and M. L. Brongersma. Fundamental photophysics and optical loss processes in Si-nanocrystal-doped microdisk resonators. *Physical Review A*, 78(2, Part B):023829, AUG 2008.
- [73] D. K. Armani, T. J. Kippenberg, S. M. Spillane, and K. J. Vahala. Ultra-high-Q toroid microcavity on a chip. *Nature*, 421(6926):925–928, 27 FEB 2003.
- [74] J. Goh, I. Fushman, D. Englund, and J. Vuckovic. Genetic optimization of photonic bandgap structures. *Optics Express*, 15(13):8218–8230, 25 JUN 2007.
- [75] J. Lu and J. Vuckovic. Inverse design of nanophotonic structures using complementary convex optimization. *Optics Express*, 18(4):3793–3804, 2010.
- [76] Q. Quan, P. B. Deotare, and M. Loncar. Photonic crystal nanobeam cavity strongly coupled to the feeding waveguide. *Applied Physics Letters*, 96(20):203102, 17 MAY 2010.
- [77] J.-C. Weeber, Y. Lacroute, A. Dereux, E. Devaux, T. Ebbesen, C. Girard, M. González, and A.-L. Baudrion. Near-field characterization of bragg mirrors engraved in surface plasmon waveguides. *Physical Review B*, 70(23):235406, DEC 2004.
- [78] S. I. Bozhevolnyi, A. Boltasseva, T. Sondergaard, T. Nikolajsen, and K. Leosson. Photonic bandgap structures for long-range surface plasmon polaritons. *Optics Communications*, 250(4-6):328–333, 15 JUN 2005.
- [79] Z. W. Liu, Q. H. Wei, and X. Zhang. Surface plasmon interference nanolithography. *Nano Letters*, 5(5):957–961, MAY 2005.
- [80] B. Wang and G. P. Wang. Plasmon Bragg reflectors and nanocavities on flat metallic surfaces. *Applied Physics Letters*, 87(1):013107, 4 JUL 2005.

- [81] A. Karalis, E. Lidorikis, M. Ibanescu, J. D. Joannopoulos, and M. Soljacic. Surface-plasmon-assisted guiding of broadband slow and subwavelength light in air. *Physical Review Letters*, 95(6):063901, AUG 5 2005.
- [82] E. M. Lifshitz, L. D. Landau, and L. P. Pitaevskii. *Electrodynamics of Continuous Media*. Butterworth-Heinemann, 2 edition, JAN 1984.
- [83] P. G. Eliseev, H. Li, A. Stintz, G. T. Liu, T. C. Newell, K. J. Malloy, and L. F. Lester. Transition dipole moment of InAs/InGaAs quantum dots from experiments on ultralow-threshold laser diodes. *Applied Physics Letters*, 77(2):262–264, 10 JUL 2000.
- [84] E. Waks and J. Vuckovic. Dispersive properties and large kerr nonlinearities using dipole-induced transparency in a single-sided cavity. *Physical Review A*, 73(4):041803, APR 2006.
- [85] Matula, R. A. Electrical Resistivity of Copper, Gold, Palladium, and Silver. *Journal of Physical and Chemical Reference Data*, 8(4):1147–1298, 1979.
- [86] Y. Gong and J. Vuckovic. Design of plasmon cavities for solid-state cavity quantum electrodynamics applications. *Applied Physics Letters*, 90(3):33113–1–3, 15 JAN 2007.
- [87] H. Iwase, D. Englund, and J. Vuckovic. Analysis of the Purcell effect in photonic and plasmonic crystals with losses. *Optics Express*, 18(16):16546–16560, 2 AUG 2010.
- [88] V. S. C. Manga and S. Hughes. Single quantum-dot Purcell factor and beta factor in a photonic crystal waveguide. *Physical Review B*, 75(20):205437–1–7, 15 MAY 2007.
- [89] H. T. Miyazaki and Y. Kurokawa. Squeezing visible light waves into a 3-nm-thick and 55-nm-long plasmon cavity. *Physical Review Letters*, 96(9):097401/1–4, 10 MAR 2006.

- [90] Y. C. Jun, R. D. Kekatpure, J. S. White, and M. L. Brongersma. Nonresonant enhancement of spontaneous emission in metal-dielectric-metal plasmon waveguide structures. *Physical Review B*, 78(15):153111M (4 pp.), 15 OCT 2008.
- [91] Y. Kurokawa and H. T. Miyazaki. Metal-insulator-metal plasmon nanocavities: analysis of optical properties. *Physical Review B*, 75(3):35411–1–13, 15 JAN 2007.
- [92] Y. Gong, J. Lu, S.-L. Cheng, Y. Nishi, and J. Vuckovic. Plasmonic enhancement of emission from Si-nanocrystals. *Applied Physics Letters*, 94(1):013106 (3 pp.), 5 JAN 2009.
- [93] R. D. Kekatpure and M. L. Brongersma. Quantification of Free-Carrier Absorption in Silicon Nanocrystals with an Optical Microcavity. *Nano Letters*, 8(11):3787–3793, NOV 2008.
- [94] P. Bianucci, X. Wang, J. G. C. Veinot, and A. Meldrum. Silicon nanocrystals on bottle resonators: Mode structure, loss mechanisms and emission dynamics. *Optics Express*, 18(8):8466–8481, 12 APR 2010.
- [95] H. Rinnert, O. Jambois, and M. Vergnat. Photoluminescence properties of size-controlled silicon nanocrystals at low temperatures. *Journal of Applied Physics*, 106(2):023501 (7 pp.), 15 JUL 2009.
- [96] Y. Gong, M. Makarova, S. Yerci, R. Li, M. J. Stevens, B. Baek, S. W. Nam, R. H. Hadfield, S. N. Dorenbos, V. Zwiller, J. Vuckovic, and L. Dal Negro. Linewidth narrowing and Purcell enhancement in photonic crystal cavities on an Er-doped silicon nitride platform. *Optics Express*, 18(3):2601–12, JAN 2010.
- [97] I. Sychugov, R. Juhasz, J. Valenta, and J. Linnros. Narrow luminescence linewidth of a silicon quantum dot. *Physical Review Letters*, 94(8):087405/1–4, 4 MAR 2005.

- [98] S. G. Johnson, M. Ibanescu, M. A. Skorobogatiy, O. Weisberg, J. D. Joannopoulos, and Y. Fink. Perturbation theory for Maxwell's equations with shifting material boundaries. *Physical Review E*, 65(6):066611/1–7, JUN 2002.
- [99] L.-D. Haret, T. Tanabe, E. Kuramochi, and M. Notomi. Extremely low power optical bistability in silicon demonstrated using 1D photonic crystal nanocavity. *Optics Express*, 17(23):21108–21117, 9 NOV 2009.
- [100] L.-W. Wang and A. Zunger. Dielectric constants of silicon quantum dots. *Physical Review Letters*, 73(7):1039–42, 15 AUG 1994.
- [101] L. Pavesi and M. Ceschini. Stretched-exponential decay of the luminescence in porous silicon. *Physical Review B*, 48(23):17625–17628, 15 DEC 1993.
- [102] F. Trojanek, K. Neudert, M. Bittner, and P. Maly. Picosecond photoluminescence and transient absorption in silicon nanocrystals. *Physical Review B*, 72(7):75365–1–6, 15 AUG 2005.
- [103] K. G. Svantesson and N. G. Nilsson. Determination of the temperature-dependence of the free carrier and interband absorption in silicon at 1.06 μm . *Journal of Physics C - Solid State Physics*, 12(18):3837–3842, 1979.
- [104] J. J. Sakurai. *Modern Quantum Mechanics, Revised Edition*. Addison-Wesley, Massachusetts, 1994.
- [105] T. J. Kippenberg, A. L. Tchebotareva, J. Kalkman, A. Polman, and K. J. Vahala. Purcell-factor-enhanced scattering from Si nanocrystals in an optical microcavity. *Physical Review Letters*, 103(2):027406 (4 pp.), 10 JUL 2009.
- [106] M. Makarova, V. Sih, J. Warga, R. Li, L. Dal Negro, and J. Vuckovic. Enhanced light emission in photonic crystal nanocavities with erbium-doped silicon nanocrystals. *Applied Physics Letters*, 92(16):161107–1–3, 21 APR 2008.
- [107] M. Makarova, Y. Gong, S.-L. Cheng, Y. Nishi, S. Yerci, R. Li, L. Dal Negro, and J. Vuckovic. Photonic Crystal and Plasmonic Silicon-Based Light Sources.

- IEEE Journal of Selected topics in Quantum Electronics*, 16(1):132–140, JAN-FEB 2010.
- [108] H. Altug and J. Vuckovic. Experimental demonstration of the slow group velocity of light in two-dimensional coupled photonic crystal microcavity arrays. *Applied Physics Letters*, 86(11):111102, 14 MAR 2005.
 - [109] R. H. Hadfield, M. J. Stevens, S. S. Gruber, A. J. Miller, R. E. Schwall, R. P. Mirin, and S. W. Nam. Single photon source characterization with a superconducting single photon detector. *Optics Express*, 13(26):10846–10853, 22 DEC 2005.
 - [110] A. Polman, D. C. Jacobson, D. J. Eaglesham, R. C. Kistler, and J. M. Poate. Optical Doping of wave-guide materials by MeV Er implantation. *Journal of Applied Physics*, 70(7):3778–3784, 1 OCT 1991.
 - [111] H. J. Kimble. Structure and dynamics in cavity quantum electrodynamics. In *Cavity Quantum Electrodynamics (Advances in Atomic, Molecular and Optical Physics)*, edited by Paul Berman. Academic Press, JAN 1994.
 - [112] Y. C. Yan, A. J. Faber, H. deWaal, P. G. Kik, and A. Polman. Erbium-doped phosphate glass waveguide on silicon with 4.1 dB/cm gain at 1.535 μm . *Applied Physics Letters*, 71(20):2922–2924, 17 NOV 1997.
 - [113] H.-S. Han, S.-Y. Seo, J. H. Shin, and N. Park. Coefficient determination related to optical gain in erbium-doped silicon-rich silicon oxide waveguide amplifier. *Applied Physics Letters*, 81(20):3720–2, 11 NOV 2002.
 - [114] O. Painter, R. K. Lee, A. Scherer, A. Yariv, J. D. O'Brien, P. D. Dapkus, and I. Kim. Two-dimensional photonic band-gap defect mode laser. *Science*, 284(5421):1819–1821, 11 JUN 1999.
 - [115] M. Loncar, T. Yoshie, K. Okamoto, Y. M. Qiu, J. Vuckovic, and A. Scherer. Planar photonic crystal nanolasers (I): Porous cavity lasers. *IEICE Transactions on Electronics*, E87C(3):291–299, MAR 2004.

- [116] Y. Zhang, M. Khan, Y. Huang, J. Ryou, P. Deotare, R. Dupuis, and M. Loncar. Photonic crystal nanobeam lasers. *Applied Physics Letters*, 97(5):051104 (3 pp.), 2 AUG 2010.
- [117] B.-H. Ahn, J.-H. Kang, M.-K. Kim, J.-H. Song, B. Min, K.-S. Kim, and Y.-H. Lee. One-dimensional parabolic-beam photonic crystal laser. *Optics Express*, 18(6):5654–60, 4 MAR 2010.
- [118] T. P. M. Alegre, R. Perahia, and O. Painter. Optomechanical zipper cavity lasers: theoretical analysis of tuning range and stability. *Optics Express*, 18(8):7872–7885, 12 APR 2010.
- [119] D. Englund and J. Vuckovic. A direct analysis of photonic nanostructures. *Optics Express*, 14(8):3472–3483, 17 APR 2006.
- [120] L. Coldren and S. Corzine. *Diode Lasers and Photonic Integrated Circuits*. Wiley & Sons, New York, 1995.
- [121] I. Friedler, C. Sauvan, J. P. Hugonin, P. Lalanne, J. Claudon, and J. M. Gerard. Solid-state single photon sources: the nanowire antenna. *Optics Express*, 17(4):2095–2110, 16 FEB 2009.
- [122] T. M. Babinec, B. J. M. Hausmann, M. Khan, Y. Zhang, J. R. Maze, P. R. Hemmer, and M. Loncar. A diamond nanowire single-photon source. *Nature Nanotechnology*, 5(3):195–199, MAR 2010.
- [123] U. Mohideen, R. E. Slusher, F. Jahnke, and S. W. Koch. Semiconductor microlaser linewidths. *Physical Review Letters*, 73(13):1785–1788, 26 SEP 1994.
- [124] G. Shambat, Y. Gong, J. Lu, S. Yerci, R. Li, L. Dal Negro, and J. Vuckovic. Coupled fiber taper extraction of 1.53 μ m photoluminescence from erbium doped silicon nitride photonic crystal cavities. *Optics Express*, 18(6):5964–5973, 15 MAR 2010.

- [125] I. K. Hwang, S. K. Kim, J. K. Yang, S. H. Kim, S. H. Lee, and Y. H. Lee. Curved-microfiber photon coupling for photonic crystal light emitter. *Applied Physics Letters*, 87(13):131107, 26 SEP 2005.
- [126] J. S. Biteen, N. S. Lewis, H. A. Atwater, H. Mertens, and A. Polman. Spectral tuning of plasmon-enhanced silicon quantum dot luminescence. *Applied Physics Letters*, 88(13):131109, 27 MAR 2006.
- [127] T. Hatano, B. Nishikawa, M. Iwanaga, and T. Ishihara. Optical rectification effect in 1D metallic photonic crystal slabs with asymmetric unit cell. *Optics Express*, 16(11):8236–8241, 26 MAY 2008.
- [128] A. Kocabas, S. Seckin Senlik, and A. Aydinli. Plasmonic band gap cavities on biharmonic gratings. *Physical Review B*, 77(19):195130–1–7, 15 MAY 2008.
- [129] D. K. Gifford and D. G. Hall. Emission through one of two metal electrodes of an organic light-emitting diode via surface-plasmon cross coupling. *Applied Physics Letters*, 81(23):4315–4317, 2 DEC 2002.
- [130] H. Mertens and A. Polman. Plasmon-enhanced erbium luminescence. *Applied Physics Letters*, 89(21):211107, 20 NOV 2006.
- [131] D. E. Chandler, Z. K. Majumdar, G. J. Heiss, and R. M. Clegg. Ruby crystal for demonstrating time- and frequency-domain methods of fluorescence lifetime measurements. *Journal of Fluorescence*, 16(6):793–807, NOV 2006.
- [132] D. Van Thourhout and J. Roels. Optomechanical device actuation through the optical gradient force. *Nature Photonics*, 4(4):211–217, APR 2010.
- [133] T. J. Kippenberg and K. J. Vahala. Cavity optomechanics: Back-action at the mesoscale. *Science*, 321(5893):1172–1176, 29 AUG 2008.
- [134] M. Eichenfield, J. Chan, R.M. Camacho, K. J. Vahala, and O. Painter. Optomechanical crystals. *Nature*, 461(7269):78–82, 5 NOV 2009.

- [135] M. L. Povinelli, M. Loncar, M. Ibanescu, E. J. Smythe, S. G. Johnson, F. Capasso, and J. D. Joannopoulos. Evanescent-wave bonding between optical waveguides. *Optics Letters*, 30(22):3042–3044, 15 NOV 2005.
- [136] M. L. Povinelli, S. G. Johnson, M. Loncar, M. Ibanescu, E. J. Smythe, F. Capasso, and J. D. Joannopoulos. High-Q enhancement of attractive and repulsive optical forces between coupled whispering-gallery-mode resonators. *Optics Express*, 13(20):8286–8295, 3 OCT 2005.
- [137] W. H. P. Pernice, M. Li, and H. X. Tang. Theoretical investigation of the transverse optical force between a silicon nanowire waveguide and a substrate. *Optics Express*, 17(3):1806–1816, 2 FEB 2009.
- [138] T. J. Kippenberg, H. Rokhsari, T. Carmon, A. Scherer, and K. J. Vahala. Analysis of radiation-pressure induced mechanical oscillation of an optical microcavity. *Physical Review Letters*, 95(3):033901/1–4, 15 JUL 2005.
- [139] M. Eichenfield, C. P. Michael, R. Perahia, and O. Painter. Actuation of micro-optomechanical systems via cavity-enhanced optical dipole forces. *Nature Photonics*, 1(7):416–422, JUL 2007.
- [140] M. Notomi, H. Taniyama, S. Mitsugi, and E. Kuramochi. Optomechanical wavelength and energy conversion in high-Q double-layer cavities of photonic crystal slabs. *Physical Review Letters*, 97(2):023903/1–4, 14 JUL 2006.
- [141] G. S. Wiederhecker, L. Chen, A. Gondarenko, and M. Lipson. Controlling photonic structures using optical forces. *Nature*, 462(7273):633–U103, 3 DEC 2009.
- [142] M. Li, W. H. P. Pernice, C. Xiong, T. Baehr-Jones, M. Hochberg, and H. X. Tang. Harnessing optical forces in integrated photonic circuits. *Nature*, 456(7221):480–4, 27 NOV 2008.
- [143] M. Li, W. H. P. Pernice, and H. X. Tang. Tunable bipolar optical interactions between guided lightwaves. *Nature Photonics*, 3(8):464–468, AUG 2009.

- [144] J. Roels, I. De Vlaminck, L. Lagae, B. Maes, D. Van Thourhout, and R. Baets. Tunable optical forces between nanophotonic waveguides. *Nature Nanotechnology*, 4(8):510–513, AUG 2009.
- [145] A. Schliesser, R. Riviere, G. Anetsberger, O. Arcizet, and T. J. Kippenberg. Resolved-sideband cooling of a micromechanical oscillator. *Nature Physics*, 4(5):415–419, MAY 2008.
- [146] T. J. Kippenberg and K. J. Vahala. Cavity opto-mechanics. *Optics Express*, 15(25):17172–17205, 10 DEC 2007.
- [147] A. H. Safavi-Naeini, T. P. M. Alegre, M. Winger, and O. Painter. Optomechanics in an ultrahigh-Q slotted 2D photonic crystal cavity. *ArXiv e-prints*, page 1006.3964, June 2010.
- [148] K. S. Yee. Numerical Solution of Initial Boundary Value Problems Involving Maxwell’s Equations in Isotropic Media. *IEEE Transactions on Antennas and Propagation*, AP14(3):302, 1966.
- [149] A. Taflove and S. C. Hagness. *Computational Electrodynamics: The Finite-Difference Time-Domain Method*. Artech House, Norwood, MA, 3rd edition, 2005.